UNIVERSITÀ DEGLI STUDI DI URBINO CARLO BO

Dipartimento di Scienze Pure ed Applicate (DiSPeA)

Corso di Dottorato di Ricerca in Scienze di Base e Applicazioni

Curriculum Scienze della Terra - XXXI ciclo

Titolo della tesi:

SURFACE EXPLORATION AND PETROLOGICAL APPLICATIONS IN HIGH ENTHALPY GEOTHERMAL AREAS: A MULTIDISCIPLINARY APPROACH FOR THE CERRO PABELLÓN PROJECT (NORTHERN CHILE)

ESPLORAZIONE DI SUPERFICIE ED APPLICAZIONI PETROLOGICHE IN AREE GEOTERMICHE AD ALTA ENTALPIA: UN APPROCCIO MULTIDISCIPLINARE NELL'AMBITO DEL PROGETTO CERRO PABELLÓN (CILE SETTENTRIONALE)

Settore Scientifico Disciplinare SSD: GEO/08

Candidato

Marco Taussi

Relatore:
Prof. **Alberto Renzulli**

Co-relatore:
Prof. **Diego Morata**

Anno Accademico: 2017-2018

INDEX

CHAPTER 1

MOTIVATIONS, GENERAL INTRODUCTION AND SUMMARY OF THE THESIS

Motivations

The present thesis was carried out in the frameworks of a collaboration with Enel Green Power and of a Memorandum of Understanding between the Department of Pure and Applied Sciences (DiSPeA) of the University of Urbino and the Faculty of Physical and Mathematical Sciences of the Universidad de Chile (Santiago).

The Cerro Pabellón geothermal system, located in Northern Chile, which is the main object of this work, is classified as a blind (or hidden) geothermal field. In fact, the only hydrothermal manifestations are represented by two fumaroles located on the top of the Apacheta volcano, set to the west and about 600 m higher than the Cerro Pabellón geothermal area.

The aim of this PhD research project was to deepen the knowledge concerning the heat source and the evolution of the related magmatic plumbing system, define the clay-cap units and constrain its role and importance in the circulation of fluids toward the surface, producing an update conceptual model. A multidisciplinary approach was involved and focused on three complementary scientific studies:

- A petrological, geochemical and isotopic study on the Apacheta-Aguilucho Volcanic Complex and on the most recent volcanic products of the Altiplano-Puna Volcanic Complex, represented by the dacitic domes of Chanka, Chac-Inca and Pabellón. The main purpose was, after the identification of the amphibole crystallization depth (i.e. the depth of the heat source/s), to define the evolution of the magmatic plumbing system, and the mixing/mingling processes of the different magmas.
- A mineralogical study through X-Ray Powder Diffraction analysis of samples from a production geothermal well and an exploration drill core, besides clay-rich samples from the Cerro Apacheta fumarolic field (adjacent to the project area). The purpose of this work was to examine the vertical and superficial distribution of the clay minerals forming the hydrothermal system of the Cerro Pabellón active geothermal field, in order to identify the minerals associations, define the clay-cap units and characterize the type of hydrothermal alteration.
- A geochemical study of the diffuse CO_2 soil flux and temperatures measurements, coupled with soil temperature gradients carried out at the fumarolic field, in order to define the sealing capacity of the clay-cap units and their importance in preventing the rise of the fluids toward the surface.

The final goal of this investigations was to give a multidisciplinary concept of geothermal exploration combining geological, volcanological, mineralogical, petrological and geochemical investigations, applying it to a blind (or hidden) geothermal system. The primary characteristic of a blind (or hidden) geothermal system is related to the lack of classic high-enthalpy-related superficial manifestations, such as geysers, fumaroles, sinter deposits, and hot springs.

Obviously, blind or hidden geothermal systems have not been extensively developed, as they are difficult to confirm in absence of drilling programs that can confirm the productivity of the reservoirs. Thus, the presence of the first geothermal power plant of South America, related to such a blind geothermal system, gave us a great opportunity to study and deepen the main features characterizing this system. A major comprehension of the processes involved in the formation of these geothermal areas is essential to extend geothermal exploration to other feasible areas where no surface manifestations are recognized.

1.1. Geothermal energy: current World situation

The continuous growth of energy consumption, the gradual and rapid depletion of oil reserves, coal and, more generally, fossil fuels, coupled with the consequent and constant increase in greenhouse gas emissions, requires the use of renewable sources for sustainable development and environmental protection. Therefore, on a local and global scale, energy plans must provide a policy focused on improving energy efficiency and exploiting renewable sources. Among the others, geothermal represents a promising energy source to satisfy the growing energy needs. Geothermal is the natural heat of the Earth. The temperature at the Earth's centre is estimated to reach up to 5,500 °C. This heat is derived from the original formation of the planet and from the decay of the radioactive elements in the Earth's crust. It is transferred to the subsurface mainly by conduction and convection.

For centuries, geothermal springs have been used for bathing, heating and cooking, but only in the early 20th century people started to consider the heat from inside the Earth as a practical source of energy with huge potential. In fact, the use of geothermal resources for energy purposes celebrated its centenary in 2013. In 1904 in Larderello (Italy) Prince Piero Ginori Conti powered five bulbs from a dynamo driven by a reciprocating steam engine using geothermal power. This success opened the way to a commercial development of the geothermal electricity, and in 1913 the first geothermal power plant started its operations with a capacity of 250 kWe. The Italian experience waked-up the interest on geothermal electricity in other countries. Geothermal energy is now used to produce electricity, to heat and cool buildings as well as for other industrial purposes like zootechnics, paper processing, fruit and vegetable cultivation, soil warming and many others. The exploitable geothermal resources are found throughout the world and are utilized nowadays in 83 countries, 27 of which also produce electrical energy (IGA Geothermal Energy Database, 2015). Surprisingly, until 2017 none of the South American countries was included in this list (Fig. 1.1). Only a small fraction of geothermal has been used so far and there is still much to do for development in both electricity generation and direct use applications.

Figure 1.1 *- Global map of the use of the geothermal resource (from IGA Geothermal Energy Database, 2015).*

The electric production from geothermal sources covers about 0.5% of the world's energy needs (Chamorro et al., 2012), but the development of new technologies for its exploitation and the numerous new studies concerning sites of potential interest, ensure that the growth margins of geothermal production are wide. It has been passed from about 11,000 MW of installed capacity in 2010, to about 14,000 MW in 2017 (Pan et al., 2019; Fig. 1.2), with an estimated further increase up to about 21,000 MW in 2020 (Bertani, 2015).

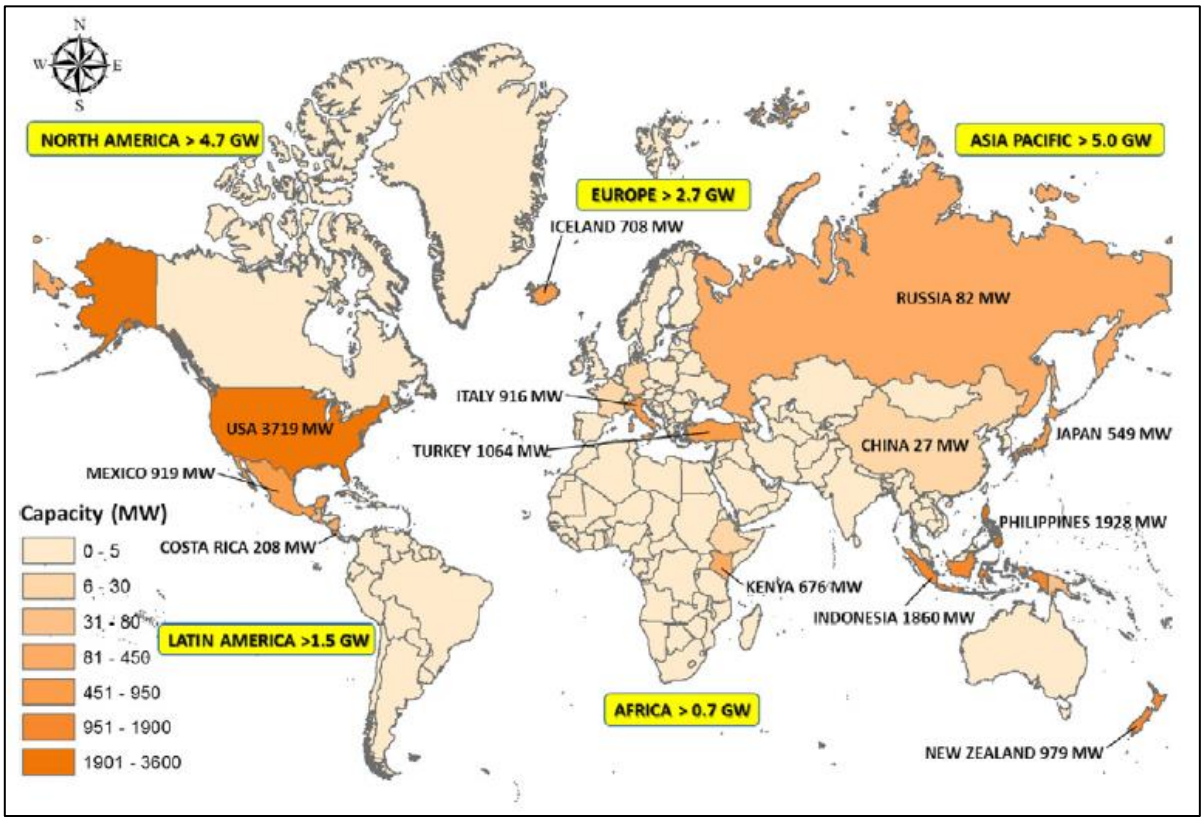

Figure 1.2 *- Global map of the installed capacity of geothermal energy plant for electricity production in 2017 (14.3 GWe; Pan et al., 2019).*

The main producers of energy from geothermal sources are represented by the USA, the Philippines, Indonesia, Mexico, New Zealand and Italy.

In the most industrialized countries, it is unlikely that large investments will be directed towards this energy sector, whereas in developing countries, characterized by lower energy consumption and with suitable geological and geodynamic features for exploitation of this source, geothermal energy can constitute a significant renewable, competitive with conventional non-renewable sources. Another important development desirable for the geothermal source is that related to non-electrical uses, therefore linked to the direct use of natural hot water, or to the production of thermal energy from plants with geothermal heat pumps, which can play a decisive role in the energy saving produced by fossil fuels.

Among the countries with a significant geothermal potential for electric production, as they cover geologically favourable areas, we found all the countries that include the Andean regions of South America, such as Colombia, Ecuador, Peru, Argentina and Chile. This latter in particular shows a remarkable potential and currently, almost completely unexpressed (Procesi, 2014; Lahsen et al., 2015; Aravena et al., 2016).

1.2. Geothermal exploration in Chile

Chile is the World's leading state in copper production and the mining industry is the country's main economic resource. The mining industry, however, imports more than 75% of the energy it needs (Lahsen et al., 2015) and in recent years the Chilean Government, also in collaboration with Enel Green Power Latin America, has therefore started to promote on its territory (in addition to hydroelectric) renewable sources of energy such as wind, photovoltaic and geothermal with the specific Cerro Pabellón project.

In Chile the demand for electricity increases by 5% every year, which is why an annual increase of approximately 1,000 MWe is required (Lahsen et al., 2015). The increase in the production of electricity from renewable sources is an important objective for the Chilean Government, to try to reduce the dependence on the importation of fossil fuels and to reduce greenhouse gas emissions in atmosphere. Geothermal resources could provide a clean source for electricity generation, since the country needs to import nearly 85% of fossil fuels for electricity production. Among the South American geothermal potential, Chile's one has been estimated to be more than 1,300 MWe (Procesi, 2014; Aravena et al., 2016), equivalent to ~4.4% of the total installed electric capacity in Chile (Aravena et al., 2016).

Early geothermal exploration in the country began in 1921 with the drilling of two ~80 m deep wells at the El Tatio geothermal field (Tocchi, 1923; Lahsen et al., 2005; Bona and Coviello, 2016). A prefeasibility investigation, funded at the end of '60s by the Chilean Development Corporation (Corporación de Fomento de la Producción, CORFO) and the United Nations Development Program (UNDP) (Procesi, 2014), was followed by geological (Lahsen, 1969; Trujillo, 1971), geophysical (McDonald, 1969, 1974; Hochstein, 1971; ELC, 1980) and geochemical (Mahon, 1974; Lahsen, 1976; Cusicanqui, 1978a,b) surveys. Six 600 m-deep exploration wells, drilled between 1969 and 1971, encountered temperatures up to 250 °C (Tassi et al., 2010). Between the '70s and the '80s numerous supplementary explorations, drilling and feasibility studies have been conducted (Lahsen 1988; Hauser, 1997; Peréz, 1999; Procesi, 2014), also in other geothermal prospects, such as Puchuldiza-Tuja and Surire, with good results (i.e. geothermometric calculations of reservoir temperatures up to 166 and 230 °C, respectively; JICA, 1979, 1981; Cusicanqui, 1979). Geothermal exploration was abandoned in 1982 because of both the remote location of the hydrothermal systems and economic factors. By early 2000, a new impulse was given by the issue of a Chilean law providing the framework for the exploration and development of geothermal energy. In that period (2005) the Italian ENEL enterprise made joint ventures with the Chilean enterprise ENAP (National Oil Company) starting a new company, i.e. Empresa Nacional de Geotermia (ENG), and also becoming shareholder in the Geotermica del Norte enterprise (2007) in order to develop geothermal exploration both in northern and central-southern Chile. Lately, during the first half of 2011, the Chilean Government founded the Andean Geothermal Center of

Excellence (Centro de Excelencia en Geotermia de Los Andes, CEGA), a FONDAP-CONICYT project hosted at the Universidad de Chile, aimed at improving geothermal knowledge and promoting its use in the Andean countries (Aravena et al., 2016). Nowadays, geothermal exploration is currently active and is driven by the need for energy security. In the country there are more than 300 geothermal areas associated with Quaternary volcanism (Lahsen et al., 2015). During the last 8 years, fourteen private companies were involved on exploring operations in 76 geothermal concession areas with the aim to identify areas of highest technical and commercial potential. In all these areas current exploration activities involves geological and structural surveys, volcanological studies, and geophysical and geochemical studies to find areas with high geothermal potential where exploratory drilling will be conducted (Lahsen et al., 2015).

1.3. Chilean main geothermal systems

The high-temperature areas in Chile are located along the Andean Cordillera in close spatial relationship with active volcanism, primarily controlled by the convergence of the Nazca and South American Plates. The main geothermal systems occur in the northern (17-28 °S) and central-southern part (33-46 °S) of Chile (Fig. 1.3). The flat slab geometry of the subducting oceanic plate (i.e. Nazca plate) beneath the continental plate (i.e. South American plate) generates areas of volcanic gaps (Barazangi and Isacks, 1976) between 28 and 33 °S, and 46 and 48 °S. In these gaps thermal manifestations are scarce and their temperature are usually lower than 30 °C (Lahsen et al., 2010).

The Northern Chile geothermal zone (Fig.1.3a) has about 90 identified hot-spring areas (Hauser, 1997), and 45 exploration concessions are being surveyed (Lahsen et al., 2015). In this region, the most advanced exploration programs have been carried out in the Colpitas, Apacheta, Pampa Lirima and El Tatio-La Torta geothermal prospects (e.g. Urzua et al., 2002; Aguirre et al., 2011; Soffia and Clavero, 2010). Exploratory (or exploitation as in the case of Apacheta, i.e. Cerro Pabellón project) wells have been drilled in all of these four prospects. Their estimated combined power potential of exploitable geothermal energy is between 400 and 1,000 MWe (Lahsen et al., 2015). Exploitation concessions have been granted for the Apacheta and El Tatio geothermal fields, and the environmental assessment for the installation of a 50 MWe power plant has been approved for Apacheta. The El Tatio project was the most advanced but, has been cancelled in 2013 due to the company failing to comply with environmental and safety requirements (source: http://www.thinkgeoenergy.com).

In the Central-Southern Chile geothermal zone (Fig. 1.3b) there are more than 200 geothermal areas (Hauser, 1997) and 31 explorations concessions are underway. The most advanced exploration surveys have been completed at the Tinguiririca, Calabozos, Laguna

del Maule, Nevados de Chillán, Tolhuaca, and Cordón Caulle geothermal areas (e.g., Clavero et al., 2011; Soffia and Clavero, 2010; Melosh et al., 2010, 2012; Hickson et al., 2011; Aravena et al., 2016). Exploratory wells have been drilled in all these prospects and the estimated combined power potential for the five areas ranges from 650 to 950 MWe (Lahsen et al., 2015). Exploration concessions were granted for the Laguna del Maule area (Mariposa sector) and Tolhuaca (San Gregorio) prospects, where production-size wells have been drilled. An environmental impact assessment was submitted to the authorities for the approval of the installation of a 70 MWe power plant at Tolhuaca where well Tol-4 has an output of 12 MWe based on flow testing data (Lahsen et al., 2015).

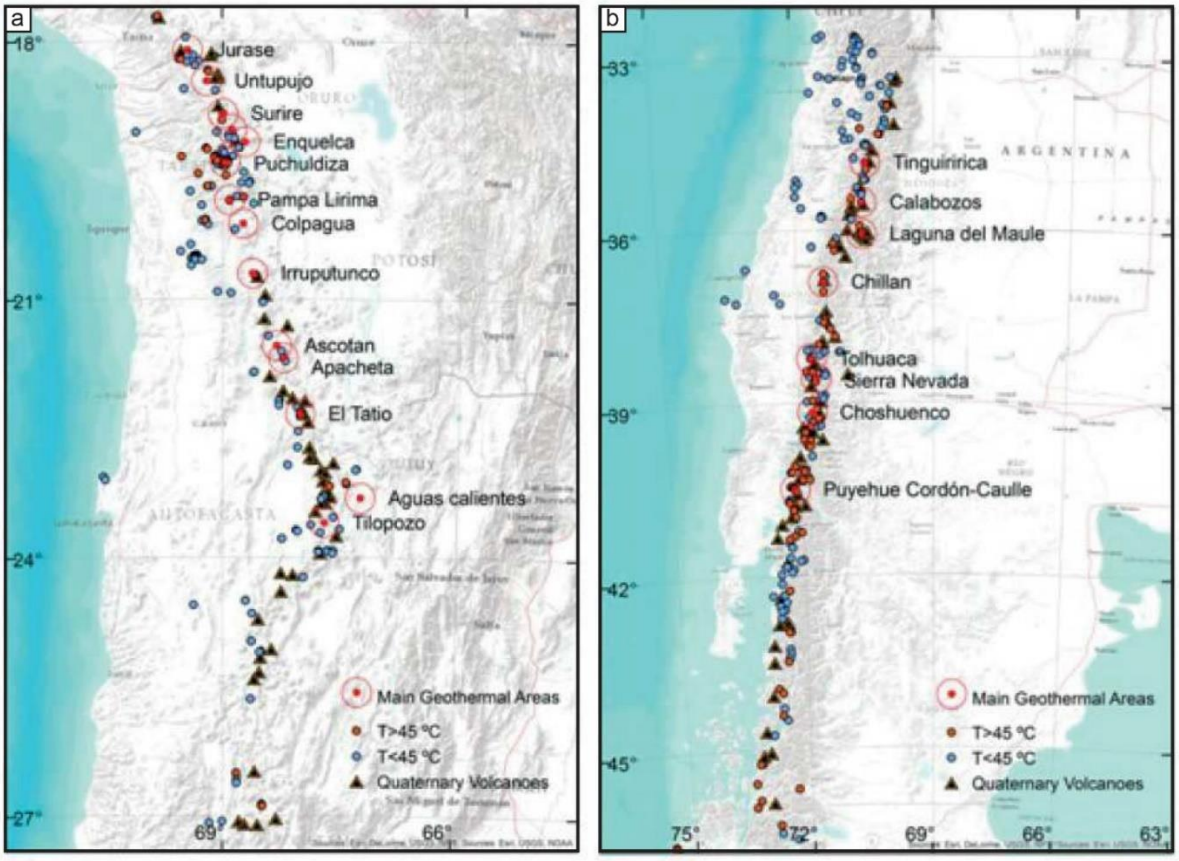

Figure 1.3 *- Main geothermal prospects of a) Northern Chile, and b) Central-Southern Chile; modified from Lahsen et al. (2015).*

1.4. Cerro Pabellón geothermal project

The Cerro Pabellón geothermal power generation project is located in the Ollagüe municipality, Antofagasta region, Northern Chile, ~100 km NE from city of Calama, and at 4,520 meters a.s.l. The concession is owned by a joint project between ENEL Latin-America (Chile) Ltd., and the National Oil Company (ENAP). The project, currently under production, involves the operation of an Organic Rankine Cycle (ORC) binary geothermal power plant, consisting of two units with an installed capacity of 48 MWe (source: https://www.enelchile.cl).

The site was luckily discovered by CODELCO at the end of '90s during water-related exploring operations (Urzua et al., 2002). Magnetotelluric (MT) and time domain electromagnetic (TDEM) surveys detected a low resistivity boundary (<10 ohm-m) extending over an area of 25 km^2 and geochemical survey indicated reservoir temperature of 250-260 °C (Urzua et al., 2002). Temperature >200 °C was successively measured at depth > 500 m in a 557 m-deep core-hole carried out by the Empresa Nacional de Geotermia in October 2007.

The geothermal system is located upon a large zone of silicic volcanism occupying the 21-24 °S segment of the Andean Central Volcanic Zone (de Silva, 1989; de Silva et al., 1994) and it is hosted by a ~4 km wide NW-SE trending graben where on the SW fault the Pliocene-Pleistocene lavas and pyroclastic products of the Apacheta-Aguilucho Volcanic Complex were erupted, while in the NE fault the Pleistocene Pabellón dacitic dome was extruded. Nowadays, this graben-hosted system has six deep wells platforms (Fig. 1.4), that allowed to exploit the liquid-dominate geothermal reservoir. The thickness of the reservoir is constrained by the convective regime in wells CP-1 (880 m) and CP-2 (1,120 m), starting at 900 and 820 m depth, respectively (Aravena et al., 2016). Wells CP-4 and CP-3 show a conductive regime (ENEL, 2012). The minimum horizontal extension of the reservoir (4 km^2) is given by the distance between wells. Maximum extension in the NE-SW orientation is given by the projected distance between the graben main faults at the depth of the reservoir. In the NW-SE direction, maximum extension will be considered as the linear projection of thickness vs. distance for wells CP-1 and CP-2 (~5 x 5 km^2). Minimum and maximum temperatures of the reservoir are reached in wells CP-2 (212 °C) and CP-1 (256 °C) respectively, which are consistent with gas geothermometry estimates of around 250 °C reported by Urzua et al. (2002), and Tassi et al. (2010).

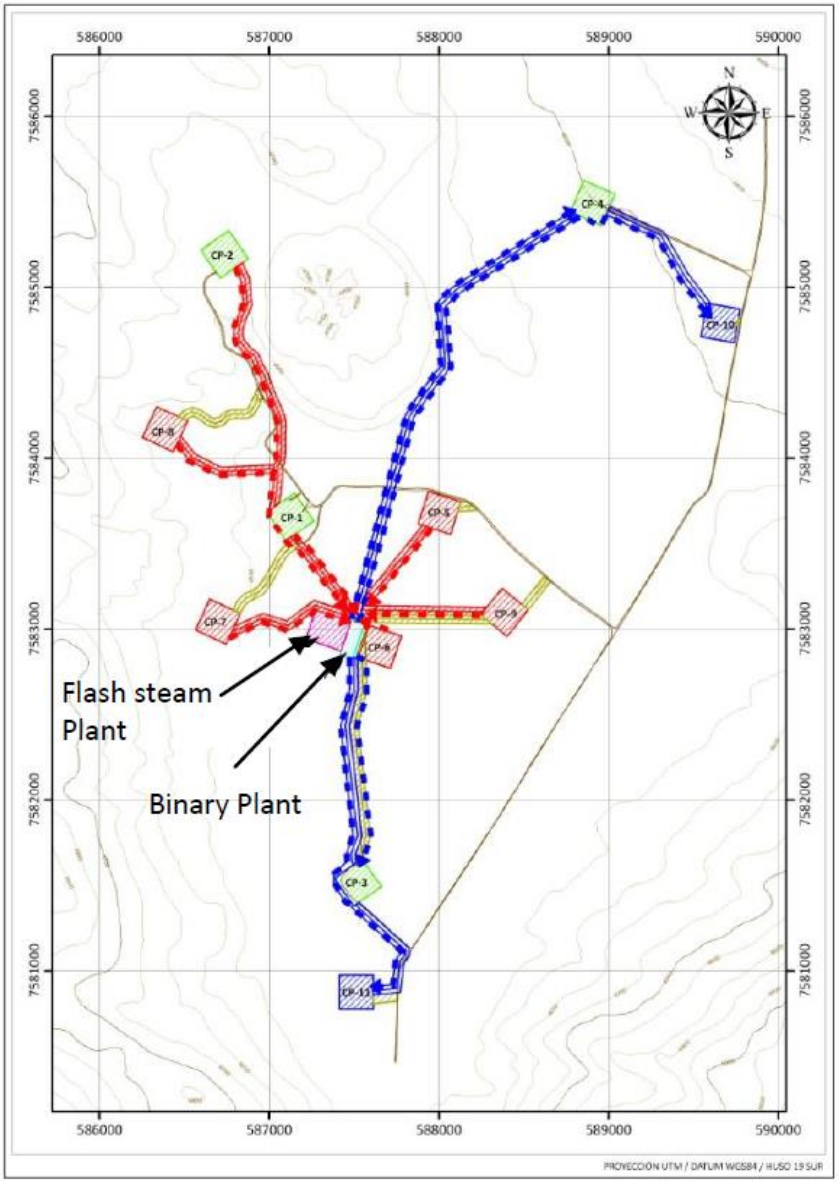

Figure 1.4 *- Production and re-injection platforms of the power plant. Red lines: production platforms and pipeline system of hot fluid toward the plant. Blue squares and line: re-injection platforms and pipeline system to re-injection wells. Green squares: platforms that have already been constructed in the context of the exploration stage. Nowadays, six platforms have been constructed (i.e. CP-1, CP-2, CP-3, CP-4 and CP-5). CP-7, CP-8, CP-9, CP-10 and CP-11 were not constructed yet, related to a possible future implementation of the power plant (ENEL, personal communication). Source: http://cdm.unfccc.int.*

1.5. Summary and structure of the thesis

The structure of this PhD thesis has been thought as a compendium of scientific papers, represented by the main chapters (i.e. 2, 3 and 4), exposed in a consequential and complementary way. In fact, after this short introduction on geothermal energy and on the main features of the Cerro Pabellón project, the chapters present three main subjects, in order to highlight the multidisciplinary purpose of the study.

1.5.1. Chapter 2

It deals with the main petrological processes affecting the magmatic plumbing system of the Apacheta-Aguilucho Volcanic Complex and the nearby dacitic domes. Moreover, a brief synthesis of the amphibole thermobarometry results is also given. These latter have been obtained during two previous PhD projects carried out at the University of Urbino (Piscaglia, 2011; Gorini, 2017), and completed during this PhD work, so they are not extensively reported.

Abstract

The evolution of the magma plumbing system of the Pleistocene Apacheta-Aguilucho Volcanic Complex and the nearby young dacitic domes, located in the Central Andean Volcanic Zone (Northern Chile), above one of the thickest crusts in the world (>70 km), was investigated through petrographic, geochemical and isotopic studies of representative lavas and related enclaves. Updated available dates of these products, both from the Apacheta and Aguilucho stratovolcanoes and nearby domes, allow us to define the activity during the last 1 Ma. This investigation showed that the andesitic magmas were affected by processes of Assimilation plus Fractional Crystallization (AFC, with a significant role played by amphibole fractionation) during their ascent through the upper crust, presumably by the interaction with the Altiplano-Puna Magma Body (APMB). The APMB is a voluminous (~500,000 km^3) igneous, partially-molten body located at a crustal depth of 15-20 km. These andesitic magmas were erupted with no or minor additional contamination at shallower levels, or experienced plagioclase-dominated Fractional Crystallization (FC) to dacite within shallower crustal magma chambers (4-8 km depth). The constructional phase of the Apacheta and Aguilucho stratovolcanoes (≥ 1 to ca. 0.6 Ma) reflect a transition from high-flux (i.e. flare-ups) to steady state magmatism, as also documented in other Pleistocene volcanic complexes of the Altiplano-Puna Volcanic Complex. During this stage the mafic magma recharge was high enough to permit a large spectrum of hybridization of the resident magmas in the upper crust to form the abundant andesites and dacites lavas. In contrast, at ~150-100 ka, the magmatism turned to a new stage of recharge (waning stage?) and the episodic intrusion of small-volumes of andesitic magmas permitted the remobilization of the crystal-rich dacites, triggering the extrusions of the Chanka, Chac-Inca and Cerro Pabellón domes. The andesitic enclaves in the domes studied here represent a snapshot of the magmatic processes of interaction that occurred in the shallower reservoir at the interface of the resident dacite with the ascending andesitic magma. A revised petrogenetic model, firstly reported by Coombs et al. (2002), well constrains the textural and geochemical variation in observed enclaves, which are strongly influenced by the location of crystallization with respect to the andesite-dacite interface. Nevertheless, as there are no dated volcanic products from the area between 0.6 and 0.1 Ma, the youngest dacitic domes could also be interpreted as the beginning of a new magmatic

pulse of the Altiplano-Puna Volcanic Complex. Independently from the significance of the mafic recharge at 150-100 ka (waning stage vs. new pulse) the youngest investigated domes share similar geochemical features and crustal depth constraints (4-8 km) with the ignimbrites of the Altiplano-Puna Volcanic Complex, therefore suggesting that the remobilized magmas erupted as the domes are possibly remains of older plumbing systems left over from the last magmatic flare-up of the Altiplano-Puna Volcanic Complex.

1.5.2. Chapter 3

In this chapter the mineralogical associations present at the Cerro Pabellón geothermal system, both deep and superficial, were investigated through X-Ray Diffraction (XRD) analyses. The purpose of this section was to examine the vertical and superficial distribution of the clay minerals forming the hydrothermal system of the Cerro Pabellón active geothermal field, in order to identify the minerals associations, define the clay-cap units and characterize the type of hydrothermal alteration. The first preliminary results from the fumarolic deposits of the Cerro Apacheta fumarolic field are here presented, although further works and analyses need to be done on these samples, to define in detailed the physico-chemical processes that affected the fluid-rocks interactions. The data presented in this chapter are the results of a jointed collaborative investigation carried out by the PhD candidate (CP-1 well and fumarolic field samples) and the C.E.G.A. researchers (PexAP-1). The results, the discussion and the conclusions are the outcome of a scientific debate between these researchers.

Abstract

Mineralogical studies on the vertical and superficial distribution of the clay minerals forming the hydrothermal system of the Cerro Pabellón active geothermal field, were carried out. From the mineral assemblages recognized in the fumarolic field and in two boreholes located in the Pampa Apacheta, the system seems to be characterized by both acid-sulfate (fumarolic field) and adularia-sericite (boreholes) alteration types. The acid-sulfate alteration characterizes the upper parts of the Apacheta volcano, where the rising magmatic gases are mixed with shallower aquifer, producing acid-sulfate waters. Here, two main subzones are recognized: *i)* one characterized by high amounts of smectite, mainly coupled with cristobalite and feldspar, and *ii)* one characterized by kaolinite, mainly coupled with halloysite and subordinate smectite. It has been constrained how these subzones show a good correspondence with the location of the thermal manifestations, and a moderate accordance with the soil temperatures measured in the sampling locations. Conversely, a not-fitting with the pH conditions of stability for the smectite clay minerals group was observed. Although a unique explanation to this controversy is difficult, our preliminary data indicate the involvement of neutralization processes in the active vents areas in order to explain the presence of

smectite in such an acid environment (i.e. pH = 3.5), and typical acid-fluids leaching processes in the far-from-vents areas, where kaolinite represents the main mineralogical phase.
The geothermal reservoir is characterized by an adularia-sericite alteration and, from the mineralogical assemblages recognized, is possibly related to fluids with near-neutral pH. The blind nature of the Cerro Pabellón geothermal system might be linked to the thickness and low permeability of the clay-cap units (~300 m). Two main clay minerals transitions were detected in the clay-cap: the smectite to illite and the smectite to chlorite. In fact, the illite and chlorite only prevail in rock samples from the reservoir domain, where mixed-layer illite-smectite and chlorite-smectite are almost absent. In both reaction series, a continuous and slow reduction of the proportion of smectite layers in mixed-layer clays with depth was observed. The impermeability of the clay-cap of the geothermal system, would not favour the advance of illite-smectite and chlorite-smectite reaction series.

1.5.3. Chapter 4

It deals with the lack of superficial thermal manifestations of the blind geothermal system. The sealing capacity of the clay-cap units defined in chapter 3, was investigated through CO_2 soil flux and temperature measurements with the accumulation chamber methodology. Soil temperature gradients were also measured at the fumarolic field on the top of the Apacheta volcano, where the only active hydrothermal manifestations are present.

Abstract

The sealing capacity of the clay-cap units was investigated in the geothermal area through systematic diffuse CO_2 soil flux and temperature measurements (~500 points), using the accumulation chamber method. The low CO_2 flux and the relatively large areas of thermal anomalies identified, demonstrate the efficiency of the thick clay-cap to prevent the resurgence of fluids up to the surface. The low CO_2 effluxes measured in the main geothermal areas suggest that contribution by deep-seated CO_2 (magmatic origin) to soil degassing is almost negligible. In fact: i) the majority of the soil CO_2 flux measurements are below background levels and most shallow soil temperatures are higher than the temperature condition of air-saturated soil. No correlation between soil temperature and CO_2 flux is recorded, and the only significant thermal anomalies is registered at the active fumarolic field. The lack of soil CO_2 anomalies above the existing pressurized reservoir, can be due to two main factors: i.e. the continuous, thick, and impervious clay-cap, and the magmatic gas scrubbing processes in the liquid-dominated environment, that produce the removal of CO_2 and acidic magmatic compounds (i.e. SO_2 and HCl), with the consequent ascent of CO_2-depleted steam, heating the shallower aquifer/s. The latter resulting at the surface as a diffuse, slight thermal anomaly, recognized by a geostatistical approach, and at 187 m below the surface (i.e. at the bottom of

an exploratory well and above the clay-cap units) as a wispy flow of steam with measured temperature of 88 °C. As a matter of fact, the active fumarolic area, located at the summit of the Apacheta volcano, is the only visible evidence of the hidden geothermal reservoir in the Cerro Pabellón area.

1.5.4. Chapter 5

In this final chapter general conclusions and consideration on the 3 years PhD course are given, considering the main results obtained during this project. An update conceptual model of the Cerro Pabellón geothermal system and possible outlooks are also presented.

CHAPTER 2

PETROLOGICAL EVOLUTION OF THE APACHETA-AGUILUCHO VOLCANIC COMPLEX AND CONSTRAINTS FOR THE MAIN HEAT SOURCE

THE MAIN PART OF THIS CHAPTER HAS BEEN PUBLISHED AS:

Taussi, M., Godoy, B., Piscaglia, F., Morata, D., Agostini, S., Le Roux, P., Gonzalez-Maurel, O., Gallmeyer, G., Menzies, A., Renzulli, A., 2019. The upper crustal magma plumbing system of the Pleistocene Apacheta-Aguilucho Volcanic Complex area (Altiplano-Puna, northern Chile) as inferred from the erupted lavas and their enclaves. Journal Volcanology and Geothermal Research. Accepted 25 January 2019. https://doi.org/10.1016/j.jvolgeores.2019.01.021.

THE AMPHIBOLE THERMOBAROMETRY RESULTS HAVE BEEN PUBLISHED IN:

Gorini, A., Ridolfi, F., Piscaglia, F., **Taussi, M.**, Renzulli, A., 2018. Application and reliability of calcic amphibole thermobarometry as inferred from calc-alkaline products of active geothermal areas in the Andes. Journal of Volcanology and Geothermal Research 358, pp. 58-76. https://doi.org/10.1016/j.jvolgeores.2018.03.018.

2.1. Introduction

The Altiplano-Puna Volcanic Complex (APVC) is an ignimbritic plateau situated between 21° and 24°S and straddling Chile, Bolivia and Argentina (de Silva, 1989) in the Andean Central Volcanic Zone (CVZ; Fig. 2.1a). The 10–1 Ma ignimbrite flare-ups that occurred in this plateau are characterized by an episodic spatiotemporal pattern of eruptions at rates much higher than typical of continental arcs (de Silva and Gosnold, 2007). Large volumes (~15,000 km^3; de Silva and Kay, 2018) of dacitic to rhyolitic magmas, erupted in four major pulses at ~10, 8, 6, and 4 Ma increased in intensity until 4 Ma (Salisbury et al., 2011) and followed by a sharp decrease. Quaternary volcanism has a periodicity of ~1 Ma and exploits relict magmas produced earlier (de Silva et al., 2015). This tempo is controlled by the thermomechanical evolution of the upper-crustal magma reservoirs. As magma accumulates in the upper crust, feedbacks between temperature, host-rock mechanics and chamber pressurization results in ductile host-rock rheologies, which promote storage and growth over eruption and lead to reservoir growth under conditions of constant recharge flux and/or crystallization (de Silva and Gregg, 2014; de Silva et al., 2015; de Silva and Kay, 2018).

The area of the APVC investigated in the present work is represented by the Pleistocene Apacheta-Aguilucho Volcanic Complex (AAVC; Aguilera et al., 2008; Mercado et al., 2009; Fig. 2.1), and three late Pleistocene dacitic domes associated with the last eruptive pulse of the APVC: Chanka, Chac-Inca and Cerro Pabellón (hereafter Pabellón) (Fig. 2.1b). Between the AAVC and the Pabellón dome, the high-enthalpy geothermal field of the “Proyecto Cerro Pabellón” (previously called Apacheta project by Urzua et al., 2002), was developed.
This part of the Central Volcanic Zone has been affected by tectonic shortening that began about 35 Ma with strong acceleration during the last 10 Ma (Freymuth et al., 2015; Wörner et al., 2018), producing an anomalously thick crust (>70 km; Beck et al., 1996). The overthickened crust below the APVC hosts a partially-molten amalgamated igneous body (Zandt et al., 2003; Ward et al., 2014), the Altiplano-Puna Magma Body (APMB; *sensu* Chmielowsky et al., 1999). This magmatic body has been well constrained by seismic (Ward et al., 2014), gravimetric (del Potro et al., 2013) and magnetotelluric studies (Comeau et al., 2015, 2016), and is interpreted as a batholith (de Silva and Gosnold, 2007; Kern et al., 2016) corresponding to a zone of melting, assimilation, storage and homogenization (MASH, *sensu* Hildreth and Moorbath, 1988) at upper crustal levels (Ward et al., 2014; Godoy et al., 2014; Burns et al., 2015; de Silva and Kay, 2018), which fed the shallower sub-volcanic systems (de Silva and Gosnold, 2007). This partially molten igneous body represents a “mush” column (de Silva et al., 2006; Muir et al., 2014, 2015; Gottsmann et al., 2017), which contaminates the mantle-derived magmas with different degrees of assimilation (e.g. Kay et al., 2010; Burns et al., 2015; Godoy et al., 2017a; Maro et al., 2017; de Silva and Kay, 2018). The youngest volcanic products (< 2 Ma) show an increasing degree of contamination with location of the

partially molten body, going from the margins towards its centre located in correspondence to the Uturuncu volcano (Bolivia) (Michelfelder et al., 2013; Godoy et al., 2017a). In this context, the extrusion of the young dacitic domes, which represent the most recent phase of the APVC (de Silva et al., 1994; Tierney et al., 2016), together with monogenic edifices of other recent eruptions, such as La Poruña scoria cone (Bertin and Amigo, 2015) located about 30 km West of the studied area (Fig. 2.1c), may represent a window into pluton assembly during low eruptive flux stages of a magmatic flare-up that characterized the evolution of the APVC in the Quaternary period (de Silva and Gregg, 2014; Tierney et al., 2016). The present chapter is focused on the AAVC lavas, the Chanka, Chac-Inca and Pabellón dacitic domes and their enclaves, in order to explore (i) the Pleistocene magmatic plumbing system working in this area and (ii) the role played by the APMB in the evolution of the erupted magmas.

The aim of this chapter is to give a petrographic, geochemical (major and trace elements) and isotopic ($^{87}Sr/^{86}Sr$, $^{143}Nd/^{144}Nd$, $^{206}Pb/^{204}Pb$; $^{207}Pb/^{204}Pb$; $^{208}Pb/^{204}Pb$) characterization of representative samples from the extrusive products of the AAVC and the nearby enclave-hosting dacitic domes of Chanka, Chac-Inca and Pabellón. This dataset was applied to petrological modelling in order to investigate the intra-crustal magmatic processes in the last 1 Ma span time. These constrains, coupled with the results of the amphibole thermobarometry published in Gorini et al. (2018), can give a better comprehension of the intra-crustal magmatic evolution of the volcanic plumbing systems, and a characterization of the possible heat source/s of the geothermal area.

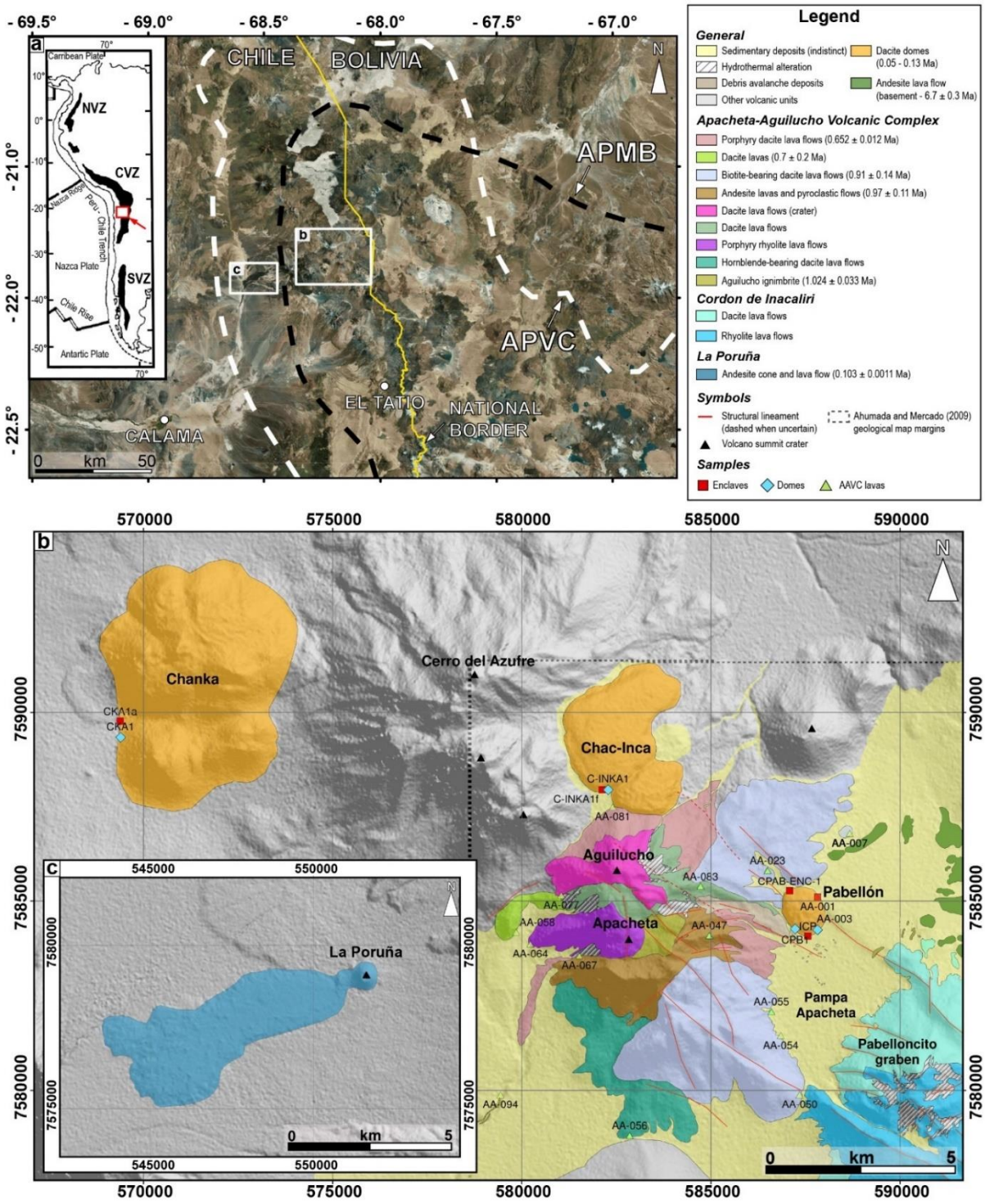

Figure 2.1 *- Location map of the Apacheta-Aguilucho Volcanic Complex and the domes. a) The small white rectangles indicate the locations of the studied areas reported in (b) and (c), in the framework of the Andean Central Volcanic Zone (CVZ; inset figure); the white dashed line delineates the Altiplano-Puna Volcanic Complex (APVC), black dashed line indicates the surface projection of the Altiplano-Puna Magma Body (APMB), after Zandt et al. (2003); yellow line indicates the national border between Chile and Bolivia. b) Simplified geological map of the Apacheta-Aguilucho Volcanic Complex showing the main volcanic and structural features of the area (after Ahumada and Mercado, 2009, Godoy et al., 2017b, and Sellés and Gardeweg, 2017). c) Enlarged view of the La Poruña scoria cone. Coordinates of b) and c) in WGS84, UTM 19S. Figure from Taussi et al. (2019).*

2.2. Geological background

2.2.1 Apacheta-Aguilucho Volcanic Complex and dacitic domes

The Pleistocene Apacheta-Aguilucho Volcanic Complex (21,84°S; 68,20°W) and the nearby young dacitic domes (Chanka, 21,78°S; 68,31°W - Chac-Inca, 21,80°S; 68,21°W - Pabellón, 21,84°S; 68,15°W) are located about 100 km NE of the city of Calama and about 55 km NW of the El Tatio geothermal field, near the international border between Chile and Bolivia (Fig. 2.1a). Based on the NW–SE alignment of the APVC centres, Davidson and de Silva (1992) and de Silva et al. (1994) suggested that the principal volcanic features are controlled by a series of NW-striking faults, an association that can also be recognized in the study area. This sector is tectonically characterized by the presence of two major faults with converging dips, characterized by 50-150 m high scarps which form a NW-oriented symmetric graben, ~4 km wide and ~20 km long (Pabelloncito graben; Francis and Rundle, 1976). This structure was formed during a Late Pliocene-Quaternary extensional phase (Tibaldi et al., 2009), and has been linked by Tibaldi and Bonali (2018) to gravity spreading of the Pliocene-Pleistocene aged Palpana-Inacaliri volcanic chain (Wörner et al., 2000; Sellés and Gardeweg, 2017). The young dacitic domes of Chanka, Chac-Inca and Pabellón were emplaced along this extensional structure, beside the AAVC and the Cerro del Azufre volcano, this latter being still active in the late-glacial period (de Silva and Francis, 1991). Both the AAVC and the dacitic domes overlay an Eocene-Miocene basement, made up of a sequence of andesitic lava flows, conglomerates, breccias, sandstones, limestones and gypsum formations (Ramírez and Huete, 1981). Over this basement, Miocene ignimbrites and andesitic lava flows (7.5 ± 0.6 Ma, and 6.7 ± 0.3 Ma, respectively; Rivera et al., 2015) are exposed. The AAVC is mainly characterized by andesitic, dacitic and rhyolitic products (Piscaglia, 2012). Its magmatic history has been divided into two main eruptive periods (Mercado et al., 2009; Piscaglia, 2012): a Middle Pleistocene phase that involved the building of the Apacheta stratovolcano and a Mid-Upper Pleistocene phase when the Aguilucho stratovolcano formed. The first phase is constrained by the ages of the Aguilucho ignimbrite (1.024 ± 0.033 Ma, that despite the name pertains to the Apacheta activity; Sellés and Gardeweg, 2017), and of a dacite lava flow (0.91 ± 0.14 Ma; Rivera et al., 2015) (Fig. 2.1b). Conversely the second phase is made up by two dacite lava flows of the Aguilucho volcano in the western (0.7 ± 0.2 Ma; Rivera et al., 2015) and northern (0.652 ± 0.012; Sellés and Gardeweg, 2017) flanks (Fig. 2.1b). The domes of this area (Fig. 2.1b) correspond to crystal-rich dacitic flows, with occasional andesitic enclaves, erupted during Upper Pleistocene, with ages obtained for Chanka (119.8 ± 5.4 ka; Tierney et al., 2016), Chac-Inca (114.0 ± 37.0 ka; Rivera et al., 2015) and Pabellón (80.0-130.0 ka according to Renzulli et al., 2006 and 50.0 ± 10.0 ka according to Urzua et al., 2002). La Poruña represents a monogenetic

andesitic scoria cone with a ~8 km long lava flow (Fig. 2.1c), dated 103.0 ± 1.1 ka (Wörner et al., 2000).

2.2.2 Altiplano-Puna Magma Body

The Altiplano-Puna Magma Body (APMB) in the Central Andes is the largest known zone of partial melting in the continental crust, spanning a region 200 km in diameter (Fig. 2.1a), at 4-25 km b.s.l. and with an estimated volume of 500,000 km^3 (Ward et al., 2014). The APMB anomaly has been described by magnetotelluric (MT) surveys (Comeau et al., 2015, 2016) as a low-resistivity zone with the top at ~15 km below sea level (defined at 3 Ω·m) due to the presence of andesitic melts with a melt fraction up to 25% (Schilling et al., 2006; Ward et al., 2014; Comeau et al., 2015) and an estimated temperature of ~1000 °C (Comeau et al., 2016). The top of the APMB has been constrained about 5 km deeper than originally reported by Ward et al. (2014), probably due to the low spatial resolution of ambient noise tomography, because of the long wavelengths of the seismic waves used, or to the possibility that the materials between ~4-15 km b.s.l. really do have a low seismic velocity but relatively high resistivity compared to the APMB (Pritchard and Gregg, 2016). The maximum thickness of the APMB seismic anomaly from the joint analysis of ambient noise tomography and receiver functions used by Ward et al. (2014) is ~11 km, defined through shear waves velocity (Vs) of 2.9 km/s, because velocities below this value clearly imply partial melting (Ward et al., 2014). An isostatic residual gravity field (Götze et al., 1994; Götze and Krause, 2002) reveals also a strong negative anomaly that supports an extensive low-density area beneath the APVC, centred in southern Bolivia under the Uturuncu volcano, and a dense grid of observations and new models have produced a range of plausible shallower low-density structures, interpreted as diapiric columns of partially molten rock that connect the APMB with putative shallow-level magma storage regions (Annen et al., 2015) constrained by experiments and melt inclusions (del Potro et al., 2013; Muir et al., 2014). S-wave velocities indicate an increase in melt/fluid percentage from the margin to the center of the partially molten body from ~4% for zones with S-velocities of 3.2 km/s, to ~10% (2.9 km/s), and up to 25% in zones with velocities <1.9 km/s (Ward et al., 2014). This variation, in the Western margin of the anomaly, is emphasized by the different degree of contamination of the erupted magmas that pass through the APMB and present a lateral variation of Sr- and Nd-isotope compositions (Michelfelder et al., 2013; Godoy et al., 2017a). The interaction between less differentiated magma and this crystal-rich mush increases from the margins to the center of the anomaly, where crustal assimilation is more significant as magmas interact along the entire mush column (Muir et al., 2014; 2015).

2.3. Sampling and analytical methods

Representative samples from the Apacheta-Aguilucho Volcanic Complex and the dacitic domes (lavas and enclaves) were collected during several field trips, between 2007 and

2017. The sample locations are shown in Figure 2.1b. A total of 27 samples were prepared for major oxides and trace element geochemical analyses; 15 samples were also prepared for isotopic analyses. One sample was prepared for $^{40}Ar/^{39}Ar$ analyses at the Servicio Nacional de Geología y Minería, Chile (SERNAGEOMIN) (additional information is given in Appendix - C2-1). Geochemical analyses of major and trace elements were carried out at Acme Analytical Laboratories Ltd. (ACMElab; Canada) with Inductively Coupled Plasma-Optical Emission Spectrometry (ICP-OES) and Mass Spectrometry (ICP-MS), at Activation Laboratories Ltd. (Actlabs; Canada) with ICP-OES and ICP-MS, and at the University of Cape Town (South Africa) with X-ray fluorescence (XRF). Sr-, Nd- and Pb-isotope analysis were performed at the "Istituto di Geoscienze e Georisorse" - National Research Council (IGG-CNR) in Pisa (Italy) with a TIMS Finnigan MAT 262, and at the University of Cape Town (South Africa) using a NuPlasma HR multicollector-ICP-MS (MC-ICP-MS). A detailed description of the analytical methods is reported in Appendix - C2-1.

2.4. Results

All the sampled and investigated volcanic products were classified based on major oxides whole rock compositions (Table 2.1, from Taussi et al., 2019) and modal mineralogy. All the compositions reported below are normalized to an anhydrous base. Geochronological analysis on the andesitic lava flow outcropping on the Apacheta volcano (Fig. 2.1b) returned a value of 0.97 ± 0.11 Ma, thus in agreement with the Apacheta activity phase. Detailed geochronological results from Taussi et al., (2019) are given in Appendix - C2-2.

2.4.1 Petrography and mineral assemblages

2.4.1.1 Apacheta-Aguilucho Volcanic Complex lavas

The AAVC is mainly characterized by extrusives of the high-K calc-alkaline series (andesites to rhyolites; Fig. 2.2). Andesites (57.7-62.4 wt% SiO_2) show a porphyritic index (P.I.) ranging from 10 to 25 vol.%, with a modal mineralogy consisting of plagioclase, orthopyroxene, clinopyroxene, amphibole, biotite, Fe-Ti oxides and rare olivine. Subhedral olivine, mostly replaced by goethite, hematite and clay minerals (i.e. iddingsite), is found in the less silicic sample (AA-047). Plagioclases have variable sizes; bigger sized crystals (1-2 mm) show resorption and sieve textures with intense zoning, while smaller crystals (<1 mm) generally do not show these textures. Groundmass is micro- to cryptocrystalline to glassy, with the same mineralogical paragenesis as phenocrysts. Dacites (63.1-65.4 wt% SiO_2) are the most abundant products of the AAVC; they are partially vesiculated with porphyritic textures (P.I. = 10-20 vol.%), and contain plagioclase, amphibole, biotite, sanidine, quartz, clinopyroxene, orthopyroxene and Fe-Ti oxides, in decreasing order of abundance. Plagioclase frequently shows disequilibrium features, such as sieve textures and zonings. Amphibole and biotite are

often characterized by breakdown rims consisting of plagioclase, pyroxene ± oxides. Groundmass varies from micro- to cryptocrystalline and consists of plagioclase, alkaline feldspar, and amphibole microlites. Rhyolitic composition is represented only by sample AA-064, which is the most evolved magma erupted in the AAVC (69.6 wt% SiO_2). It has a porphyritic texture (P.I. = 20 vol.%) with convoluted banded textures consisting of lighter and darker-coloured sections. The modal mineralogy is represented by plagioclase, sanidine, amphibole, quartz, biotite, orthopyroxene, clinopyroxene, Fe-Ti oxides and titanite as accessory phase. The groundmass is micro-cryptocrystalline with interstitial devitrified glass and a locally pilotaxitic texture. Plagioclase phenocrysts show inverse and oscillatory zoning. Quartz crystals show rounded edges and are sometimes strongly embayed. Clinopyroxenes represent the most abundant mafic phase. Hydrous minerals are always affected by breakdown textures or secondary alteration processes.

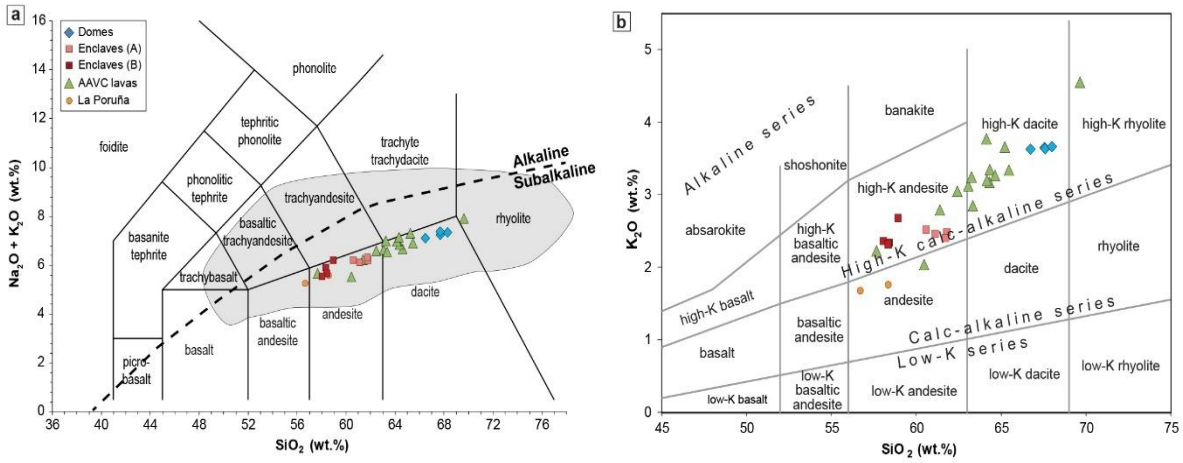

Figure 2.2 *- a) Total-Alkali vs. Silica (TAS) diagram for sampled lavas of the Apacheta-Aguilucho Volcanic Complex, and the domes and enclaves therein (after Le Bas et al., 1986). Lava samples show a well-defined trend, varying from andesitic to rhyolitic in composition; b) K_2O vs. SiO_2 diagram for the same samples as in a) (after Peccerillo and Taylor, 1976). Samples SP1 (Mamani et al., 2008) and POR-10-01 (Godoy et al., 2014) from La Poruña scoria cone are also shown. The grey field represents the composition of Central Andes lavas (after Mamani et al., 2010); while the dashed line separates alkaline and sub-alkaline lavas (after Irvine and Baragar, 1971). Figure modified from Taussi et al. (2019).*

2.4.1.2 Domes

Chanka, Chac-Inca and Pabellón domes are classified as high-K dacites (66.7-68.0 wt% SiO_2; 3.6-3.7 wt% K_2O; Fig. 2.2) with a porphyritic and partially seriate texture (P.I. = 16-23 vol.%). The phenocrysts, in order of abundance, consist of plagioclase, amphibole, biotite, quartz, pyroxene, titanite and Fe-Ti oxides, plus micro-phenocrysts of apatite and zircon as accessory phases (Fig. 2.3a). The groundmasses are micro-cryptocrystalline (with the same mineral assemblage as the phenocrysts), slightly glassy and characterized by perlitic cracks and interstitial devitrified glass. Plagioclase phenocrysts are variable in size with oscillatory

zoning, sometimes with coarse-sieve textures and smooth edges (Fig. 2.3b). Besides the frequent enclaves, the dacitic domes contain portions of a “cryptic” mafic-intermediate component characterized by microlites mainly consisting of plagioclase and amphibole (Fig. 2.3c). Quartz crystals have rounded edges. Hydrous minerals show euhedral to subhedral habits, with the larger sized crystals (up to 2 mm) sometimes affected by intense breakdown that occasionally replaces the entire mineral with pseudomorph assemblages made of plagioclase + pyroxene ± oxides. Accessory phases are frequently hosted as inclusions in hydrous minerals. The contact between the dacite and the enclaves is irregular, crenulated and cuspidate (Fig. 2.3d).

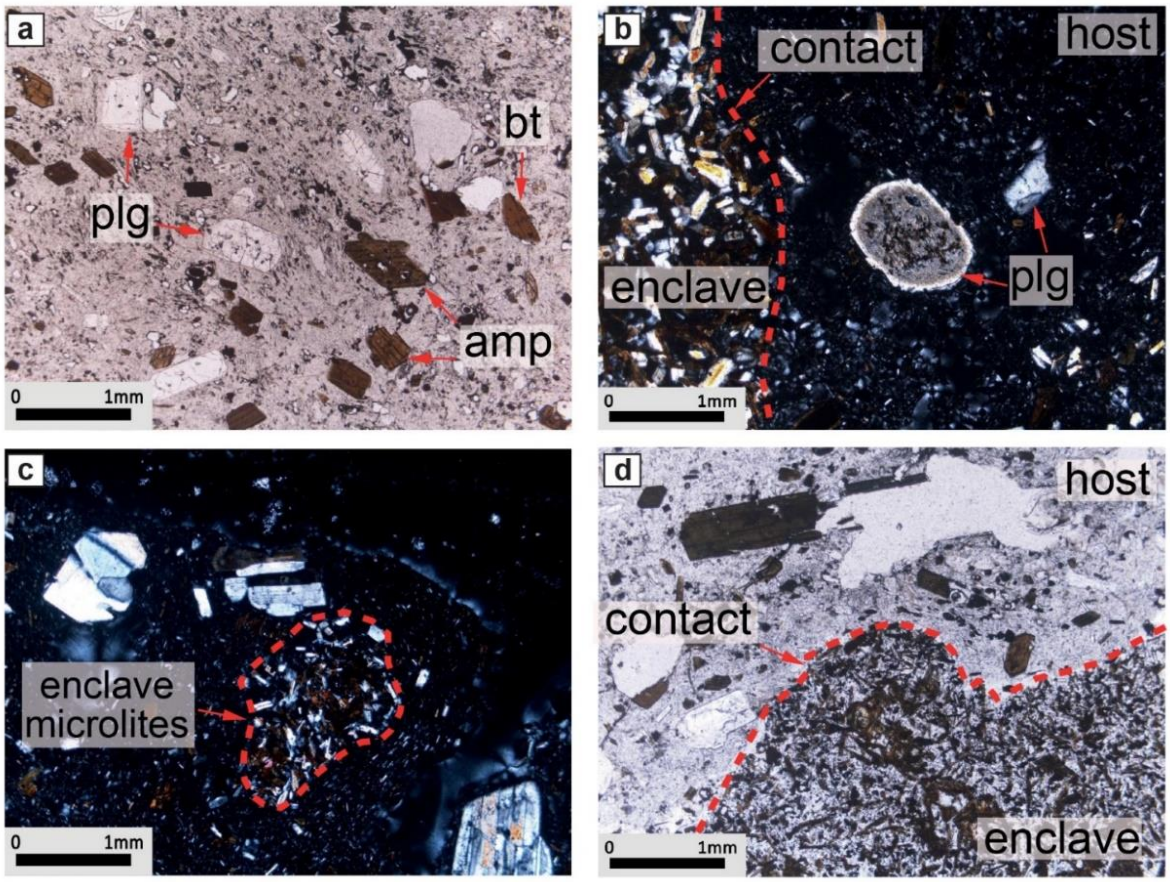

Figure 2.3 *- Photomicrographs showing typical textures of the dacitic domes. a) a representative mineral assemblage composed of a micro-cryptocrystalline groundmass with abundant plagioclase (plg), amphibole (amp) and biotite (bt); b) plagioclase phenocrysts of variable sizes locally showing coarse-sieve texture and smooth edges, the contact between the hosting dacite and the andesitic enclave is also highlighted; c) portions of groundmass microlites mainly consisting of plagioclase and amphibole, texturally compatible with the andesitic enclaves; d) an irregular, crenulated and cuspidate contact between the hosting dacite and the andesitic enclave. Figure from Taussi et al. (2019).*

2.4.1.3 Micro-vesiculated enclaves

All the lava domes contain frequent fine-grained and micro-vesiculated high-K andesitic enclaves (58.1-61.8 wt% SiO_2; 2.3-2.7 K_2O; Fig. 2.2b). They range from 2 up to 20 cm (Fig. 2.4a,b) in size and show a very low P.I. (3-5 vol.%). Different colouration on a mesoscopic scale can be found even within the same enclave (Fig. 2.4c). This is probably due to differences in content and degree of interconnection of the vesicles, since no geochemical (see Table 2.1 for sample CKA1a_ch lighter portion, CKA1b_sc, darker portion of the enclave), mineralogical or petrographic variations were recognized (e.g. modal mineralogy; core-to-rim variations in crystallinity). The crystal assemblage of the enclaves consists of plagioclase, pyroxene, amphibole, biotite, olivine and quartz. The groundmass is characterized by quenched and acicular phases of plagioclase, pyroxene, amphibole and rare biotite and Fe-Ti oxides, arranged in a diktytaxitic-like texture. This texture is constituted by abundant angular interstitial gas cavities between the plagioclase laths (Fig. 2.4d) and variable amount of glass. Although the general mineral assemblages are almost the same for all the analysed enclaves, we observed some peculiar differences which have allowed to distinguish two petrographic types independent of the size of the enclave. The first type, “Type-A” (Fig. 2.4d,e,f), show a very fine-grained texture with small and acicular micro-phenocrysts and widespread vesicles. Xenocrysts assemblages are mostly represented by embayed quartz with rim overgrowths of pyroxene and amphibole, and large-sized plagioclases (up to 3 mm) with sieve textures limited to crystal rims or absent. Olivine crystals are scarce or absent in these enclaves. The second type of micro-vesiculated enclaves, “Type-B” (Fig. 2.4g), show a slightly coarser texture and are mainly characterized by plagioclase xenocrysts with extensive sieve and resorbed textures, and the presence of olivine phenocrysts. Scarce or no quartz xenocrysts is recognized among this type.

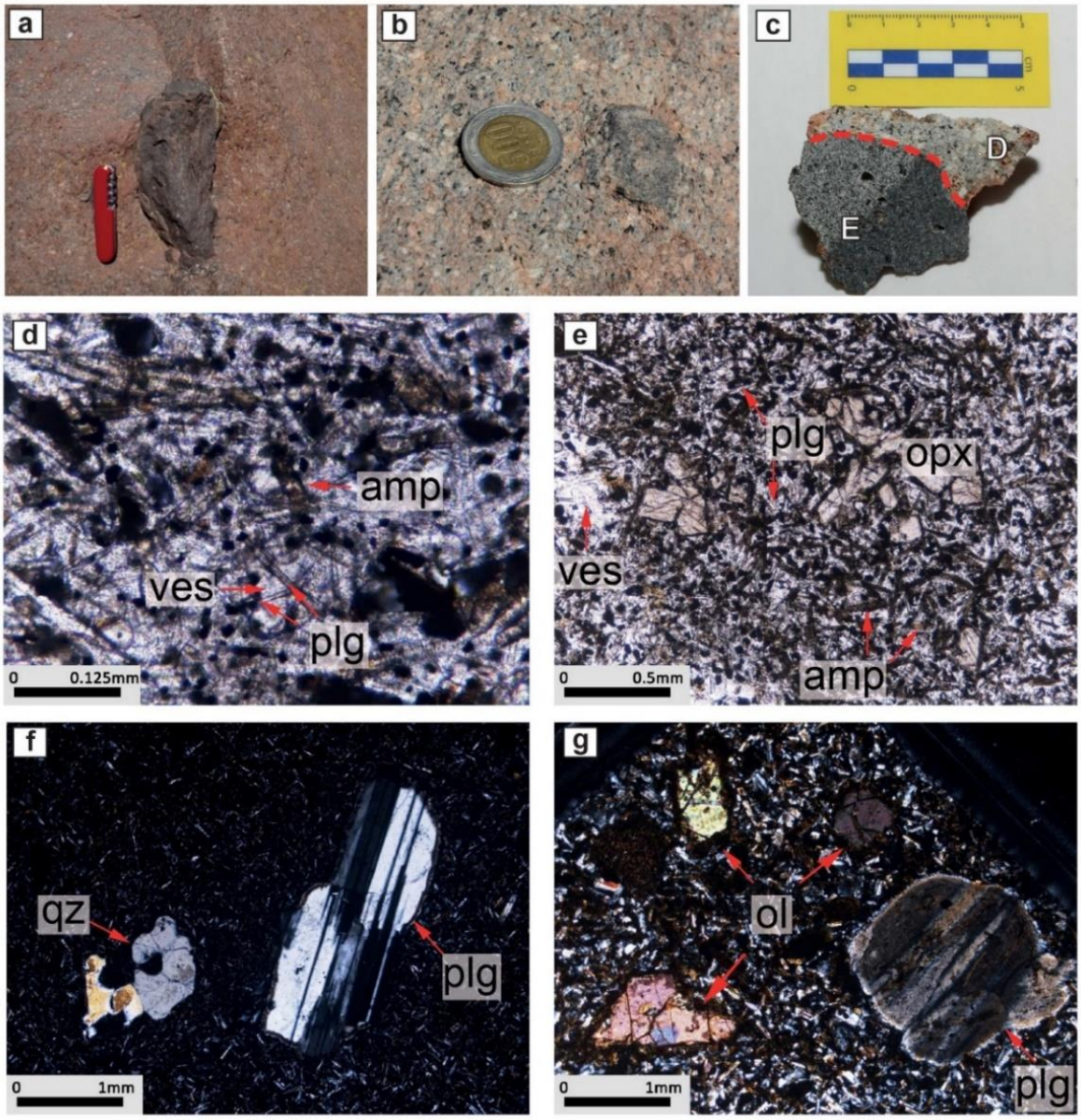

Figure 2.4 *- Micro-vesiculated enclaves within the dacitic domes and photomicrographs showing typical petrographic textures; a) and b) show enclaves of different sizes; c) shows colour difference inside the enclaves themselves, dashed red line mark the contact between the enclave (E) and the dacite (D); d) microphotograph showing the diktytaxitic-like texture of the groundmass of the enclaves with angular vesicles (ves) between plagioclase (plg) and amphibole (amp) laths; e) microphotograph showing a very fine-grained micro-vesiculated groundmass with orthopyroxene (opx) phenocrysts (Type-A enclave); f) microphotograph showing large sized plagioclases with no sieve textures and embayed quartz (qz) in a very-fine micro-vesiculated groundmass of a Type-A enclave; g) microphotograph showing olivine phenocrysts and plagioclase with extensive sieve and resorbed textures in a slightly coarser groundmass, typical of Type-B enclaves. Figure from Taussi et al. (2019).*

2.4.2 Data on major-trace element and Sr-Nd-Pb isotopes

Results of geochemical analyses are summarized in Table 2.1 (from Taussi et al., 2019).

Table 2.1

Major and trace element compositions of domes, enclaves and lava samples from the Apacheta-Aguilucho Volcanic Complex area.

Location	**Chanka**			**Chac-Inca**	
Sample	CKA1	CKA1a_ch	CKA1a_sc	C-INKA1	C-INKA1f
Unit	Dacite	Enclave (A)	Enclave (A)	Dacite	Enclave (A)
Age	0.1198 ± 0.054 Ma[1]			0.114 ± 0.37 Ma[2]	
Coordinates WGS84 19S	569389	569383	569383	582287	582120
	7589334	7589771	7589771	7587947	7587957
Major oxides (wt%)					
SiO_2	65.81	59.62	59.99	66.92	61.02
Al_2O_3	15.08	16.38	15.85	14.98	16.03
$Fe_2O_{3(tot)}$	3.29	6.18	6.11	4.22	5.63
MgO	1.47	3.32	3.37	1.54	3.29
CaO	3.39	5.57	5.62	3.49	5.54
Na_2O	3.54	3.60	3.56	3.58	3.84
K_2O	3.55	2.48	2.42	3.60	2.38
TiO_2	0.46	0.83	0.84	0.50	0.78
P_2O_5	0.12	0.29	0.28	0.12	0.22
MnO	0.06	0.09	0.09	0.07	0.08
LOI	1.99	1.09	1.55	0.48	1.29
Sum	98.75	99.45	99.67	99.50	100.11
Trace elements (ppm)					
V	70	144	141	81	139
Cr		90	90	40	70
Co	7.0	15	15	8.0	14
Ga	18	19	20	17	20
Rb	175	73	73	181	63
Sr	342	526	533	366	580
Y	13	15	14	13	13
Zr	139	161	155	147	169
Nb	10	8.0	8.0	10	7.0
Sn	2.0	2.0	1.0	2.0	1.0
Cs	13	3.3	3.1	13	2.2
Ba	671	794	809	692	829
La	32	26	26	35	29
Ce	61	53	54	66	58
Pr	6.5	6.2	6.2	7.0	6.7
Nd	22	23	23	24	25
Sm	3.9	4.6	4.6	4.5	4.9
Eu	0.83	1.1	1.2	0.83	1.2
Gd	3.0	3.8	4.1	3.2	3.8
Tb	0.40	0.50	0.60	0.50	0.50
Dy	2.4	3.0	3.0	2.6	2.9
Ho	0.50	0.50	0.50	0.50	0.50
Er	1.3	1.4	1.5	1.4	1.5
Tm	0.18	0.19	0.19	0.21	0.20
Yb	1.4	1.3	1.3	1.4	1.3
Lu	0.23	0.20	0.22	0.22	0.21
Hf	3.8	3.8	3.7	4.4	4.0
Ta	1.4	0.70	0.70	1.3	0.60
Tl	0.80	0.40	0.40	0.90	0.30
Th	32	9.5	9.3	32	7.2
U	11	3.1	2.9	10	2.1
Be	3.0	2.0	2.0	3.0	2.0
Ni		20		40	
Cu		10	20	20	20
Zn	60	90	80	70	90
As	12	7.0	10	12	
Pb	20	12	12	21	12
Sc	7.0	14	14	8.0	14

Table 2.1

(continued)

Location	**Cerro Pabellón**					
Sample	AA003	CPB1	AA001	ICP16	ICP22	ICP24
Unit	Dacite	Dacite	Enclave (B)	Enclave (B)	Enclave (A)	Enclave (B)
Age	0.08 - 0.13 Ma[3]					
Coordinates WGS84 19S	587826 7584239	587232 7584266	587826 7585104	587562 7584075	587562 7584075	587562 7584075
Major oxides (wt%)						
SiO_2	64.80	66.37	57.33	57.33	61.69	57.23
Al_2O_3	15.49	15.12	17.06	15.98	16.46	16.22
$Fe_2O_{3(tot)}$	3.90	3.55	6.22	7.35	5.93	7.31
MgO	1.71	1.60	3.66	4.68	3.10	4.01
CaO	3.53	3.65	5.72	6.84	5.32	6.57
Na_2O	3.41	3.65	3.42	3.14	3.70	3.25
K_2O	3.53	3.56	2.60	2.33	2.48	2.29
TiO_2	0.54	0.47	0.89	0.76	0.82	0.78
P_2O_5	0.15	0.14	0.25	0.20	0.22	0.17
MnO	0.06	0.06	0.09	0.11	0.08	0.11
LOI	3.11	1.67	1.89	1.16	0.96	1.01
Sum	100.23	99.84	99.13	99.88	100.76	98.95
Trace elements (ppm)						
V	87	73	157	176	138	171
Cr	20	24	80	210	80	80
Co	9.0	7.0	16	22	14	18
Ga	20	18	23	17	19	18
Rb	191	172	85	85	81	74
Sr	376	354	630	503	601	542
Y	11	13	14	15	13	16
Zr	139	152	163	120	164	137
Nb	11	12	8.0	6.0	8.0	6.0
Sn	2.0	2.0	2.0	1.0	2.0	2.0
Cs	13	14	3.1	3.5	3.3	3.1
Ba	707	688	813	581	812	667
La	35	32	29	19	28	26
Ce	66	57	59	41	59	50
Pr	6.2	6.3	6.3	4.6	6.8	5.6
Nd	24	22	27	18	25	21
Sm	3.9	4.1	5.1	3.8	4.9	4.2
Eu	0.89	0.83	1.3	1.0	1.2	1.1
Gd	3.1	3.0	4.0	3.3	3.7	3.6
Tb	0.50	0.40	0.60	0.60	0.50	0.60
Dy	2.6	2.6	3.0	3.1	2.8	3.3
Ho	0.50	0.50	0.60	0.60	0.50	0.60
Er	1.4	1.4	1.6	1.7	1.4	1.8
Tm	0.21	0.22	0.22	0.25	0.20	0.28
Yb	1.4	1.4	1.4	1.7	1.3	1.9
Lu	0.22	0.22	0.21	0.26	0.21	0.29
Hf	3.9	4.8	4.2	3.1	4.2	3.4
Ta	1.4	1.4	0.70	0.50	0.60	0.60
Tl	1.2	1.1	0.70	0.40	0.30	0.40
Th	30	31	8.6	6.7	8.3	8.0
U	10	10	2.5	2.1	2.5	2.4
Be	3.0		2.0	1.0	2.0	2.0
Ni				40	20	20
Cu	20		20	30	30	40
Zn	60		100	90	100	90
As	7.0	14		6.0	6.0	5.0
Pb	13		8.0	11	20	11
Sc	7.0		15	21	14	21

Table 2.1

(continued)

Outcrop	**Cerro Pabellón**	**Apacheta - Aguilucho Volcanic Complex**				
Sample	CPAB-ENC-1	AA-007	AA-023	AA-024	AA-047	AA-050
Unit	Enclave (B)	Dacite	Andesite	Dacite	Andesite	Dacite
Age		0.91 ± 0.14 Ma[2]	Middle Pleistocene[4]	0.91 ± 0.14 Ma[2]	0.97 ± 0.11 Ma[5]	0.91 ± 0.14 Ma[2]
Coordinates WGS84 19S	587081	588670	586495	586495	584937	587346
	7585275	7586793	7585794	7585794	7584092	7579885
Major oxides (wt%)						
SiO_2	57.06	62.05	61.31	62.10	56.22	63.92
Al_2O_3	16.77	16.47	17.02	16.69	18.07	16.48
$Fe_2O_{3(tot)}$	6.65	5.09	5.21	5.13	6.59	4.62
MgO	4.01	2.29	2.27	2.25	3.18	2.07
CaO	6.32	4.69	4.92	4.82	6.76	4.32
Na_2O	3.50	3.60	3.49	3.45	3.35	3.79
K_2O	2.26	2.79	2.99	3.07	2.16	3.32
TiO_2	0.84	0.73	0.72	0.69	0.78	0.63
P_2O_5	0.24	0.19	0.18	0.19	0.24	0.15
MnO	0.09	0.08	0.08	0.08	0.11	0.07
LOI	1.19	1.01	1.60	1.30	2.30	0.40
Sum	98.93	98.99	99.79	99.77	99.76	99.77
Trace elements (ppm)						
V	161	117	107	100.00	155	77
Cr	101	20		20		
Co	49	12	11	11	18	9.9
Ga		20	19	19	19	19
Rb	64	113	122	123	104	139
Sr	641	444	466	450	551	448
Y	19	21	19	18	19	15
Zr	174	173	181	187	147	159
Nb	12	11	12	13	8.0	11
Sn		1.0	1.0	2.0	2.0	2.0
Cs		3.9	7.4	7.1	2.6	5.6
Ba	933	742	679	683	607	655
La		39	33	32	21	30
Ce		78	64	60	41	56
Pr		8.2	8.0	7.7	5.3	6.9
Nd		33	29	28	21	23
Sm		6.0	5.2	5.0	4.0	4.3
Eu		1.2	1.0	1.0	1.0	0.92
Gd		4.9	4.7	4.4	4.0	3.4
Tb		0.70	0.66	0.63	0.61	0.54
Dy		4.0	3.9	3.5	3.7	2.9
Ho		0.80	0.67	0.66	0.80	0.54
Er		2.2	2.0	1.7	2.2	1.5
Tm		0.33	0.33	0.31	0.36	0.25
Yb		2.1	1.9	1.9	2.3	1.6
Lu		0.29	0.29	0.27	0.32	0.24
Hf		4.7	5.6	4.8	3.7	4.4
Ta		1.3	1.2	1.4	0.60	1.2
Tl		0.50				
Th		23	23	22	5.9	23
U		7.5	7.7	7.9	1.2	7.8
Be		2.0	2.0	2.0	2.0	1.0
Ni	12		2.4	1.8	6.0	1.8
Cu	24	40	17	12	33	9.3
Zn	83	90	27	23	30	16
As				1.3		1.5
Pb	9					
Sc	23	12				

Table 2.1

(continued)

Outcrop	**Apacheta - Aguilucho Volcanic Complex**					
Sample	AA-054	AA-055	AA-056	AA-058	AA-064	AA-067
Unit	Dacite	Dacite	Dacite	Dacite	Rhyolite	Andesite
Age	0.91 ± 0.14 Ma[2]	0.91 ± 0.14 Ma[2]	Lower Pleistocene[4]	0.70 ± 0.2 Ma[2]	Middle Pleistocene[4]	0.97 ± 0.11 Ma[5]
Coordinates WGS84 19S	586848 7581446	586588 7582077	582845 7578792	579850 7584178	580225 7583868	581521 7583555
Major oxides (wt%)						
SiO_2	63.33	63.85	62.08	63.98	68.44	58.49
Al_2O_3	16.52	16.23	16.65	16.58	14.75	18.12
$Fe_2O_{3(tot)}$	4.58	4.11	4.61	4.71	2.87	6.10
MgO	1.92	1.86	2.30	2.11	1.15	1.29
CaO	4.30	3.92	4.78	4.49	2.78	4.22
Na_2O	3.33	3.57	3.68	3.78	3.32	3.26
K_2O	3.19	3.57	3.18	3.17	4.46	2.66
TiO_2	0.59	0.57	0.64	0.63	0.38	0.88
P_2O_5	0.17	0.13	0.15	0.15	0.08	0.24
MnO	0.07	0.07	0.07	0.07	0.06	0.04
LOI	1.80	1.90	1.60	0.10	1.50	4.50
Sum	99.80	99.78	99.74	99.77	99.79	99.80
Trace elements (ppm)						
V	94	109	129	127	78	80
Cr	21			34		21
Co	9.3	9.9	12	12	6.1	13
Ga	19	19	21	20	19	20
Rb	147	179	129	152	293	80
Sr	418	409	507	467	273	435
Y	18	20	18	19	23	17
Zr	192	180	167	171	189	153
Nb	14	13	11	12	18	9.1
Sn	3.0	2.0	2.0	2.0	3.0	7.0
Cs	11	13	9.0	6.9	25	1.1
Ba	628	680	743	696	541	659
La	35	35	31	33	52	22
Ce	66	69	61	65	98	45
Pr	8.2	8.4	7.5	7.9	11	5.9
Nd	29	27	25	27	34	22
Sm	5.0	5.0	4.8	4.9	5.6	4.3
Eu	0.96	0.95	1.0	1.0	0.80	1.2
Gd	4.5	4.0	3.7	4.0	4.4	3.7
Tb	0.61	0.67	0.61	0.66	0.72	0.60
Dy	3.3	3.4	3.4	3.4	3.7	3.1
Ho	0.62	0.66	0.62	0.68	0.78	0.65
Er	1.9	1.9	1.7	1.9	2.2	1.8
Tm	0.31	0.32	0.29	0.32	0.37	0.28
Yb	1.8	2.0	1.8	2.1	2.4	1.7
Lu	0.29	0.29	0.27	0.30	0.37	0.24
Hf	5.4	5.8	5.2	5.5	7.0	4.4
Ta	1.6	1.5	1.0	1.3	2.4	0.60
Tl	0.20	0.20			0.20	
Th	32	33	21	25	57	4.5
U	10	12	7.4	9.1	23	1.2
Be	3.0	2.0	1.0	2.0	4.0	1.0
Ni	3.7	3.1	2.7	4.4	3.2	6.5
Cu	11	17	17	20	19	45
Zn	38	33	30	25	18	32
As		0.80		0.80	1.3	
Pb						
Sc						

Table 2.1

(continued)

Apacheta - Aguilucho Volcanic Complex				
Sample	AA-077	AA-081	AA-083	AA-094
Unit	Dacite	Dacite	Dacite	Andesite
Age	Pleistocene[4]	0.652 ± 0.012 Ma[4]	Pleistocene[4]	1.024 ± 0.033 Ma[4]
Coordinates WGS84 19S	581045 7585154	582405 7587497	584711 7585422	579434 7579884
Major oxides (wt%)				
SiO_2	62.80	63.15	64.65	59.97
Al_2O_3	16.21	16.26	15.90	16.65
$Fe_2O_{3(tot)}$	4.53	4.61	4.28	6.12
MgO	2.10	2.07	2.05	3.97
CaO	4.53	4.60	4.30	6.03
Na_2O	3.57	3.15	3.52	3.46
K_2O	3.10	3.70	3.29	2.02
TiO_2	0.61	0.67	0.58	0.75
P_2O_5	0.15	0.17	0.15	0.16
MnO	0.07	0.07	0.07	0.10
LOI	2.10	1.30	1.00	0.50
Sum	99.77	99.75	99.79	99.73
Trace elements (ppm)				
V	109	118	106	122
Cr	27	14		103
Co	11	11	10	17
Ga	19	20	19	19
Rb	158	169	173	85
Sr	451	475	418	437
Y	19	21	18	20
Zr	161	175	173	156
Nb	12	13	13	11
Sn	2.0	2.0	2.0	4.0
Cs	11	11	13	7.9
Ba	683	737	681	570
La	31	35	36	28
Ce	63	69	70	57
Pr	7.5	8.5	8.2	7.1
Nd	24	28	27	23
Sm	4.7	5.3	4.9	4.9
Eu	0.99	1.1	0.99	1.0
Gd	3.9	4.4	3.8	4.2
Tb	0.64	0.71	0.60	0.70
Dy	3.3	3.5	3.3	3.8
Ho	0.66	0.71	0.60	0.73
Er	1.7	2.1	1.7	2.0
Tm	0.28	0.34	0.26	0.32
Yb	1.9	2.0	1.7	2.0
Lu	0.27	0.32	0.25	0.29
Hf	5.3	5.1	5.4	5.4
Ta	1.2	1.2	1.4	0.90
Tl				
Th	24	26	31	17
U	8.9	8.9	10	5.8
Be	2.0	2.0	2.0	3.0
Ni	2.0	2.4	2.8	4.0
Cu	16	12	18	25
Zn	16	33	28	11
As	0.90			0.90
Pb				
Sc				

Ages from: [1] - Tierney et al. (2016); [2] - Rivera et al. (2015); [3] - Renzulli et al. (2006); [4] - Sellés and Gardeweld (2017); [5] - Taussi et al. (2019)
(A) and (B) indicates Type-A and Type-B enclaves, respectively
Values not shown were not analysed or are below the detection limit.

Lavas from AAVC and from the domes, including the enclaves, display a broad range in SiO_2 content, from 57.7 to 69.6 wt%, and relatively low MgO contents (<5 wt%), with the higher MgO values for the enclaves (3.1-4.7 wt%) and for sample AA-094 (4.0 wt%). Almost all the samples studied (lavas, domes and enclaves) form a uniform trend in most of the bivariate diagrams (Figs. 2.5 and 2.6). There is an evident gap in SiO_2 content between the enclaves and the domes (~4.0 wt%), which is filled by the dacites of the AAVC. SiO_2 has a negative correlation with Fe_2O_3 (Fig. 2.5a), MnO (not shown), MgO (Fig. 2.5b) and CaO (Fig. 2.5c). TiO_2 and Al_2O_3 show negative correlations in lavas and domes (Fig. 2.5d,e); in the enclaves an initial increase in TiO_2 and Al_2O_3 in the less differentiated samples (<59 wt% SiO_2; Type-B enclaves) is followed by a decrease in the more evolved ones (Type-A enclaves). Na_2O vs. SiO_2 (Fig. 2.5f) shows an almost flat pattern, while P_2O_5 vs. SiO_2 diagram shows a scattered trend (not shown). K_2O shows a positive correlation with SiO_2 in the AAVC lavas, showing almost the same values for all the enclaves (2.3-2.7 wt%) and all the domes (3.6-3.7 wt%) (Fig. 2.2b).

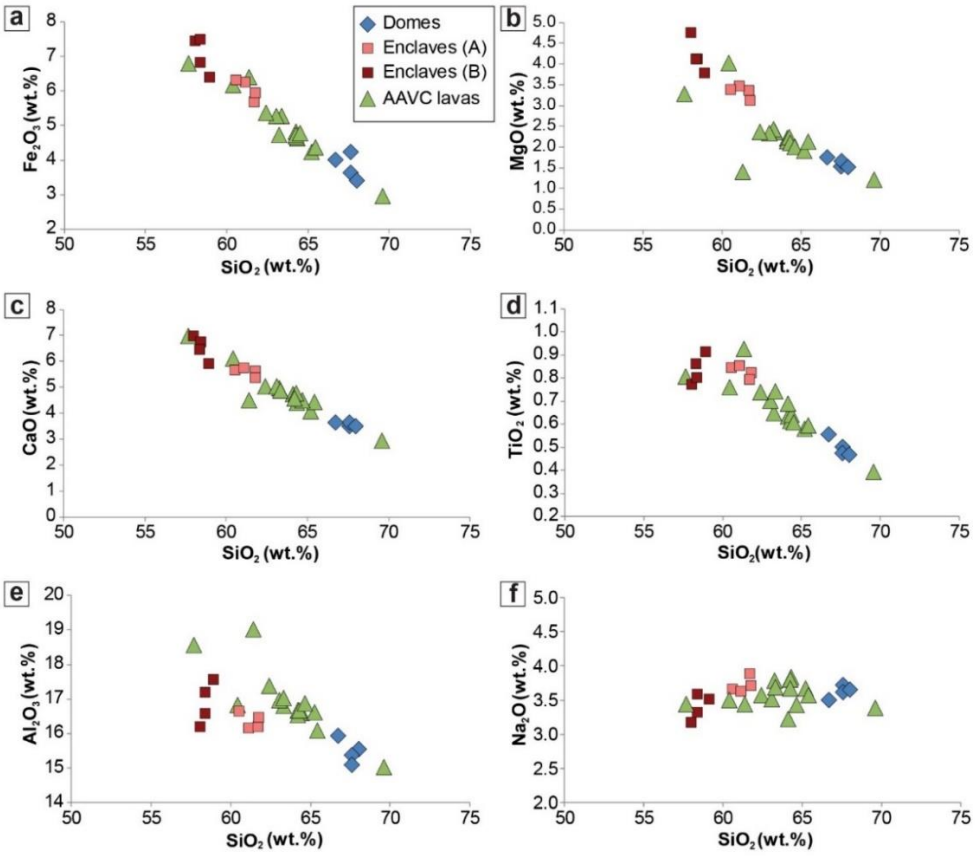

Figure 2.5 *- Major oxides vs. SiO_2 diagrams for sampled lavas of the Apacheta-Aguilucho Volcanic Complex, domes and enclaves therein. Figure from Taussi et al. (2019).*

Selected trace element against SiO_2 concentrations are reported in Figure 2.6. In the enclaves-domes series, Cr content decreases from the enclaves toward the dome lavas (Fig.

2.6a), whereas Rb, Nb, La, Th and U have a positive correlation with SiO_2 (Fig. 2.6b,c,d,e,f). Sr and Ba show similar patterns with an initial scattered pattern in the less differentiated samples (<59 wt% SiO_2), followed by an abrupt decrease toward the most differentiated products (Fig. 2.6g,h). In the AAVC lavas, Sr shows a general decrease (in absolute values) from the andesites to the rhyolite, but an almost stable plateau for the dacites (Fig. 2.6g). Rb, Nb, La, Th and U increase in concentrations with SiO_2 enrichment (Fig. 2.6b,c,d,e,f) while Ba shows no correlation (Fig. 2.6h).

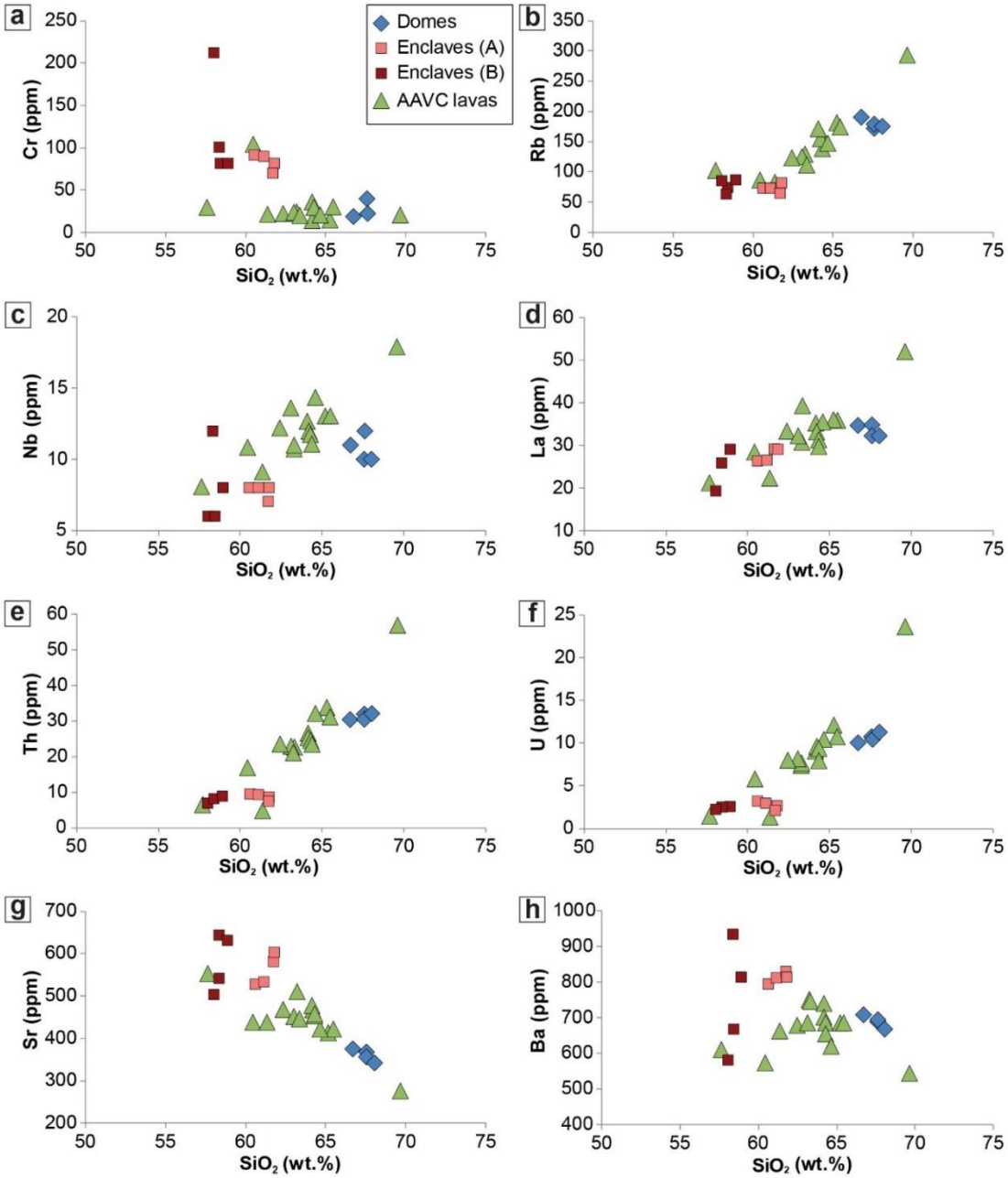

Figure 2.6 *- Trace elements vs SiO_2 diagrams for sampled lavas of the Apacheta-Aguilucho Volcanic Complex, domes and enclaves therein. Figure from Taussi et al. (2019).*

Concerning the patterns of the incompatible elements and REE (normalized to Primitive Mantle and Chondrite, respectively; Fig. 2.7), all the studied samples are within the range of the Central Volcanic Zone field (Mamani et al., 2010). They exhibit a marked enrichment in Cs, Rb, K, Th and U, combined with a marked depletion in Nb, Ta, P and Ti, and a flatter pattern of REE (low LREE/HREE) than most of the other erupted products in the Central Volcanic Zone (Mamani et al., 2010). Their low LREE/HREE ratios are relatively similar to that of the Basaltic-Andesite (BA) end-member (Blum-Oeste and Wörner, 2016), which has been linked to an evolved product of a typical primary arc magma that is generally ubiquitous in the sub-Andean mantle wedge.

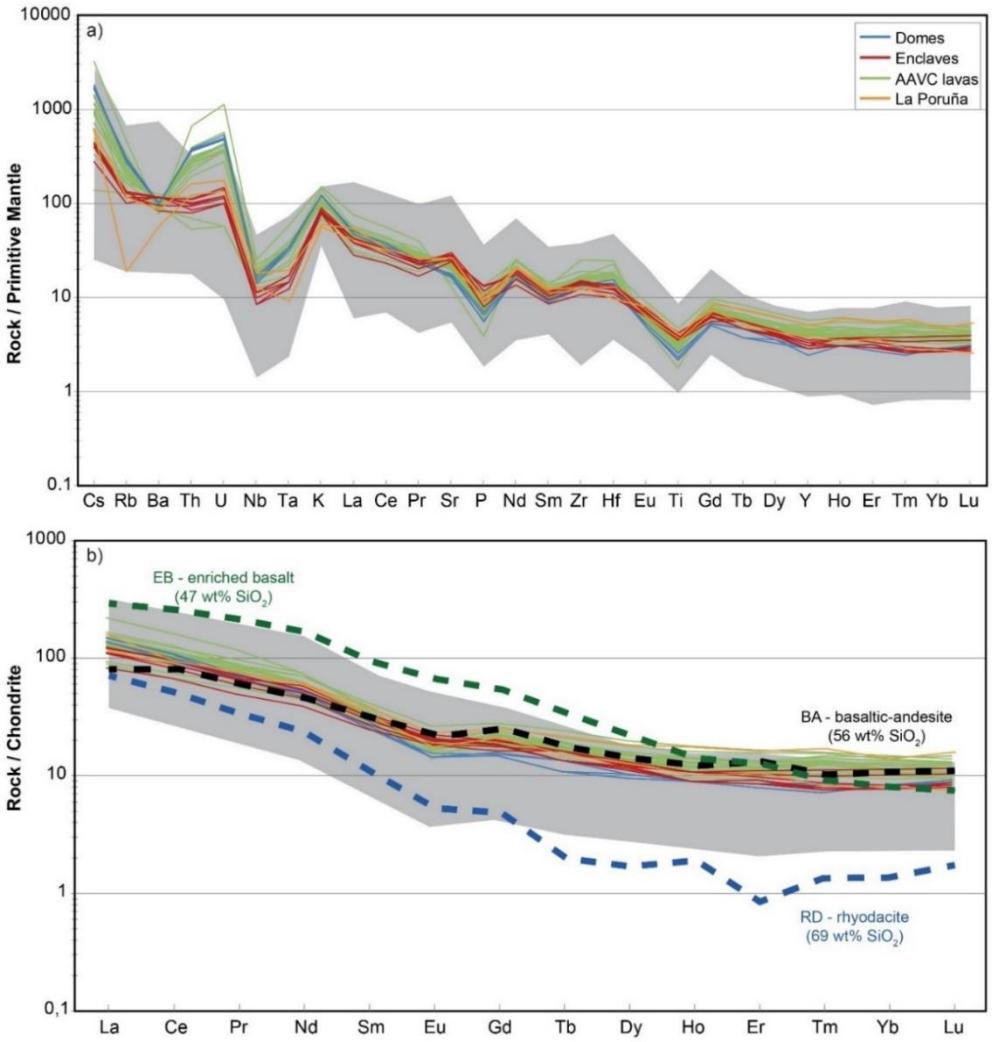

Figure 2.7 *- a) Trace elements normalized to primitive mantle, and b) REE normalized to chondritic values (after Sun and McDonough, 1989) for representative lava samples of Apacheta-Aguilucho Volcanic Complex (green lines), dacitic domes (blue lines), the enclaves (red lines) and La Poruña scoria cone samples from Mamani et al. (2008) and Godoy et al. (2014) (orange lines). Grey areas represent normalized compositions of lavas erupted in the Central Volcanic Zone of the Andes (data after Mamani et al., 2010). End-members for the Central Andean magmatism as defined by Blum-Oeste and Wörner (2016) are shown by thick dashed lines (EB, enriched basalt in green; BA, basaltic-andesite in black; RD, rhyodacite in blue). Figure from supplementary material in Taussi et al. (2019).*

Table 2.2
$^{87}Sr/^{86}Sr$, $^{143}Nd/^{144}Nd$, $^{208}Pb/^{204}Pb$, $^{207}Pb/^{204}Pb$, and $^{206}Pb/^{204}Pb$ isotopic analyses for selected samples.

Unit	Sample	$^{87}Sr/^{86}Sr$	±	$^{143}Nd/^{144}Nd$	±	$^{208}Pb/^{204}Pb$	±	$^{207}Pb/^{204}Pb$	±	$^{206}Pb/^{204}Pb$	±
Chanka											
Dacite	*CKA1*	0.707016	8	0.512313	11	38.7542	9	15.6461	4	18.7914	4
Enclave (A)	*CKA1a_ch*	0.707046	10	0.512303	10	38.8333	17	15.6849	6	18.8159	7
Enclave (A)	*CKA1a_sc*	0.707078	11	0.512297	25	38.7465	13	15.6588	5	18.7973	6
Chac-Inca											
Dacite	*C-INKA1*	0.707013	8	0.512298	13	38.8406	13	15.6726	5	18.8081	6
Enclave (A)	*C-INKA1f*	0.706953	10	0.512302	4	38.7718	20	15.6667	8	18.7801	9
Cerro Pabellón											
Dacite	*AA003*	0.706928	5	0.512308	9	38.8593	340	15.6779	100	18.8151	90
Enclave (B)	*ICP16*	0.706495	7	0.512354	16	38.6150	13	15.6343	5	18.6847	6
Enclave (A)	*ICP22*	0.706919	7	0.512335	41	38.3109	14	15.6367	6	18.3439	6
Enclave (B)	*ICP24*	0.706631	6	0.512330	13	38.6911	31	15.6456	13	18.7475	15
Enclave (B)	*CPAB-ENC-1*	0.706642	11	0.512342	16						
Apacheta-Aguilucho Volcanic Complex											
Andesite	*AA-023*	0.706947	6	0.512319	6	38.8098	340	15.6656	100	18.8015	90
Andesite	*AA-047*	0.706579	8	0.512392	19	38.7783	340	15.6509	100	18.7790	90
Dacite	*AA-055*	0.706962	6	0.512325	8	38.8672	340	15.6736	100	18.8180	90
Dacite	*AA-056*	0.706898	6	0.512332	8	38.7880	340	15.6520	100	18.7991	90
Dacite	*AA-083*	0.707006	8	0.512325	12	38.8822	340	15.6868	100	18.8196	90

$^{87}Sr/^{86}Sr$, $^{143}Nd/^{144}Nd$, $^{206}Pb/^{204}Pb$, $^{207}Pb/^{204}Pb$, and $^{208}Pb/^{204}Pb$ values are summarized in Table 2.2 (from Taussi et al., 2019). In general terms, $^{87}Sr/^{86}Sr$ (0.7065 - 0.7071) and $^{143}Nd/^{144}Nd$ (0.5123 - 0.5124) ratios are comparable to the lavas of the Central Volcanic Zone reported in Mamani et al. (2010) (Fig. 2.8). In the investigated samples, $^{87}Sr/^{86}Sr$ shows an initial increase with SiO_2 in the less evolved products (SiO_2 <60 wt%) to then stabilize at the higher values (Fig. 2.8a); conversely $^{143}Nd/^{144}Nd$ shows a slight decrease from the less silicic samples to the most differentiated (Fig. 2.8b).

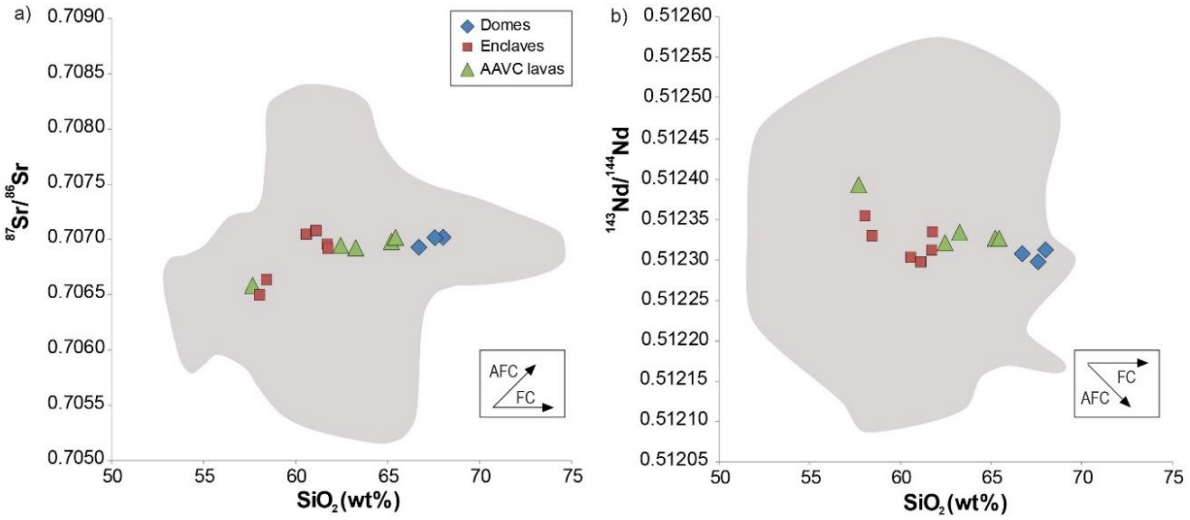

Figure 2.8 *- a) $^{87}Sr/^{86}Sr$ vs. SiO_2 and b) $^{143}Nd/^{144}$ Nd vs. SiO_2 for the studied samples. Assimilation and Fractional Crystallization (AFC) and Fractional Crystallization (FC) trends related to open- and close-system differentiation suggested by Davidson et al. (1991) for the Central Andean magmatism. Grey areas represent the compositional variations of Central Volcanic Zone lavas (data from Mamani et al., 2010). Figure from Taussi et al. (2019).*

The $^{206}Pb/^{204}Pb$ and $^{208}Pb/^{204}Pb$ ratios are > 18.68 and 38.60 respectively (Table 2.2), which is in agreement with the Antofalla Domain values where $^{208}Pb/^{204}Pb$ ratios > 38.50 and $^{206}Pb/^{204}Pb$ ratios > 18.55 (Aitcheson et al., 1995; Mamani et al., 2008, 2010). The only exception is sample ICP22 (Pabellón enclave; Table 2.2), which has lower values ($^{206}Pb/^{204}Pb$ = 18.34; $^{208}Pb/^{204}Pb$ = 38.31), better fitting with the Southern Transition zone to the Arequipa domain (*sensu* Mamani et al., 2010) (Fig. 2.9).

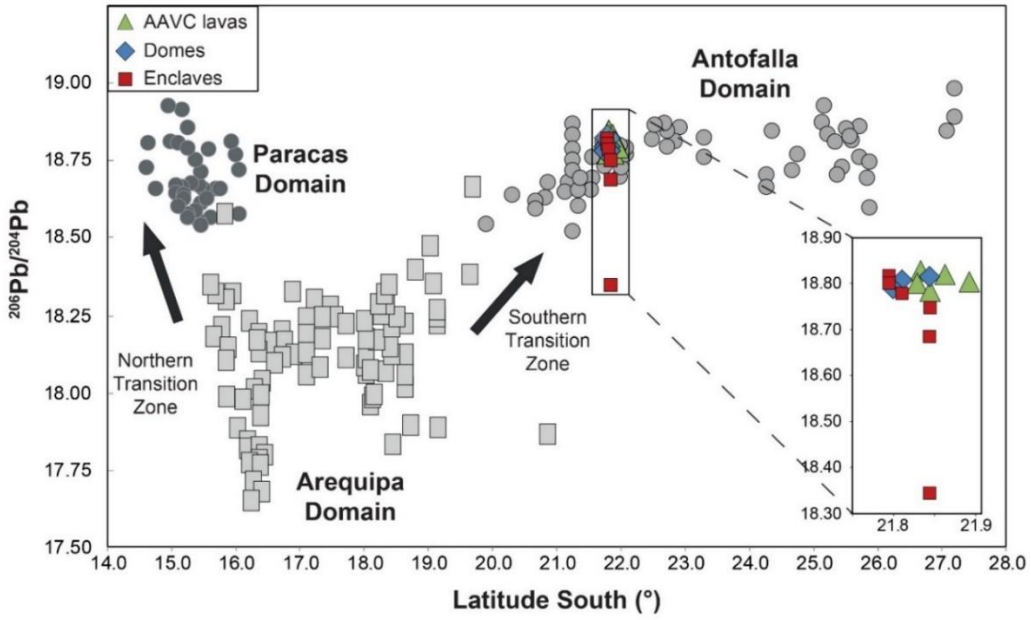

Figure 2.9 *- $^{206}Pb/^{204}Pb$ vs. Latitude South (°) plot for the studied samples and other lavas erupted within the Paracas, Arequipa and Antofalla domains (after Mamani et al., 2010). Figure from supplementary material in Taussi et al. (2019).*

2.5. Discussion

2.5.1 The origin of the enclaves

The irregular, crenulated and cuspate contacts between the host domes (dacitic magmas) and the enclaves (andesitic magmas) (Fig. 2.3d), and the diktytaxitic-like texture recognized in the enclaves (Fig. 2.4), indicate that the origin of these latter is magmatic (liquid-liquid interaction) and that they were quenched during mixing/mingling processes between magmas with different compositions, temperatures and water contents (Bacon, 1986). Furthermore, the presence in the enclaves of crystals inherited from the dacite (i.e. resorbed quartz and large plagioclases) is an evidence of physical mixing between the magmas. In fact, habits, sizes, disequilibrium features and textural relationships of the larger crystals found in the enclaves with respect to the groundmass (Fig. 2.4f,g), suggest that they originated in the hosting dacite and were subsequently embedded by the andesitic enclave (i.e. xenocrysts). This is particularly visible in the Type-A enclaves, showing the presence of large crystals of plagioclase and quartz (i.e. up to 3 mm and 2 mm, respectively; Fig. 2.4f) with few signs of resorption. The above features were also found in the enclaves of other dacitic domes of the Altiplano-Puna Volcanic Complex province (e.g. de Silva et al., 1994; Watts et al., 1999; Burns et al., 2015). In addition, the enclaves have different SiO_2 content, increasing from ~57 wt.% (Type-B) to ~61 wt.% (Type-A) (Table 2.1). This indicates that the Type-A enclaves show a moderate degree of hybridization with the dacite, partially filling the gap of SiO_2 between the Type-B enclaves and the dacitic domes (~66 wt.%). Type-A samples also show higher $^{87}Sr/^{86}Sr$ ratios (~0.7070, i.e. equal to the isotopic signature of the dacite) compared to Type-B samples (~0.7065). We relate the higher silica content, and isotopic signatures of the Type-A enclaves to a higher degree of mixing between these latter and the dacitic magma, which therefore permit a major interaction, coupled with the exchange of more material coming from the dacite (i.e. plagioclase and quartz xenocrysts) that affected the isotopic value. Nevertheless, both types of enclaves show crystallization of similar mineral assemblage, with a marked change on their crystallinity, which varies from fine- (Type-A) to relatively coarser-grained (Type-B) crystals (Fig. 2.4), showing no correlation with the size of the enclaves (Fig. 2.4). Thus, we envisage the interaction between dacitic and andesitic magmas (domes and enclaves therein), in a scenario that implies different crystallinity textures, reflecting different depth of crystallization from the interface andesite-dacite, in a way according to “Model B” by Coombs et al. (2002) (Fig. 2.10). In this model, the andesitic magma ponds and forms an intermediate/silicic interface below the dacitic magma (Fig. 2.10a). This permits the dacite to be remobilized, allowing for mixing in this layer. The andesite cools at different rates depending on its position below the interface (Fig. 2.10b), producing vesicles and consequently decreasing its bulk density, permitting flotation as discrete enclaves (e.g. Eichelberger, 1980;

Coombs et al., 2002). Crystallization and cooling start before disaggregation, thus permitting different crystallinity textures, function of the depth below the interface and independent of eventual enclave size (Fig. 2.10c) (Coombs et al., 2002). This two-stage process (Fig. 2.10b,c) is consistent with a near-interface crystallization for the fine-grained textured samples with the highest degree of interaction and mixing between the different magmas (Type-A), and a faraway crystallization for the slightly coarser textured enclaves (Type-B) (Fig. 2.10b).

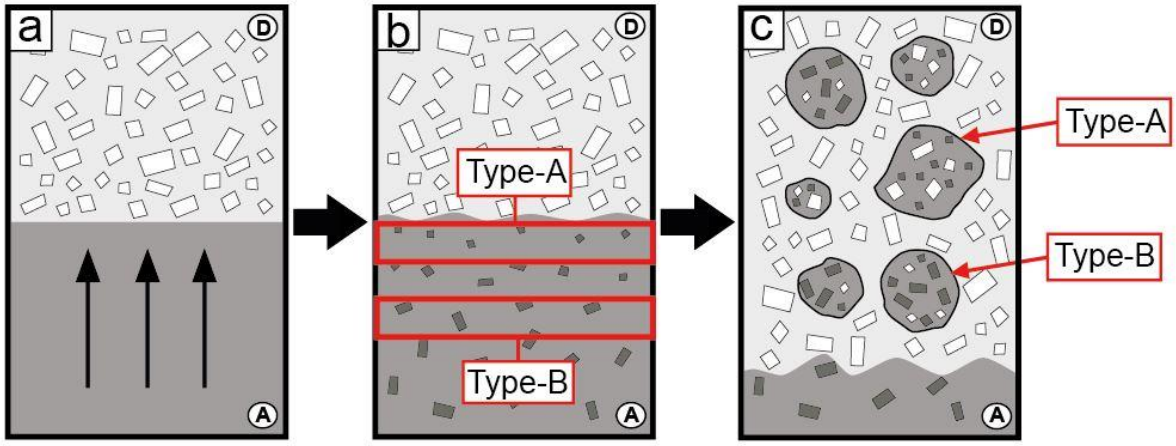

Figure 2.10 *– Interaction model between andesitic (A) and dacitic (D) magmas for the origin of mafic enclaves. a) Andesite influx occurs and a mafic-silicic interface forms; b) crystallization and vapor exsolution proceed within the andesite layer forming minerals of different sizes that increase moving away from the interface, which is reflected in the petrographic characteristics of the enclaves; c) flotation of enclaves occurs due to decreased density of the andesite, resulting in different ranges of crystallinities with no correlation to enclave size (Type-A and Type-B). Type-A and Type-B enclaves incorporate "silicic" xenocrysts during cooling. Modified after "model B" in Fig.10 of Coombs et al. (2002). Figure from Taussi et al. (2019).*

2.5.2 Depth of interaction between andesitic and dacitic magmas

The presence of garnet, amphibole and plagioclase affects the REE profiles of magmas interacting with, or generated in a thickened crust of different depths in different ways (Kay et al., 1999; McMillan et al., 1993; Macpherson et al., 2006). Since Sr and La have a strong affinity for plagioclase whereas Y and Yb prefer garnet and amphibole, the Sr/Y, Sm/Yb, La/Yb and Dy/Yb ratios were plotted versus SiO_2 (Fig. 2.11), as these ratios are particularly sensitive to the presence of garnet and amphibole against plagioclase. The enclaves show the highest values of Sr/Y ratios (Fig. 2.11a) of the entire suite of the studied rocks (Sr/Y range = 33.5-46.2). The lowest values are associated with the AAVC lavas (Sr/Y range = 11.9-29.7) and the intermediate values with the domes (Sr/Y range = 26.3-34.2) and La Poruña (19.5-33.1). In comparison with the Central Volcanic Zone lavas erupted during the last 3 Ma (Fig. 2.11a), these values can be considered low (Mamani et al., 2010). This, coupled with the low Sm/Yb values (enclaves < 3.8; AAVC lavas < 2.9; domes < 3.2; La Poruña < 3.6; Fig. 2.11b), can exclude a "thick crust assimilation" garnet signature (Wörner et al., 2004; Mamani et al., 2010).

Moreover, while La/Yb increases during garnet and amphibole fractionation, garnet fractionation will also increase Dy/Yb, whereas amphibole and titanite fractionation will decrease this ratio (Tiepolo et al., 2002; Macpherson et al., 2006). In the analysed samples, La/Yb shows a positive correlation with SiO_2 (Fig. 2.11c), but the Dy/Yb ratio increases only from the Type-B toward the Type-A enclaves. Conversely, a negative correlation between Dy/Yb and differentiation is recorded for the domes and the AAVC lavas (Fig. 2.11d), consistent with significant amphibole and titanite fractionation, in a garnet-free differentiation environment (Tiepolo et al., 2002; Davidson et al., 2007).

Using the amphibole thermobarometer of Ridolfi et al. (2010) and Ridolfi and Renzulli (2012), Piscaglia (2012) and Gorini et al. (2018) defined two distinct zones of crystallization for magmas erupted at both the AAVC and the dacitic domes. In fact, it was proposed due to polybaric crystallization, that the feeding systems mainly consist of (i) shallow (~4-8 km) magma chambers filled with silicic magma (~740-840°C), which gave rise to the more differentiated lavas of the AAVC and the magmas that generated the dacitic domes; and (ii) deeper levels (~15-20 km) of amphibole crystallization, calculated for an andesite lava flow (~940°C; Gorini et al., 2018). For the enclaves, Gorini et al. (2018) obtained, for few amphiboles crystallized in equilibrium conditions, pressures mainly related to shallow magma chambers (4-8 km) and temperatures akin to the dacites (i.e. ~750-850°C). However, crystallization pressures (~15-20 km) and temperatures (~950-1,000°C) of deeper crustal levels were also found (Gorini et al., 2018). This suggests that andesitic magmas started to crystallize amphibole during their ascent from garnet-free mid-upper crustal levels (~15-20 km) to the shallower crustal levels (~4-8 km), where the massive crystallization and quenching occurred.

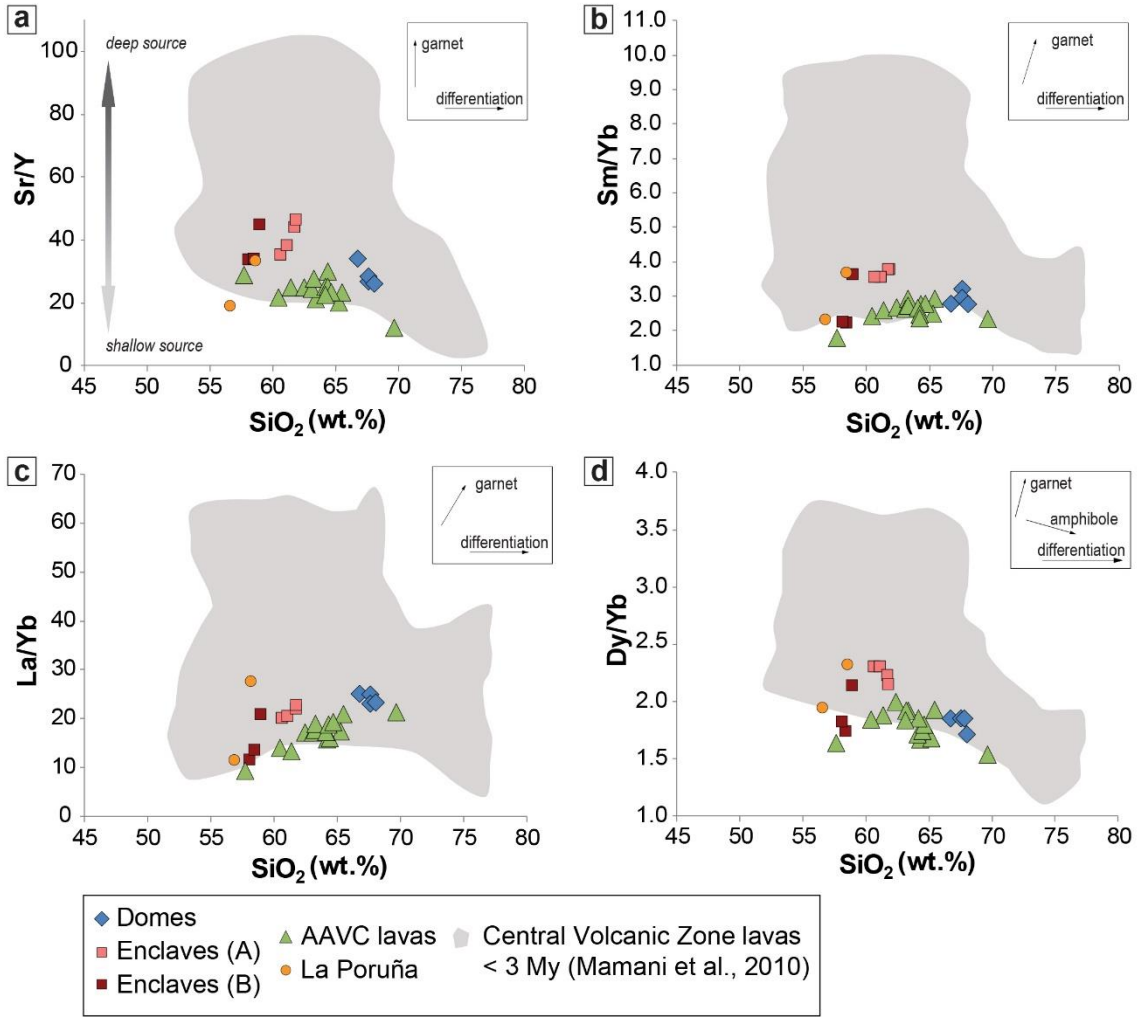

Figure 2.11 *- Plots of Sr/Y (a), Sm/Yb (b), La/Yb (c) and Dy/Yb (d) ratios versus SiO_2 for the domes, the enclaves, the Apacheta-Aguilucho Volcanic Complex lavas and La Poruña scoria cone (sample SP1 from Mamani et al., 2008; sample POR-10-01 from Godoy et al., 2014). Grey fields represent the younger (<3 My) Central Volcanic Zone lavas (after Mamani et al., 2010). Arrows of differentiation trends (with relative mineral contribution) after Mamani et al. (2010). Figure from Taussi et al. (2019).*

2.5.3 Petrological model for evolution of lavas and domes of the Apacheta-Aguilucho Volcanic Complex area

The Altiplano-Puna Magma Body played a significant role in the magmatic plumbing systems of the erupted magmas in the Altiplano-Puna Volcanic Complex. Rising parental magma interacted with this voluminous magmatic body, resulting in strong contamination (Michelfelder et al., 2013; Godoy et al., 2017a). This produced an AFC trend line for the Neogene and Quaternary mafic-to-intermediate erupted products (MgO content ≥ 3.0%) at the surface projection of the Altiplano-Puna Magma Body (data from Hawkesworth et al., 1982; Wörner et al., 1992; Matthews et al., 1994; Feeley and Davidson, 1994; Mattioli et al., 2006; Mamani et al., 2008; Godoy et al., 2014, Michelfelder et al., 2014; Maro et al., 2017), with increasing values of $^{87}Sr/^{86}Sr$ ratios and a slight increase in the Rb/Sr ratio from the margins

toward the centre of the Altiplano-Puna Magma Body (Fig. 2.12a). Above the partially-molten igneous body, the magmas can undergo subsequent stagnation and FC differentiation coupled with mixing/mingling and minor contamination, which occur at shallower levels (~4-8 km, e.g. Burns et al., 2015; Kern et al., 2016; Gorini et al., 2018). This is reflected in the stable $^{87}Sr/^{86}Sr$ ratio (~0.7070) and the increase of the Rb/Sr ratio (Fig. 2.12a). By contrast, all the samples from the Uturuncu volcano (dacites and enclaves; Michelfelder et al., 2014) fall along the AFC line and reach the highest values of the considered dataset (Fig. 2.12a). This is coherent with a strong influence of these processes in the evolution of magmas (Sparks et al., 2008; Michelfelder et al., 2014) at this location (i.e. at the centre of the Altiplano-Puna Magma Body), which hence suggests large crustal contributions derived from the interaction within the maximum thickness of the Altiplano-Puna Magma Body (Muir et al., 2014; 2015; Godoy et al., 2017a).

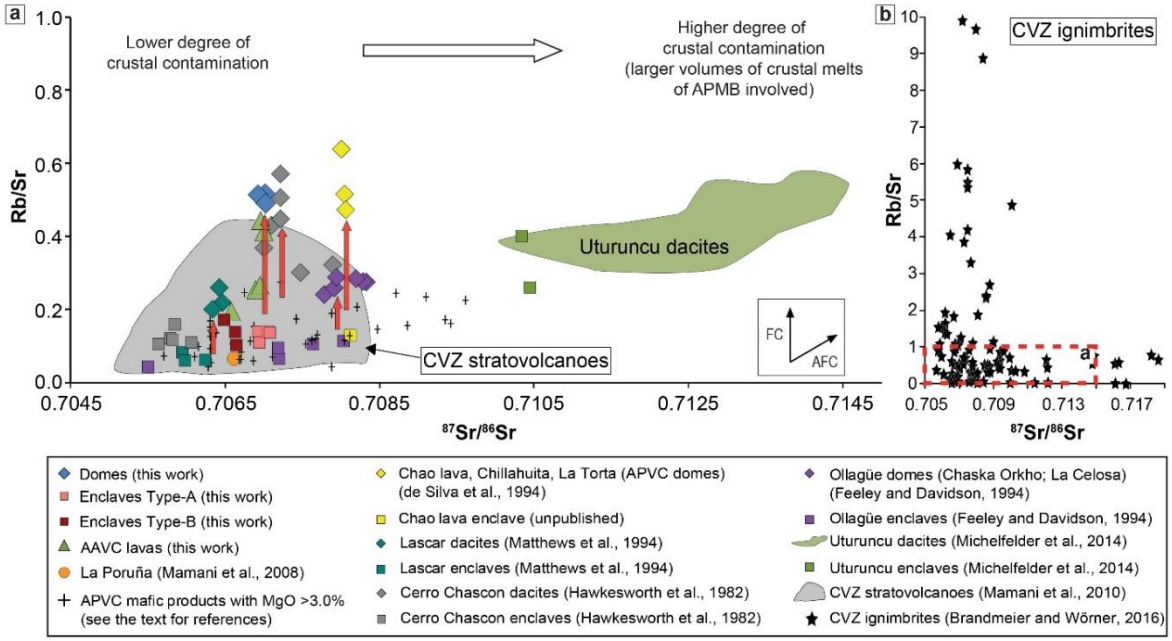

Figure 2.12 *– Plots of Rb/Sr vs. $^{87}Sr/^{86}Sr$. a) Shows an AFC trend line along which all the mafic-intermediate products (MgO > 3.0 wt%) of the Altiplano-Puna Volcanic Complex lie, including the enclaves studied in this work. The values of both Rb/Sr and $^{87}Sr/^{86}Sr$ increase with increasing degree of interaction with the partially molten Altiplano-Puna Magma Body. The more evolved rocks represented by the domes form vertical trends defined by FC-dominant process. The Apacheta-Aguilucho Volcanic Complex lavas fall in the between the enclaves and the domes. The AFC and FC trends are also visible for the Lascar, Ollagüe, Cerro Chascon, Chao lava, Chillahuita and La Torta products reported for comparison, while all the Uturuncu rocks (both enclaves and dacites) lie on the AFC trend. Grey field represents the Central Volcanic Zone stratovolcano values (Mamani et al., 2010). b) Central Volcanic Zone ignimbrite values from Brandmeier and Wörner (2016). Figure from Taussi et al. (2019).*

Based on the geochemical and isotopic compositional variations, a petrological evolution has been conceived for lavas erupted in the AAVC area. To assess these different processes an AFC-type petrological model (DePaolo, 1981) was developed (Table 2.3 from Taussi et al., 2019; Fig. 2.13). We selected a sample from the Lascar volcano (Table 2.3),

which has a low Sr-isotope ratio (~0.7057) (Matthews et al., 1994), corresponding to the isotopic baseline values of MASH-magmas derived from the lower crust (0.705; *sensu* Davidson et al., 1991) and akin with the Sr-isotope composition of the basaltic-andesite (BA) end-member of Blum-Oeste and Wörner (2016). As contaminant we used a bulk felsic upper crustal composition (i.e. gneiss) derived from samples of the Palaeozoic Andean basement from the zone outcropping NE of the studied area, that corresponds to the northern Sierra de Moreno (Lucassen et al., 2001; Table 2.3). For the AFC-model calculations, mineral assemblages were generated by taking into consideration the petrographic characteristic of the enclaves (Table 2.3). The first evolutionary stage is characterized by dominant crustal contamination at middle-upper crustal levels where processes occur in an open-system ($^{87}Sr/^{86}Sr$ increase from ~0.7065 to ~0.7070; Figs. 2.8a and 2.13).

Table 2.3
AFC-type model parameters (after DePaolo, 1981) for erupted magmas at Apacheta-Aguilucho Volcanic Complex. Bulk D according to partitioning coefficients from Rollinson (1993) for basaltic melts. Mineral assemblage according to petrographic characterization of the enclaves reported in Gorini et al., 2018 and in this work).

	Initial	Contaminant	Mineral assemblage	Model 1 (% vol)	Model 2 (% vol)
Location	Lascar volcano	Sierra de Moreno	Plagioclase	45	60
Reference	Matthews et al. (1994)	Lucassen et al. (2001)	Amphibole	30	40
Sample	LA123	3/291	Clinopyroxene	10	
SiO_2 (wt%)[a]	57.55	68.80	Orthopyroxene	10	
Al_2O_3 (wt%)[a]	17.10	13.41	Olivine	5	
CaO (wt%)[a]	7.11	2.72			
Na_2O (wt%)[a]	3.64	3.20	D^{Sr} (bulk)	0.84	1.1
K_2O (wt%)[a]	1.55	1.64			
MgO (wt%)[a]	3.78	1.94			
FeO_t (wt%)[a]	6.36	5.93	Conditions		
Sr (ppm)	711	271	$r = M_a/M_c$	0.6	
$^{87}Sr/^{86}Sr$	0.705765	0.721843			

t = total Fe as Fe^{2+}.
[a] Recalculated 100% water free.

The contamination happens at garnet-free shallow levels (Fig. 2.11) and is likely enhanced by assimilation of the partially melted Altiplano-Puna Magma Body (Fig. 2.12) located at about 15-20 km of depth (Chmielowsky et al., 1999; Zandt et al., 2003; Ward et al., 2014). After assimilation of the partially melted upper crustal layer, a second stage of FC and mixing between the dacitic and the andesitic magmas occurs. This stage represents the main processes occurring in the shallow magmatic chambers at the Apacheta-Aguilucho Volcanic Complex area (~4-8 km depth; Gorini et al., 2018), characterized by plagioclase fractionation (Sr starts to decrease from samples with > 63 wt% SiO_2) and small contamination ($^{87}Sr/^{86}Sr$ slightly increase) (Fig. 2.13).

In the petrological model (Fig. 2.13), evolution of analysed samples runs from the composition of the less-evolved magmas (enclaves) towards more differentiated compositions (domes), passing through the intermediate compositions of the analysed AAVC lavas. This

suggests that these latter are associated to mixing between andesitic and dacitic magmas, that occurred at shallow crustal levels (~4-8 km). Additionally, published ages of the volcanic products indicate that the AAVC lavas were erupted prior the dacitic domes (Urzua et al., 2002; Renzulli et al., 2006; Rivera et al., 2015; Tierney et al., 2016; Sellés and Gardeweg, 2017). As complete hybridization can only occur when the magmas both behave as liquids at the same temperature, and formation of the enclaves occurs when there is a large temperature difference between the magmas or a large proportion of silicic magma (e.g. Sparks and Marshall, 1986; Lesher, 1990), we propose that a thermal change occurred before eruption of the dacitic domes. Thus, during evolution of magmas erupted throughout the formation of the Apacheta and Aguilucho stratovolcanoes (i.e. ~1.0 to ~0.6 Ma), the thermal conditions of andesitic and dacitic magmas were similar, allowing mixing between both end-members (Figs. 2.5 and 2.6). By contrast, during eruption of the dacitic domes (i.e. ~150-100 ka), the thermal differences were significant, preventing mixing and allowing mingling and the extrusion of the domes with the observed enclaves (Fig. 2.10).

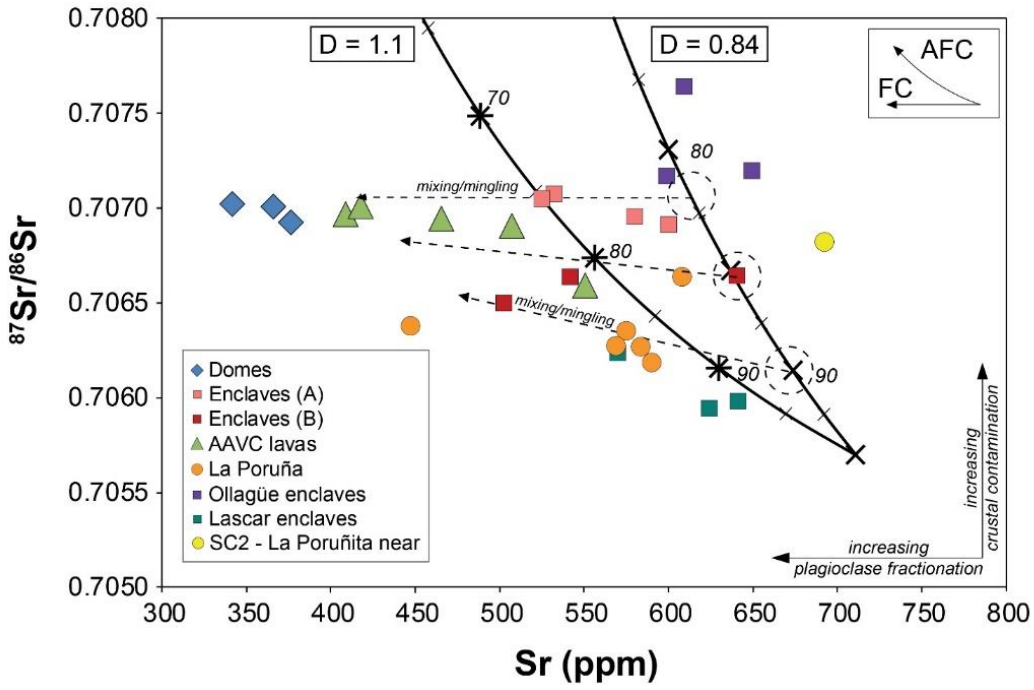

Figure 2.13 *- $^{87}Sr/^{86}Sr$ vs. Sr (ppm) diagram showing the isotopic distribution of lavas from the AAVC area and La Poruña scoria cone. Black, bold lines represent plagioclase-dominated AFC-type (DePaolo, 1981) evolution models taking into account samples from Sierra de Moreno basement (3/291; Lucassen et al., 2001), and Lascar volcano (LA 123; Matthews et al., 1994) as contaminant and initial end-members, respectively (Table 2.3). Italic numbers indicate the remaining melt fraction (F). D indicates bulk partitioning coefficients of Sr according to the crystallizing mineral assemblage of Table 2.3 and mineral partitioning coefficients of Rollinson (1993). The enclaves follow AFC trends, involving mixing/mingling processes (dashed lines) starting from different possible batches of less-differentiated magmas toward the dacitic domes samples. The AAVC samples follow a linear trend similar to FC plus mixing paths. La Poruña, SC2 Poruñita-near sample, Ollagüe and Lascar enclaves are plotted for comparison (Godoy et al., 2014, 2017a; Mattioli et al., 2006; Feeley and Davidson, 1994; Matthews et al., 1994). Figure from Taussi et al. (2019).*

2.5.4 The youngest dacitic domes in the framework of the Altiplano-Puna Volcanic Complex

Similarly to other young dacitic systems of the Altiplano-Puna Volcanic Complex (e.g. Chao lava, Cerro Chascon-Runtu Jarita, La Torta, Chillahuita, and Cerro Chascon; de Silva et al., 1994; Watts et al., 1999; Burns et al., 2015), the magmas erupted by Chanka, Chac-Inca and Pabellón lava domes were in an advanced stage of evolution (high porphyricity, high viscosity), and therefore it seems very unlikely that they would have been erupted without some trigger process. As injection of less-evolved magmas in a more silicic magma chamber is a common mechanism for triggering volcanic eruptions (e.g. Sparks et al., 1977; Murphy et al., 1998; Pritchard et al., 2013), we therefore propose that the interaction between the shallow dacitic crystal-mushes and uprising andesitic magmas produced quenching and vesiculation of the higher temperature magma (Fig. 2.10), enhancing the extrusion of the long-steady magmas originating the dacitic domes within the AAVC area (Fig. 2.14). In addition, bulk composition, mineralogical and isotopic characteristics of these domes, resemble those of the ignimbrites erupted during the flare-up phases (de Silva et al., 1994; Watts et al., 1999; Salisbury et al., 2011; Burns et al., 2015). The vertical trends marked by the APVC domes in the Rb/Sr plot (Fig. 2.12a) runs from the Central Volcanic Zone stratovolcanoes field to the ignimbrites field (Fig. 2.12b). Such features suggest that the formation of these dacitic magma chambers required a thermal history within a magmatic system of super-eruption scale with a vigorous plutonic system feeding these chambers for hundreds thousand years prior to eruption (Tierney et al., 2016; Kern et al., 2016). Finally, also phase petrology of the Altiplano-Puna Volcanic Complex ignimbrites indicate that magmas were stored pre-eruptively over a depth range from about 3 km to 8 km (e.g. Lindsay et al., 2001; Schmitt et al., 2001; de Silva et al., 2006; Burns et al., 2015; Grocke et al., 2017) and therefore the shallow crystal-mushes represented by the youngest domes can be associated to remnant ignimbrite magmas of the Altiplano-Puna Volcanic Complex, produced during earlier magmatic stages.

2.6. Summary and conclusions

A polybaric upper crustal magma plumbing system has been working during the ~1 Ma span time of activity of the AAVC area, with two distinct reservoirs (Fig. 2.14). The deeper reservoirs were located at mid-crustal levels (15-20 km) and are akin to the location given for the Altiplano-Puna Magma Body (Godoy et al., 2014; 2017a; Ward et al., 2014; Burns et al., 2015; Comeau et al., 2015, 2016), involving AFC processes with a dominant role played by amphibole fractionation. Shallower magma chambers were located at depth of 4-8 km (Burns et al., 2015; Gorini et al., 2018) allowing further differentiation of the erupted magmas through FC processes, mainly dominated by plagioclase crystallization.

The concept of different “magmatic regimes” in a trans-crustal magma system may help to better understand the high variability of different types of volcanoes in the Central Andes, from building of andesite-dacite composite cones (steady-state regime) to dominantly large-scale ignimbrites and caldera complexes (flare-up regime; de Silva and Kay, 2018 and references therein). Nevertheless, the magmatic regimes may change back-and-forth from one extreme to the other depending on the rate of mafic recharge and the size and temperature of resident, evolved magmas at shallow levels (Wörner et al., 2018 and references therein). In the evolution of the AAVC area we can envisage a transition of the magmatic regimes from flare-up mode (about 1 Ma; Fig. 2.14a) to steady state (1-0.6 Ma; Fig. 2.14b). This latter magmatic regime characterized by decreasing, but still relatively high rates of mafic magmas recharges for at least 0.4 Ma, kept the upper crustal reservoirs thermally “fertile”, allowing mixing between the new higher temperature magmas with the older, lower-temperature silicic resident magmas to form the abundant andesites and dacites lavas of the composite cones of Apacheta and Aguilucho (Fig. 2.14b). At about 150-100 ka, i.e. the age of the youngest domes, the flux magmatism in the Altiplano-Puna Volcanic Complex had to be already diminished as no MASH processes could occur in the upper crust. In this way, a different magmatic stage could be hypothesized with inputs of basaltic-andesite magmas into the shallower dacitic chambers, leading to triggering the extrusion of the domes rather than complete mixing and hybridization (Fig. 2.14c). The enclaves represent a snapshot of this process at the interface of interactions of the magmas (Fig. 2.10). Nevertheless, as no age data of volcanic products in the studied area fall in the 0.6-0.15 Ma interval, an open question is if the extrusion of the dacitic domes correspond to the final stages of an expiring magmatic system (i.e. waning stage), or to the beginning of a new pulse of the Altiplano-Puna Volcanic Complex (Fig. 2.14c). The presence of the enclaves in many of the youngest domes and eruption of coeval less-evolved magmas (e.g. La Poruña) with similar geochemical and isotopic compositions in the last 150 ka within the Altiplano-Puna Volcanic Complex province, suggests a new period of mafic recharge, enabling the triggering of scattered eruptions within this volcanic province.

Some considerations about the main heat source of the Cerro Pabellón are necessary. According to numerical studies of convective cooling intrusions (Garcia-Estrada et al., 2002), high temperatures (about 300 °C) in hydrothermal systems can only exist if the magmatic heat source is less than a few hundred thousand years old (around 0.4 Ma for typical size rhyolitic intrusions at 4 km depth). Because the emission of silicic volcanic products at the AAVC ended about 0.6 ± 0.1 Ma ago, the present-day high temperatures measured in the geothermal boreholes (i.e. > 250 °C; Aravena et al., 2016) cannot be related to the known magmatic activity of the composite stratovolcanoes-forming events. Therefore, these temperatures should be associated with the area’s youngest (80-130 ka) dacitic magmatic episode, which led to the

emplacement of the small Cerro Pabellón dome. Nevertheless, as extensively discussed above, the dacitic domes of the studied area seems to be left-overs of previous magmatic phases (i.e. about 1 Ma), thus it is unlikely to ascribe the main heat source driving the active geothermal area of Cerro Pabellón to the dome magma chamber. However, as no age data of nowadays studied volcanic products in the AAVC fall in the 0.6-0.15 Ma interval, a univocal explanation cannot be defined. What is worth to mention is that the presence, the areal extension, and the volume of the huge APMB in the upper crust is not negligible and cannot be ruled out as the main heat source of this and the other geothermal systems of the APVC.

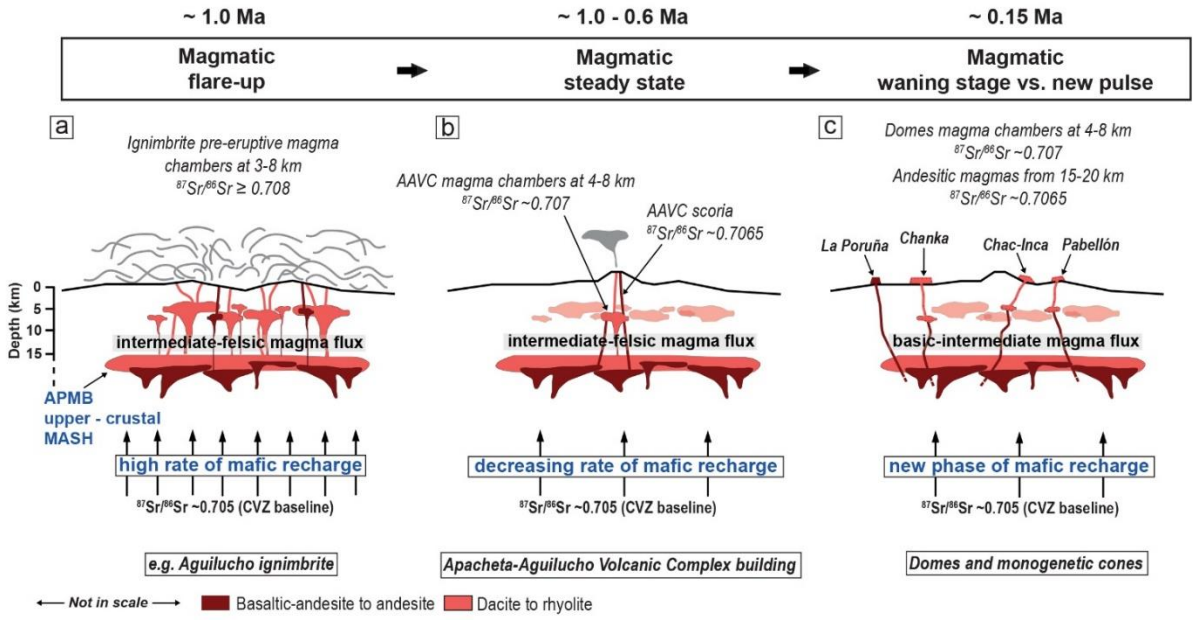

Figure 2.14 *– A schematic model of the magma plumbing system processes in the upper crust at the Altiplano-Puna Volcanic Complex, focussing on the Apacheta-Aguilucho area, through the last ~1.0 Ma. a) Flare-up stage with high rate of mafic recharge accumulates in the Altiplano-Puna Magma Body (APMB); this produced a high intermediate-felsic magma flux towards the pre-eruptive levels (3-8 km) where the magmas (with high crustal assimilation, i.e.* $^{87}Sr/^{86}Sr \geq 0.708$*; Burns et al., 2015) feed ignimbrite eruptions. At this time the Aguilucho ignimbrite was erupted. b) A decrease of mafic recharge is recorded at ~1.0-0.6 Ma, but the thermal conditions of the magmas involved still permitted the hybridization and mixing of the magmas forming the Apacheta-Aguilucho Volcanic Complex (AAVC; steady state conditions; sensu de Silva et al., 2015). c) A new phase (waning stage vs. new pulse) of mafic recharge is recorded at ~0.15 Ma; magmas ascended from depth into the upper crust with less mid-crustal interactions (*$^{87}Sr/^{86}Sr = 0.7065$*), where could: remobilize the dacitic magmas leftovers from previous magmatic stages, triggering the extrusion of the domes, or be erupted with slight contamination (e.g. La Poruña). The CVZ* $^{87}Sr/^{86}Sr$ *baseline is according to Davidson et al. (1991). Depths of the magma chambers according to Gorini et al. (2018). Depth of the Altiplano-Puna Magma Body as in Ward et al. (2014). Modified after de Silva et al. (2015) and arranged according to the present results of the Apacheta Aguilucho Volcanic Complex area. Figure from Taussi et al. (2019).*

CHAPTER 3

CLAY MINERALS ASSOCIATIONS FROM THE ACTIVE HYDROTHERMAL SYSTEM

THE PART OF THIS CHAPTER RELATED TO THE CLAY-CAP UNITS HAS BEEN PUBLISHED IN:

Maza, S.N., Collo, G., Morata, D., Lizana, C., Camus, E., **Taussi, M.**, Renzulli, A., Mattioli, M., Godoy, B., Alvear, B., Pizarro, M., Ramírez, C., Rivera, G., 2018. *Clay mineral associations in the clay cap from the Cerro Pabellón blind geothermal system, Andean Cordillera, Northern Chile*. Clay Minerals Journal of Fine Particle Science, 54 (2), pp. 117-141. https://doi.org/10.1180/clm.2018.9.

THE PART OF THIS CHAPTER RELATED TO THE FUMAROLIC FIELD ALTERATION WILL BE PREPARED FOR THE SUBMISSION WITH THE PROVISIONAL TITLE:

Dynamics of a fumarolic alteration in the Apacheta volcano associated with the Cerro Pabellón geothermal system, Northern Chile.

3.1. Introduction

Hydrothermal activity is a general term used to describe a complex set of interactions in which fluids, circulating within Earth's continental and oceanic crust, transfer heat energy and chemical mass toward the surface (Lowell et al., 2014). These processes produce mineralogical, textural and chemical variations of the host rocks, as a response to the changing thermal and chemical environment, by the presence of hot water, steam or gases (Henley and Ellis, 1983). Some chemical constituents may be removed from the fluid to the solid earth, while others may be extracted from the rock; these reactions are reflected in the transformation of primary to secondary rock-forming minerals. The formation of these hydrothermally altered minerals is usually dependent on the temperature, permeability, pressure, fluid composition, initial composition of the rock, the duration of the hydrothermal activity and the fluid:rock ratio. These factors are largely independent, but the effects of one or more of them can exert a dominant influence in the location and extent of hydrothermal alteration (Lagat, 2010). In volcanic environments, two main possible sources of hydrothermal fluids, or a combination of them, could be defined: i) near-surface groundwater (i.e. meteoric water); or ii) water and gases exsolving from the magma.

The two main types of alteration associated with volcanic geothermal systems are i) the acid-sulfate and ii) the adularia-sericite (Wohletz and Heiken, 1992). The acid-sulfate facies usually occurs within the uppermost parts of an active or dormant volcano, or along its ring fractures where there is abundant cool groundwater that could interact with the rising magmatic gases, producing acid-sulfate waters. By contrast, the adularia-sericite alteration type occurs within a flow regime, above or adjacent to a deep heat source, mostly linked to older volcanic plumbing systems, and is usually characterized by neutral pH and alkali-chloride waters (Heald et al., 1987). By mapping alteration mineral assemblages at the surface and/or along the drill-holes, it is possible to locate zones with high temperatures, as well the most impermeable and suitable subsurface rocks that can maintain steady conditions of temperature, pressure and enthalpy of the geothermal reservoir through time (Todesco and Giordano, 2010; Maffucci et al., 2016; Sánchez-Alfaro et al., 2016). This is of paramount importance in geothermal exploration and exploitation (Wohletz and Heiken, 1992). In fact, i) the cap-rock units, ii) the heat source, iii) the reservoir, and iv) the recharge areas, represents the four main elements in hydrothermal convective geothermal systems (Corrado et al., 2014). In volcanic and volcaniclastic systems, the development of large, thick cap-rocks is favoured by intense argillic alteration which leads to the formation of the clay-cap. The efficiency of these cover units is controlled to a significant extent by the intensity of the hydrothermal alteration. Di- and

trioctahedral clay minerals such as smectite, illite, corrensite, chlorite and chlorite-smectite, chlorite-corrensite and illite/smectite mixed layers are widespread hydrothermal alteration products in volcanic/subvolcanic geothermal systems (Inoue et al., 2004; Meunier 2005; Stimac et al., 2015). Geochemical and mineralogical processes leading to clay minerals and, in particular, transformation to mixed-layer phases (e.g. smectite to illite and smectite to chlorite) have been widely studied in many fossil and active hydrothermal systems (Inoue, 1995; Inoue et al., 2004; Meunier et al., 2008a,b; Vázquez et al., 2014; Inoue and Kogure 2016). Consequently, these studies are fundamental in understanding the spatial distribution of the clay minerals and their relationship with temperature. This can allow to estimate the efficiency of the clay-cap where other subsurface data are scarce, as in the case of blind geothermal systems, characterized by lack of surface thermal manifestations (e.g. Corrado et al., 2014).

In this chapter the hydrothermal mineralogical associations occurring at the Cerro Pabellón geothermal system (Fig. 3.1), both deeply and superficially, were investigated through X-Ray Diffraction (XRD) analyses. A total amount of 27 drill-cuttings samples from the 1,821.1 m deep production CP-1 well (21.8490°S, 68.1567°W, 4,546 m a.s.l.; Figs. 3.1b and 3.2) located in the Pampa Apacheta, and 16 clay-rich samples from the active fumarolic field of the Cerro Apacheta, were examined (Fig. 3.2). Moreover, XRD results from a 557 m long exploration drill core (PexAP-1; 21.8471°S, 68.1559°W, 4.545 m a.s.l.; Figs. 3.1b and 3.2) carried out by the C.E.G.A. (Centro de Excelencia en Geotermia de los Andes) group of the Universidad de Chile are also reported. The purpose of the present chapter is to examine the vertical and superficial distribution of the clay minerals forming the hydrothermal system of the Cerro Pabellón active geothermal field, in order to identify the minerals associations, define the clay-cap units and characterize the hydrothermal alteration type. The first preliminary results from the fumarolic deposits of the Cerro Apacheta fumarolic field are here presented and discussed. Anyway, further work and analyses need to be done on these samples, to define the minerogenesis, and the physico-chemical processes that affected the fluid-rocks interactions.

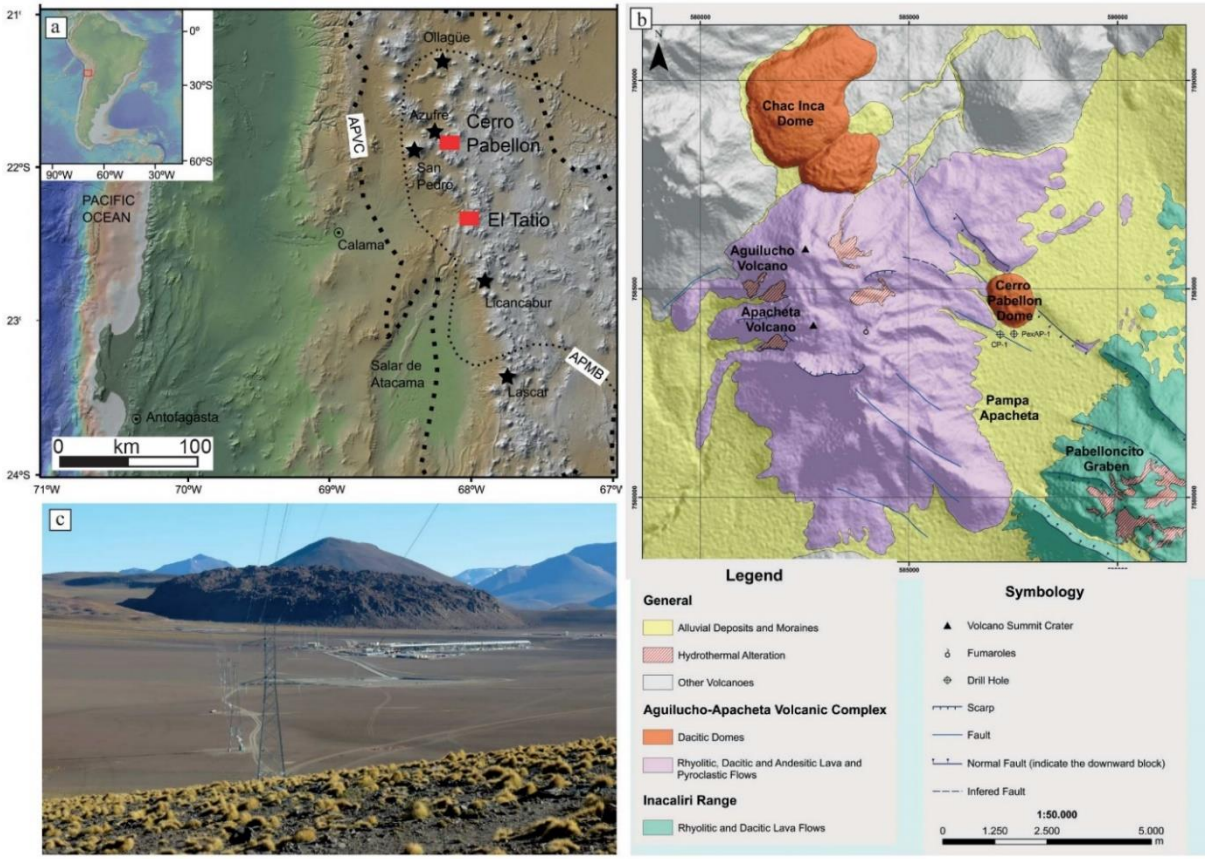

Figure 3.1 *- a) Central Volcanic Zone (CVZ) in the Andean Cordillera showing the Altiplano-Puna Volcanic Complex (APVC; de Silva, 1989), the main Pleistocene to Holocene volcanoes and the location of the Cerro Pabellón geothermal system; b) simplified geological map of the Cerro Pabellón geothermal field (modified from Godoy et al., 2017b); c) general view of the Cerro Pabellón geothermal power plant with the 80-130 ka Cerro Pabellón dacitic dome in the background. Figure from Maza et al. (2018).*

3.2. Geological setting

The Central Volcanic Zone (CVZ) is an active volcanic region with heat-flow values between 50 and 180 mW/m^2 measured in the active magmatic arc and in the Altiplano (Springer and Forster, 1998). This region comprises abundant Quaternary volcanoes and its geodynamic setting is favourable to the development of several geothermal areas (Aravena et al., 2016). The CVZ has been developing under a complex tectonic regimes since the Early Cretaceous, and is associated with the subduction of the Nazca Plate under the South American Plate, which gives rise to magmatic and hydrothermal activity (e.g. Lahsen, 1988; Brasse et al., 2002; Farías et al., 2005; Charrier et al., 2007; Tassi et al., 2010; Sánchez-Alfaro et al., 2015; Herrera et al., 2017). In northern Chile, the magmatism generated Middle Cretaceous–Late Miocene andesitic to rhyolitic volcanic rocks overlain by Late Miocene-Pleistocene ignimbrite deposits (Lahsen and Trujillo, 1975; Francis and Rundle, 1976; Marinovic and Lahsen, 1984; de Silva, 1989; Ahumada and Mercado, 2009). These volcanic rocks constitute the Altiplano-Puna Volcanic Complex (APVC), a volcano-tectonic silicic

magmatic province generated by the partial melting and interaction of the thickest continental crust in the world (de Silva, 1989; Beck et al., 1996) with mantle-derived basaltic andesite magmas. Over these units, different Pleistocene to Holocene arc volcanoes have been emplaced. In the studied area, the CVZ is characterized by several NW-SE oriented eruptive centers dominated by the polygenetic Palpana-Inacaliri volcanic chain of Pliocene-Pleistocene age (Wörner et al., 2000; Sellés and Gardeweg, 2017), where stratovolcanoes of basaltic-andesite to dacitic composition, such as the Apacheta-Aguilucho Volcanic Complex (AAVC) and dacitic domes of Pabellón and Chac-Inca are recognized (Fig. 3.1b). Locally, the different geological units have been identified by surface geological mapping and recorded from four commercial wells drilled by Geotermia del Norte S.A. (GDN) (Rivera et al., 2015). They mainly correspond to Pliocene-Pleistocene andesitic to dacitic lava, breccias and tuffs, capped by a 100 m-thick welded ash flow, whereas the recent volcanic activity is associated with the Pleistocene dacitic lava domes of Pabellón (80.0-130.0 ka, Ar-Ar; Renzulli et al., 2006; 50.0 ± 10.0 ka, K-Ar; Urzua et al., 2002) and Chac-Inca (114.0 ± 37.0 ka, Ar-Ar; Rivera et al., 2015) (Fig. 3.1b). A local Pliocene extensional phase, within a regional compressional regime related to the subduction of the Nazca Plate under the South American Plate, took place in the area (e.g. González et al., 2003; Tibaldi et al., 2009). This phase generated a NW-striking normal fault system which extends from Azufre volcano in the NW to Inacaliri volcano to the SE (Tibaldi et al., 2017).

In the investigated zone, a topographically depressed area of ~100 km^2 (Tibaldi et al., 2009; Rivera et al., 2015), ~20 km long and ~4 km wide, is well defined by two major lineaments with converging dips and pronounced scarps (~100-150 m), which form a symmetric graben. This NW-SE Pabellóncito graben structure, affects the NW-SE aligned Pliocene stratovolcanoes. In fact, the structural weakening of the AAVC by the local extensional setting and hydrothermal alteration is confirmed by the presence on the eastern flank of a debris avalanche deposit, morphologically emphasized by small hummocks, levées and ridges, and mainly consisting of fragments of andesitic-to-dacitic lavas and hydrothermally altered lava blocks (Godoy et al., 2017b). This deposit has recently been interpreted to be triggered by the partial collapse of this volcanic edifice 100-700 ka ago (Godoy et al., 2017b). Conversely, the main NE fault bounding the graben was sealed by the Pabellón dome (Fig. 3.1c), whose extrusion was favored by the structural weakness related to the normal faults of the graben (Tibaldi et al., 2009). On the surface, the Cerro Pabellón active geothermal system only exhibits two superheated fumaroles, a mud pool, and some minor vents, located in a 0.3 km^2 area on the summit of the Cerro Apacheta volcano (5,150 m a.s.l.) at about 3 km western from the Pabellón dome. This fumarolic field is imposed on intercalation of grey andesitic lavas and highly vesiculated, scoria-rich pyroclastic flows (Piscaglia, 2012; see also Chapter 2). Wide areas of hydrothermal alteration also outcrop on the north, west, southwest and eastern

flanks of the volcano edifice and are partially related to past and present fumarolic activity (Aguilera et al., 2008). The gas geochemistry of the two superheated fumaroles suggests their relationship with a high-temperature geothermal system, with a reservoir consisting of biphasic fluids (liquid and vapor, in proportions of 80% and 20%, respectively; ENEL personal communication), at temperatures of 250-325°C (Urzua et al., 2002; Tassi et al., 2010). Nevertheless, the only surface alteration related to the active Cerro Pabellón geothermal system is the presence of discontinuous altered clay zones, spatially related to an acid-sulfate alteration, including native sulfur and clay minerals affecting the Pliocene volcanic units (Fig. 3.1b; Ramírez and Huete, 1981; Urzua et al., 2002; Tibaldi et al., 2009).

3.3. Sampling and analytical methods

The fumarolic field, the CP-1 production well and the PexAP-1 locations are reported in Figure 3.2. Representative fumarolic field samples from the Apacheta Volcano (21.8457°S; 68.1853°W; 5,179 m a.s.l), which is part of the AAVC, were collected during two field trips, in November 2016 and November 2017. Samples location is shown in Figure 3.2b, while the coordinates and the related measured temperatures, are reported in Table 3.1. The fumarolic field has an extension of about 0.03 km^2, and it is characterized by various types of hydrothermally-altered volcanic rocks, showing whiteish to yellow to reddish to purplish colorations (Fig. 3.3).

The samples studied from the drilling cuttings of the CP-1 well were collected every 25 meters, from 175 m to 825 m of depth, for a total amount of 27 samples. The shallower 10 cutting-samples, preliminary studied in Piscaglia (2012), were re-elaborated as well. The samples studied along the PexAP-1 well correspond to depths between 165 and 557 m, with a spacing of ~30 m, for a total amount of 25 samples.

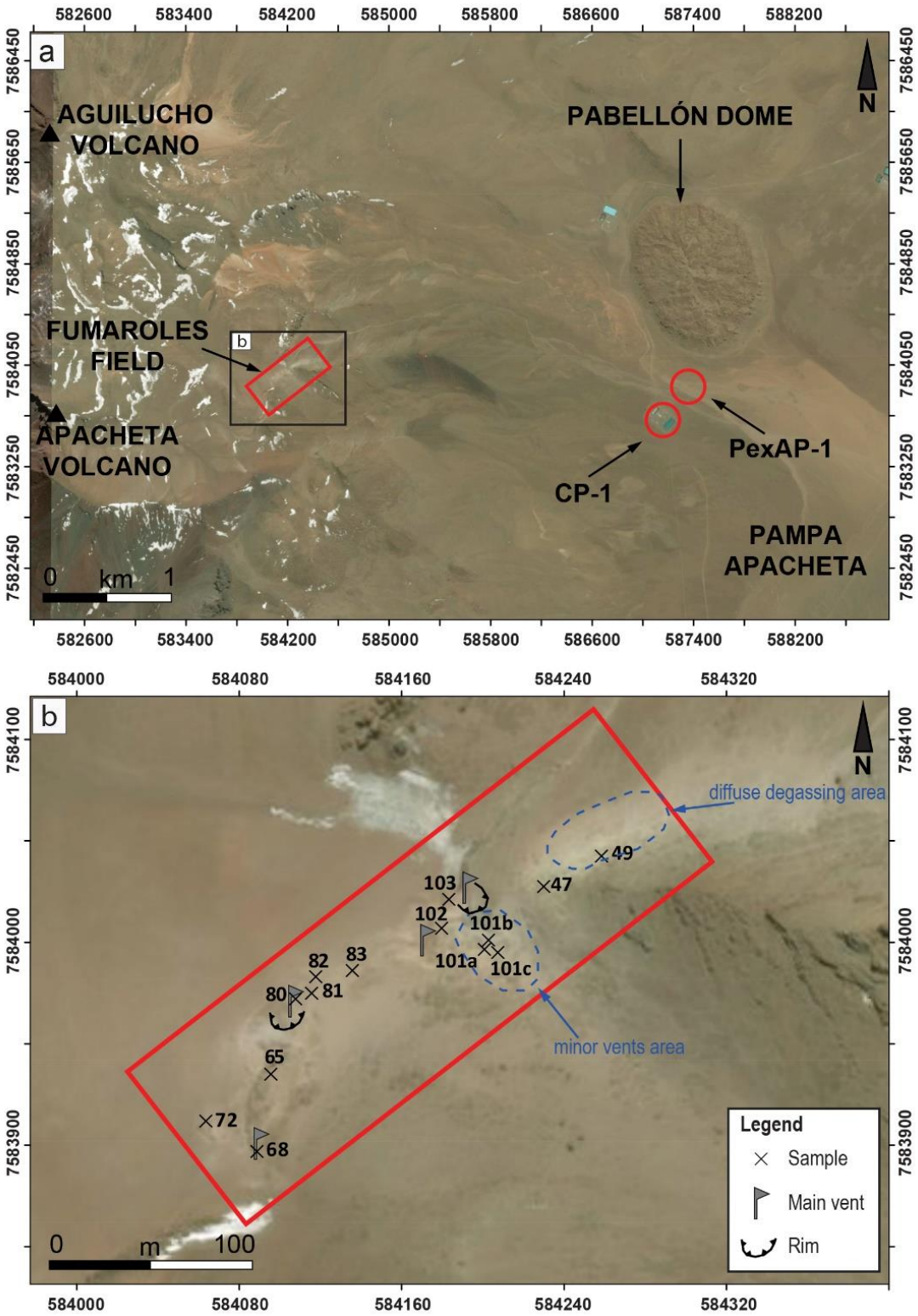

Figure 3.2 *– a) Global view of the Apacheta-Aguilucho Volcanic Complex with the location of the fumarolic field, of the CP-1 production well platform, and of the PexAP-1 exploratory well; b) detailed map of the fumarolic field with the location of the samples, and of the main thermal features. Coordinates in WGS84 UTM19S, modified from Google Earth™.*

Table 3.1.
Representative samples from the fumarolic field

ID SAMPLE	EAST	NORTH	HEIGHT (m a.s.l.)
FA47	584233	7584018	5,159
FA49	584265	7584034	5,166
FA65	584096	7583935	5,181
FA68	584089	7583897	5,190
FA72	584064	7583912	5,190
FA80	584108	7583972	5,172
FA81	584116	7583975	5,171
FA82	584118	7583983	5,170
FA83	584136	7583986	5,165
FA101a	584206	7583995	5,150
FA101b	584204	7583994	5,151
FA101c	584209	7583991	5,151
FA102	584178	7584004	5,156
FA103a	584184	7584015	5,152
FA103b	584184	7584015	5,152
FA103c	584184	7584015	5,152

The XRD data were obtained with a Bruker D8 Advance diffractometer with Cu-Kα radiation and a Bragg-Brentano geometry at the Department of Physics in the Facultad de Ciencias Físicas y Matemáticas of the Universidad de Chile (Chile) and a Philips PW1830 diffractometer with PW3710 generator and Cu-cathode at 30 mA and 40 kV at the Università degli Studi di Urbino Carlo Bo (Italy). Samples for bulk-rock analysis were dried at room temperature and powdered in an agate mortar, and successively mounted in aluminum holders for the bulk composition analysis, and glass holders for clay minerals analyses.

The minerals in the clay fraction (<2 μm) were identified according to the position of the basal reflections of air-dried (AD), ethylene-glycol solvated (EG), and heated to 355°C (355) and 550°C (550) XRD patterns, using the criteria of Moore and Reynolds (1997). Smectite was identified by the peak shift from ~14 Å to ~17.5 Å after EG solvation, and collapse to 10 Å after the heat treatments (Moore and Reynolds, 1997).

The presence in the boreholes of illite-smectite (I-S) mixed layers and their illite proportions were determined by the reflection near 16-17°2θ and the ordering types (R0, R1 and R3) by the position of the reflection from 5 to 8.5°2θ in the AD and EG preparations. Illite was identified by the 10.1 Å, 5.0 Å and 3.33 Å reflections on AD preparations, which are not displaced after the EG and 355 and 550 treatments. Chlorite was identified by the 14, 7, 4.76 and 3.53 Å reflections in AD and EG samples. Kaolinite was identified by the ~7 Å peak in the AD, EG and 355 analyses, followed by the disappearance in the 550 X-ray diffractogram. Mixed-layer chlorite-smectite (C-S), corrensite and chlorite-corrensite (C-Cor) were identified following the recommendations of Beaufort et al. (1997), and Moore and Reynolds (1997). The CP-1 cuttings between 175 m and 400 m of depth were analysed by Piscaglia (2012), over a 2θ angle of 2-75°, steps of 0.02° and a scan-step of 1 sec for bulk composition, a 2θ angle of 2-50°, steps of 0.02° and a scan-step of 1 sec for AD and a 2θ angle of 2-30°, steps of 0.02°

and a scan-step of 1 sec for EG. No thermal treatments were carried out on these samples. The cuttings between 425 m and 825 m of depth were analysed over a 2θ angle of 5-70°, steps of 0.02° and a scan-step of 1 sec for the bulk composition, while a 2θ angle of 2-40° in steps of 0.02° and a scan-step of 1 sec for AD, and a 2θ angle of 2-30° in steps of 0.02° and a scan-step of 1 sec for EG, 355 and 550 compositions. PexAP-1 samples were analysed over a 2θ angle of 5-70°, steps of 0.02° and a scan-step of 1 sec for the bulk composition, while clay mineral analyses were carried out between 2 and 40°2θ, with a step size of 0.02°2θ and a scanning time per step of 47.25 s for each treatment. The fumarolic field samples were measured over a 2θ angle of 2-65° in steps of 0.02° and a scan-step of 1 sec for bulk composition, a 2θ angle of 2-40° in steps of 0.02° and a scan-step of 1 sec for AD, and a 2θ angle of 2-30° in steps of 0.02° and a scan-step of 1 sec for EG, 355 and 550 compositions. All the data were collected by the software X'Pert Quantify and then elaborated by the software X'Pert High Score.

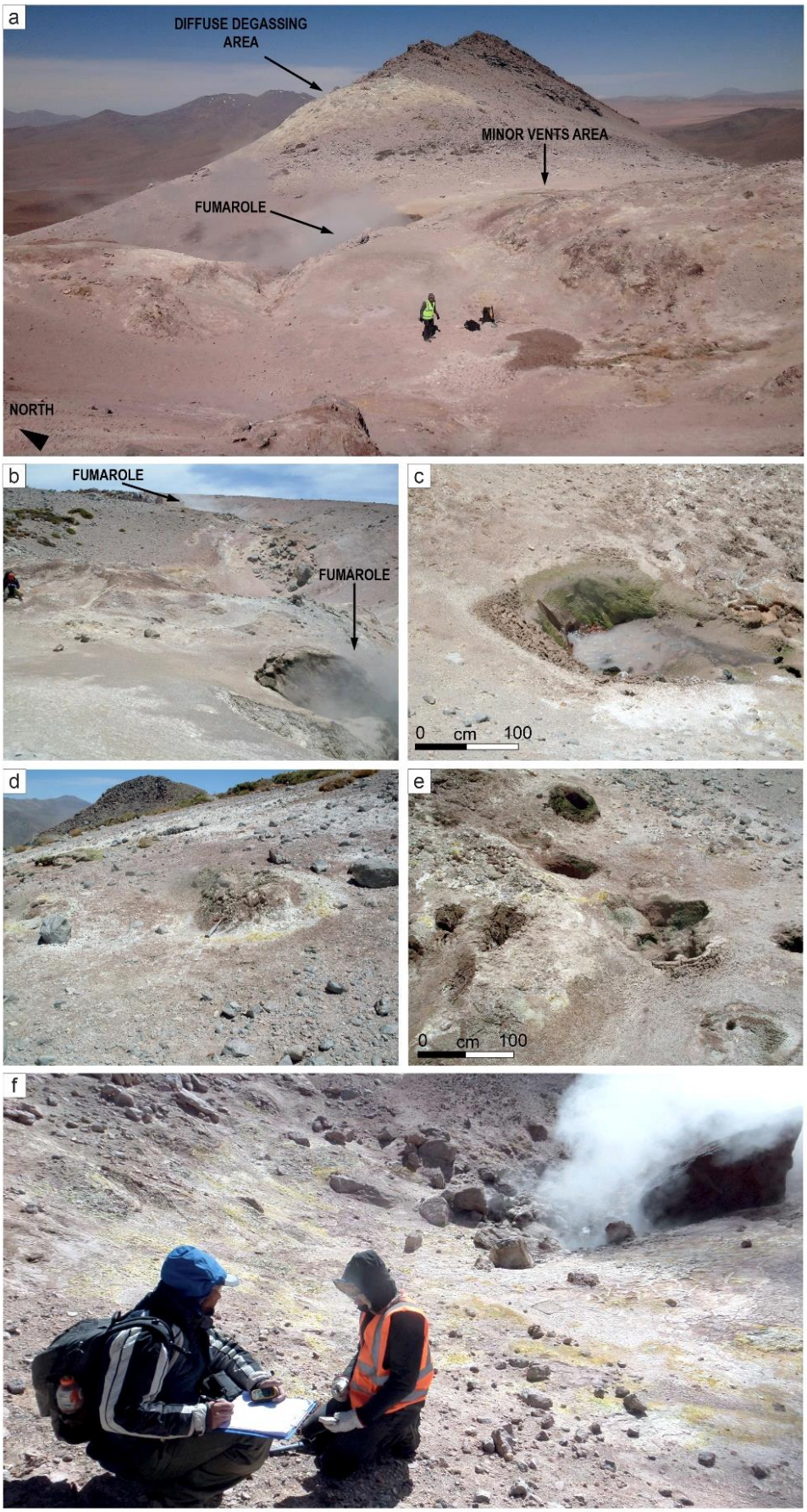
a
DIFFUSE DEGASSING AREA
MINOR VENTS AREA
FUMAROLE
NORTH
b
FUMAROLE
FUMAROLE
c
0 cm 100
d
e
0 cm 100
f

Figure 3.3 *– Field photographs. a) General view of the Apacheta fumarolic field from North-West, with indicated the main thermal features; b) view of the two super-heated fumaroles; c) mud pool; d-e) minor vents with different distinguishable different colorations varying from whiteish to yellowish to reddish; f) sampling procedure near the fumarole, where whiteish-yellowish colorations and crusts are visible.*

3.4. Results

3.4.1 Subsoil hydrothermal system

The stratigraphic sequence of both wells is summarized in figure 3.4. The different lithologies recorded from PexAP-1 and CP1 wells are comparable (Rivera et al., 2015): the first ~190 m consists of unconsolidated sediments (0-65 m), recent volcanic rocks (65-125 m) and whitish tuffs (125-190 m); from ~190 to 737 m the sequence is characterized by an alternation of breccias and andesitic lavas; from ~737 to 900 m red-whitish tuffs were recognized. Finally, from 900 to 1755 m a series of andesitic-dacitic lavas with intercalations of tuffs were distinguished. Secondary alteration minerals were studied in the continuous drill core PexAP-1 well and in the cuttings from the CP1 well (Fig. 3.4).

Similar mineral assemblages were recognized from XRD analyses along both wells (Fig. 3.4). Smectite is the main clay mineral in the ~165-250 m interval which is also characterized by the absence of quartz and the presence of clinoptilolite, calcite, alunite, pyrite and hematite. From ~250 to ~500 m, mixed-layer I-S and C-S linked to albite, calcite, hematite, quartz, stilbite and laumontite were identified. At about 375 m starts to appear corrensite, which is found in different samples until 575 meters. From ~400 m smectite group minerals rapidly decrease, while chlorite is intimately associated with hematite, adularia, albite, calcite, quartz, epidote, while illite was identified from ~500 m. The Ca-zeolites (clinoptilolite-stilbite-laumontite-wairakite sequence) are present from 165 m in a relatively discontinuous way. From ~500 m, it is possible to recognize epidote, sporadically at first and then in a persistent way from 625 m.

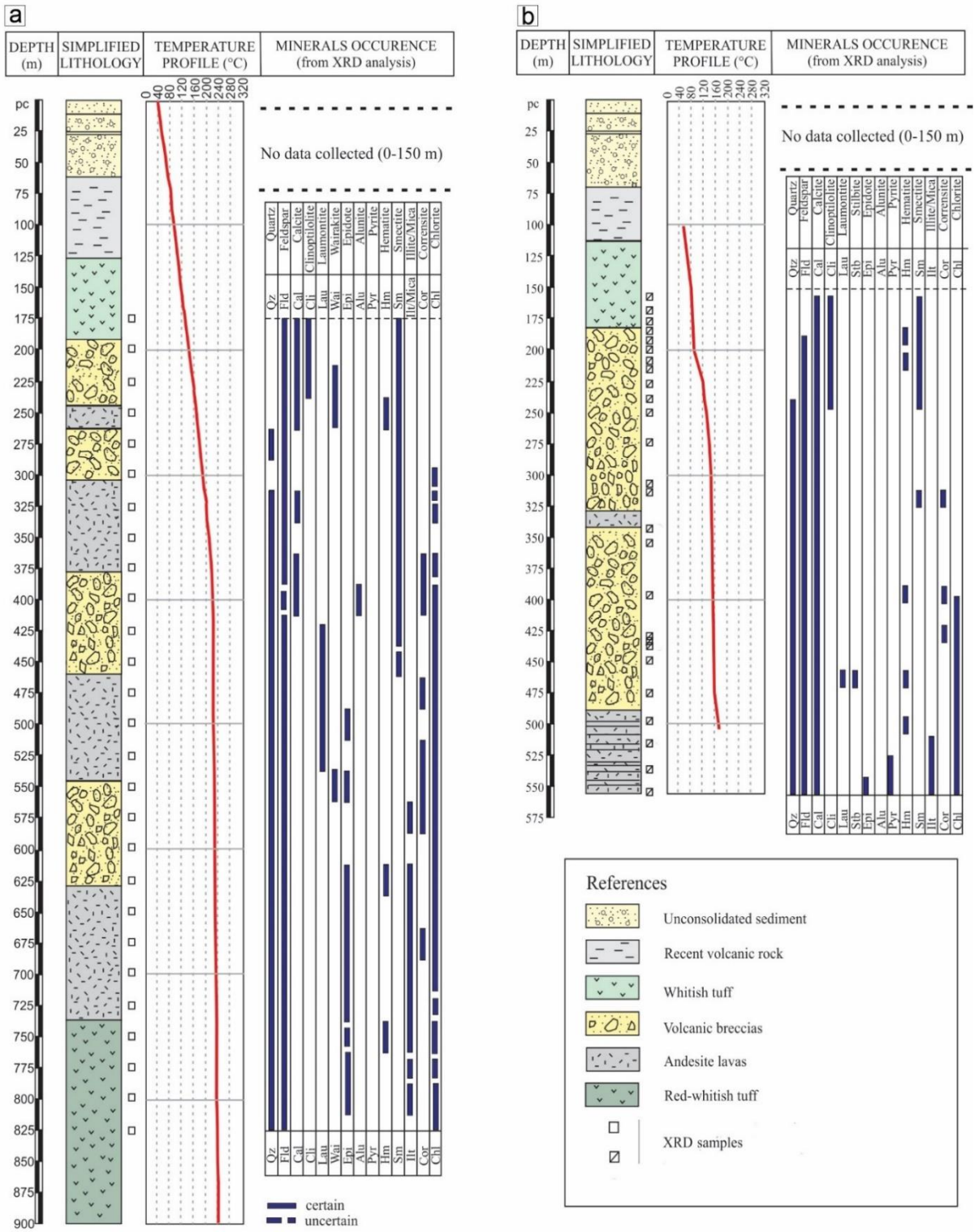

Figure 3.4 *- Simplified lithological columns of the Cerro Pabellón geothermal field obtained from the CP-1 (left) and the PexAP-1 (right) wells, showing measured temperature profiles (°C) and the main alteration minerals identified through petrography and bulk-rock XRD. Figure from Maza et al. (2018).*

A detailed analysis of the clay minerals was carried out in the PexAP-1 well. Smectite, I-S, illite, C-S, corrensite, C-Cor and chlorite were identified, showing a zonation with depth (Fig. 3.5, Table 3.2 from Maza et al., 2018). Smectite is present continuously from the shallower parts of the borehole down to a depth of 251 m and reappears at a depth of 319 m (Table 3.2, Figs. 3.4 and 3.5a). At greater depths, smectite disappears and is replaced by mixed-layer I-S: R0-type I-S with ~10% illite layers at 346 m depth, R1-type I-S with 55-66% illite layers at ~433 m and R3-type I-S with >90% illite layers occurring continuously from depths of ~451 to ~493 m. Then, to the bottom of the well, R3 I-S (>90% illite) was identified. Samples CP273 and CP401 contain R3-type I-S with illite contents which are not in agreement with those from the nearby samples. Mixed-layer C-S appears together with smectite in shallower levels between 213 and 346 m (Fig. 3.5a). Corrensite is also present discontinuously with R1 and R3-type I-S between 273 (Fig. 3.5b) and 434 m depth, whereas from 400 m to the bottom of the well, mixed-layer C-Cor coexists with chlorite and illite (Fig. 3.5c).

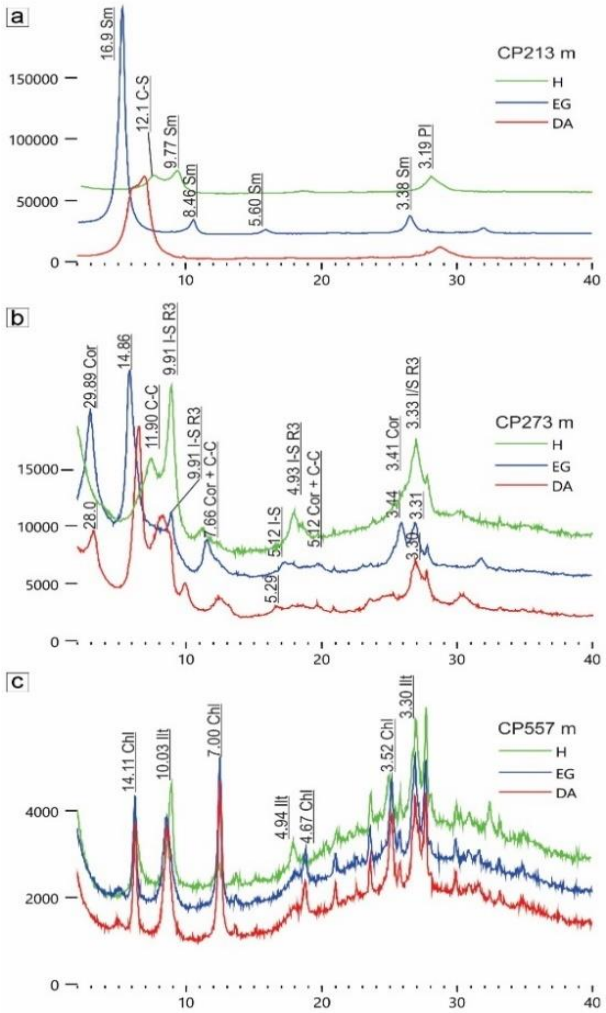

Figure 3.5 *- XRD patterns in the <2 µm fraction of representative samples in the PexAP-1 well. Red: air dried; blue: after ethylene glycol solvation; green: heated at 500°C. Numbers indicate d-spacing in (Å). Figure from Maza et al. (2018).*

Table 3.2.
Clay mineralogy of the PexAP-1 well. Sm: smectite; I-S: illite-smectite; Ilt: illite; C-S: chlorite-smectite; Cor: corrensite; C-Cor: chlorite-corrensite; Chl: chlorite. % of illite in I-S and *in situ* measured temperature are also shown.

Sample	Clay minerals									
	T ºC	Sm	(R0) I-S	(R1) I-S	(R3) I-S	Illt	C-S	Cor	C-C	Chl
CP165	95	x								
CP170	97	x								
CP173	100	x								
CP181	103	x								
CP184	106	x								
CP197	110	x								
CP212	117	x								
CP213	124	x					x			
CP228	141	x					x			
CP240	148	x					x			
CP251	154	x					x			
CP273	172				88			x	x	
CP317	173	x					x			
CP319	173	x					x			
CP346	176		10				x			
CP401	180				85			x	x	x
CP432	183			56					x	x
CP433	183			64				x	x	x
CP434	183			66				x	x	x
CP451	184				80				x	x
CP467	185				90				x	x
CP494	190				90				x	x
CP512	208					x			x	x
CP534	222					x			x	x
CP557	238					x			x	x

3.4.2 Clay-rich fumarolic field samples

The semiquantitative mineralogical compositions of the fumarolic field samples, and the relative soil temperatures are reported in Table 3.3, representative XRD patterns are presented in Figure 3.6. From the comparison of the mineralogical assemblages three groups and three samples with distinct modal mineralogy were distinguished (Table 3.2).

Table 3.3.
Semi-quantitative mineralogical compositions of analyzed samples and related soil temperatures

Samples	**Kao**	**Sm**	**Ver**	**I/M**	**mixed**	**Hal**	**Feld**	**Op**	**Cr**	**Qz**	**Cpx**	**AlOx**	**Al**	**Temperature at 10 cm (°C)**
GROUP 1														
FA47	++	+				+++	+				+			71.8
FA65	++	++				++	+				+			46.7
FA72	+++	+				+				+				30.1
FA103a	++	+++				+								47.5
FA103b	+	+++				+			+					47.5
GROUP 2														
FA68		+++					++		+					83.0
FA80		++		+			++		++					41.8
FA82		+++		+		+	+							34.3
FA101a		+++					+		+	+				66.5
FA102		+++		+			+		+					56.2
GROUP 3														
FA101b		++											+++	68.4
FA101c	+	++				+	+		+				++	81.3
FA103c		+++		+			+						+	47.5
DISTINCT SAMPLES														
FA49		+			+		+	+++	++					82.8
FA81		+++	++											65.1
FA83		+		+			+			++		+++		80.7

Legend*: Kao = kaolinite; Sm = smectite; Ver = vermiculite; I/M = illite/mica; Inter = mixed layer clay minerals; Hal = halloysite; Feld = feldspar; Op = opal; Cr = cristobalite; Qz = quartz; Cpx = clinopyroxene; AlOx = aluminum hydroxides; Al = alunogen.*
Amount*: + = less abundant; ++ = abundant; +++ = very abundant.*

Samples of group 1 (Table 3.3; Fig. 3.6a) are characterized by the presence of kaolinite (up to very abundant) and smectite (from low to abundant) group minerals, and halloysite (from less to very abundant). Specifically, the smectite group minerals are montmorillonite and nontronite, whereas the kaolinite group minerals are represented by kaolinite, nacrite and dickite. These minerals are associated with variable amounts but always subordinated, of clinopyroxene, feldspar, cristobalite and quartz. Samples of group 2 (Table 3.3; Fig. 3.6b) are characterized by the dominance of the smectite group minerals (from abundant to very abundant) and feldspar (from less to abundant). The smectite group minerals are represented by montmorillonite, nontronite and volkonskoite. Fewer amounts of cristobalite, halloysite, illite/mica and quartz are also present. No kaolinite was found in these samples. Samples of group 3 (Table 3.3) are characterized by the presence of alunogen, coupled with abundant smectite, probably represented by nontronite and montmorillonite. Subordinate feldspar, kaolinite, halloysite, cristobalite and mica (muscovite) are also found in small amounts.

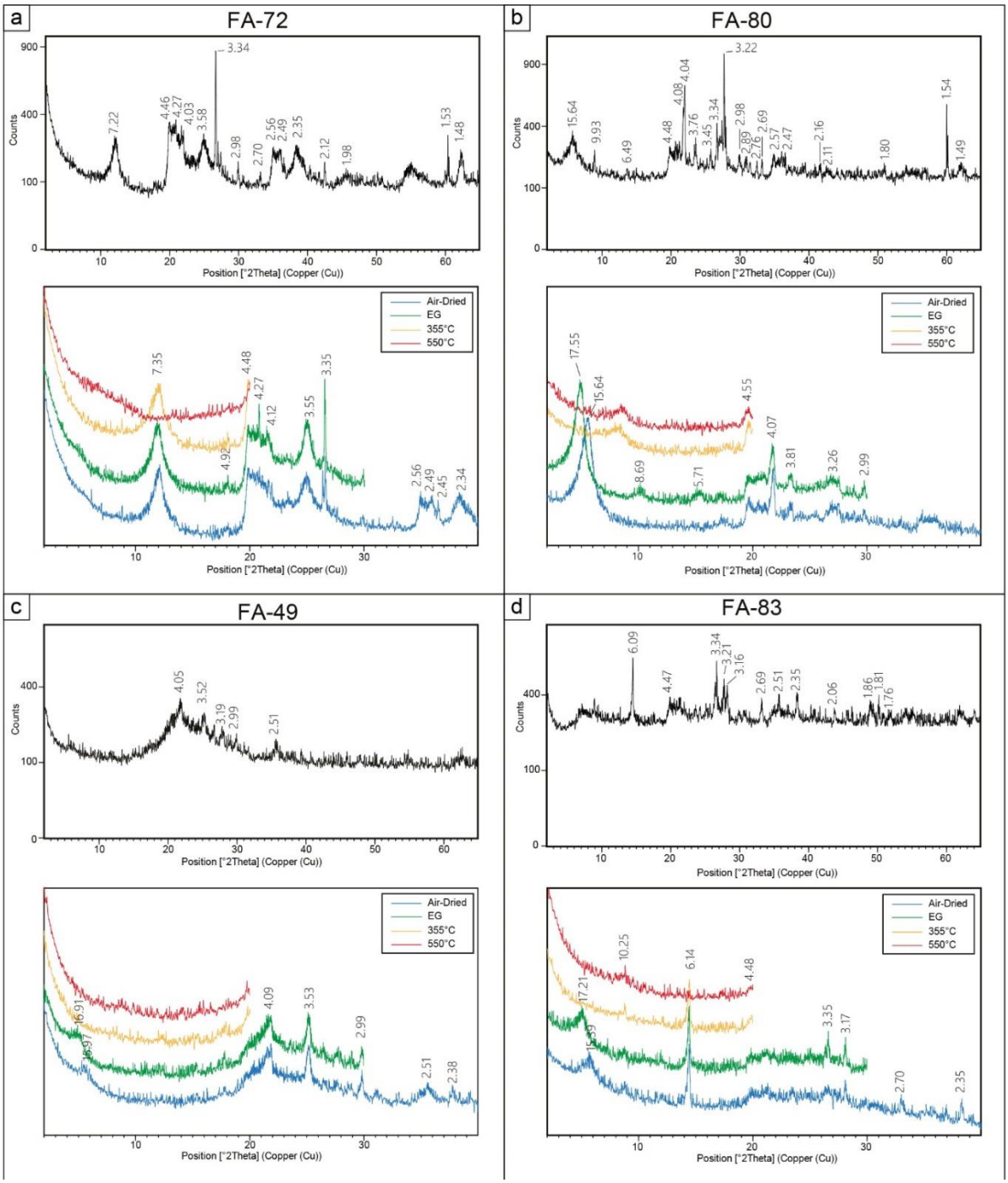

Figure 3.6 *- XRD patterns of representative samples of the fumarolic field. Black: bulk composition; blue: air dried; green: after ethylene glycol solvation; yellow: heated at 355°C; red: heated at 550°C. Numbers indicate d-spacing in (Å).*

Finally, samples FA49, FA81 and FA83 show, each one, peculiar mineralogical compositions (Table 3.3). FA49 (Fig. 3.6c) is the only one, among the analysed samples, dominated by the presence of silica phases, both as amorphous (opal, very abundant) and crystalline phase of high-T (cristobalite, abundant), associated to less amount of smectite group minerals, high-T feldspar and mixed layer minerals. Sample FA81 is characterized by a

simple composition, pointed out by the presence of abundant vermiculite, related to the high amount of smectite group minerals, such as montmorillonite, nontronite and volkonskoite. Sample FA83 (Fig. 3.6d) is distinguishable by abundant Al-hydroxides [AlO(OH)] and quartz, coupled with the minor amount of the smectite group minerals (beidellite), feldspar (plagioclase) and illite/mica.

3.5. Discussion

3.5.1 Clay mineral associations in the boreholes and related temperatures of formation

The present study differentiates several mineral assemblages down the borehole that can be grouped into three main hydrothermal alteration zones: (i) argillic zone; (ii) sub-propylitic zone; and (iii) propylitic zone. The argillic zone mainly affects the shallow part of the system, from 165 m to 315 m in the PexAP-1 well and from 175 m to 350 m in the CP-1 well. In this interval, an intensive, pervasive alteration dominated by smectite is observed, associated with hematite, zeolites, calcite, alunite and quartz. The smectites are mainly represented by montmorillonite, typical of smectites associated with the early alteration products of volcanic glass (e.g. Bauluz et al., 2002; Guisseau et al., 2007). Discrete smectite disappears completely at depths below 345 m, being replaced by I-S. Although kaolinite group minerals were found in none of the investigated samples, the presence of alunite could referrers this shallower part of the system to an advanced argillic alteration facies (Fulignati et al., 1998).

The sub-propylitic zone operates over the depth interval 315-490 m in the PexAP-1 well and over 360-420 m depth in the CP-1 well. This zone is dominated by mixed-layer I-S with R0, R1 and R3 ordering, C-S, corrensite, C-Cor and chlorite, plagioclase, quartz, calcite, hematite, stilbite and laumontite. The amount of I-S and C-Cor decrease with increasing depth and temperature (Table 3.2), with random ordered R0 I-S type identified at 345 m depth, and regularly ordered R1 I-S type at 432-434 m depth. Some exceptions to this trend were observed, as illite-rich R3 I-S appears at ~270 and ~400 m depth (Table 3.2).

From a depth of ~450 m until the propylitic zone (~510 m) mixed-layer I-S with R3 ordering dominates. Finally, the propylitic zone, from depths of 490 to 557 m in the PexAP-1 well and from 420 to 825 m in the CP-1 well, is characterized by illite and chlorite as the main phyllosilicates, associated with mixed-layer C-Cor, epidote, plagioclase, adularia, quartz, calcite, pyrite, chalcopyrite and titanite. The argillic and sub-propylitic zones, dominated mostly by clay minerals, represent a thick clay-cap (~300 m thick), while the propylitic zone should represents the beginning of the reservoir domain of the Cerro Pabellón geothermal system.

The transition of smectite to illite, via mixed-layer has been reported widely in hydrothermal systems, as the transition between the two end-member clays involved changes in chemical composition that might be related to temperature. In geothermal systems, the ranges of

temperature recorded for the appearance of smectite, illite/smectite and illite are ~75-220°C, ~130-220°C and ~130-300+°C (Wohletz and Heiken, 1992; Day-Stirrat et al., 2010; Vázquez et al., 2014). At Cerro Pabellón, the clay-cap consists of the argillic and sub-propylitic zones, characterized by low permeability and temperatures lower than ~190°C. This is also in accordance to Piscaglia (2012), that determined the clay-cap units with field methods (i.e. methylene blue, using the methodology described in AFNOR 1993) and with the semi-quantitative analyses of the clay minerals abundance (Biscaye, 1965), although reporting a minor thickness of these units (i.e. ~50-75 m). The argillic zone is characterized by the occurrence of clinoptilolite and smectite as index minerals and temperatures between 90 and 175°C (from depths of 175 to 315 m; Fig. 3.7). The transition from the argillic to the sub-propylitic zones, with the replacement of smectite for R1 I-S, and the appearance of chlorite and laumontite takes place at 180-185°C. The sub-propylitic zone (315 and 490 m depth; Fig. 3.7), characterized by (R1-R3) I-S, is related to borehole temperatures between 175 and 190°C. Finally, the propylitic zone, with the chlorite-epidote-illite association (from about 500 m downwards), records temperatures >200°C (Fig. 3.7). In the PexAP-1 well two levels at 273 and 400 m containing R3 I-S are outside the observed illitization trend. Sample CP273 belongs to the argillic zone, dominated by smectites, whereas sample CP400 corresponds to the sub-propylitic zone in the transition from R0 to R1 I-S (Fig. 3.7). There is no relationship between the lithological variations in the well and the appearance of R3 I-S at these levels. The occurrence of R3 I-S in these levels, >100 m apart on the vertical scale, might be explained by local fluctuations in fluid:rock ratios, mentioned above as a significant variable in the formation of clay minerals. The andesitic levels at which the specific R3 I-S occurs are interlayered in an area dominated by polymictic breccias (Fig. 3.4), possibly leading to zones of greater permeability in the system, associated with hydrostatic fracturing. The presence of minerals such as adularia, chlorite, epidote and illite represent some of the most typical phases occurring in an adularia-sericite alteration type, usually formed in geothermal systems where surficial waters mix with deeper, heated saline waters in a lateral flow regime, high above and probably offset from a heat source at depth (Heald et al., 1987).

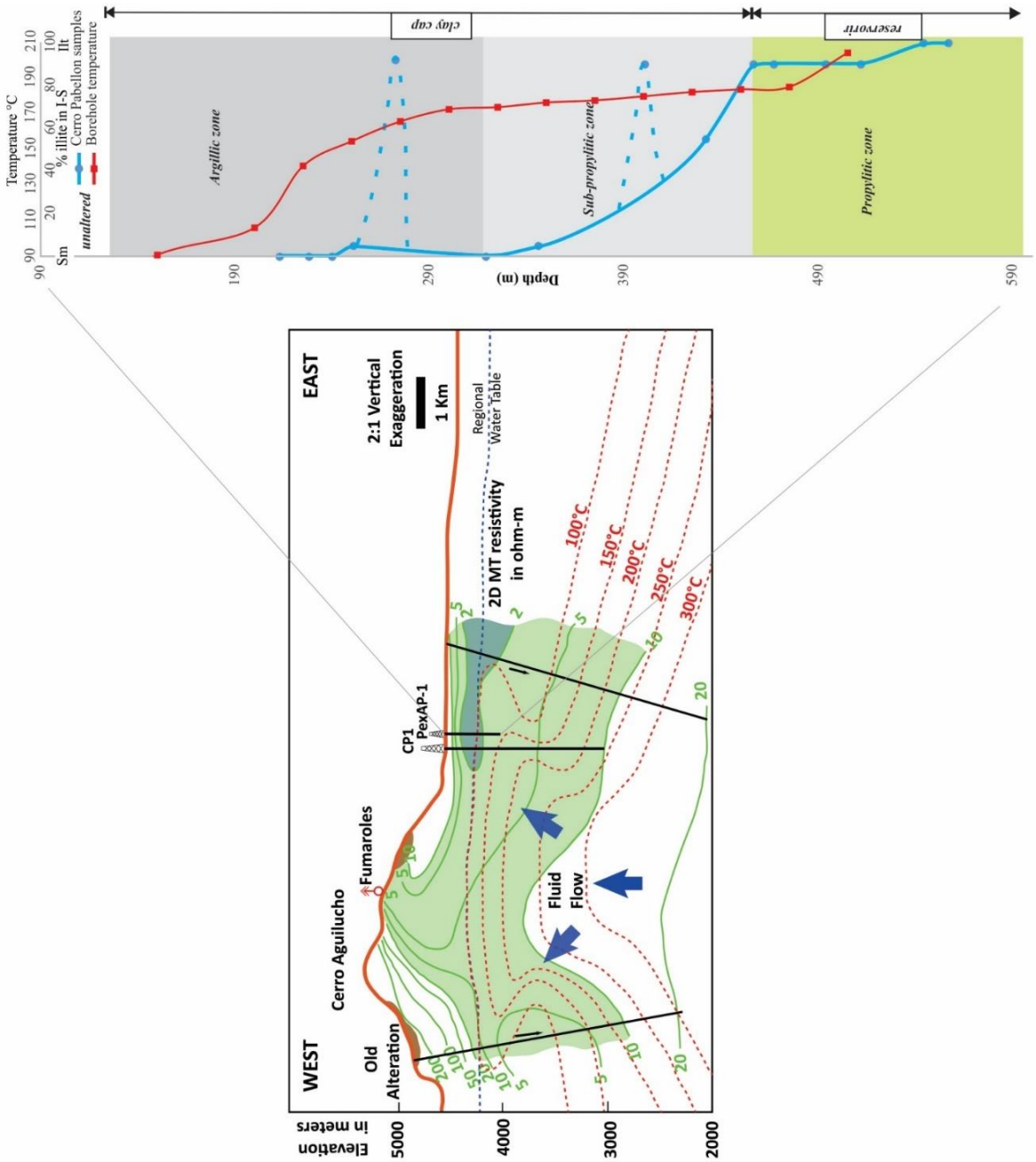

Figure 3.7 *- Simplified conceptual model for the Cerro Pabellón geothermal system: a) west to east simplified profile of the Cerro Pabellón area showing temperature isotherms and MT (magnetotelluric) resistivity data from Urzua et al. (2002). Following these authors, the <10 Ω·m low resistivity layer was interpreted as a smectite clay cap overlying rocks at temperatures of >200°C as expected over geothermal reservoirs; the lowest (<2 Ω·m) resistivities detected in very shallow smectite clay zones were associated with parched fossil aquifers. b) Clay-mineral evolution along the clay-cap showing the variation in I-S content (blue line) and temperature (red line) along the profile (data referred to the PexAP-1). Figure from Maza et al. (2018).*

3.5.2 Superficial hydrothermal alteration

The different types of mineralogical associations recognized in the AAVC fumarolic area are referable to an intermediate argillic alteration facies (*sensu* Fulignati et al., 1998),

controlled by the presence of clay minerals, which is a common feature of all the analysed sample. The main phase is represented by smectite, commonly associated to feldspar and silica polymorphs (e.g., cristobalite, quartz). Kaolinite is present only in group 1 samples, strictly associated with halloysite and the absence of illite/mica, variously present in the other groups. The only exceptions, due to the scarceness of clay minerals, are represented by the samples FA49, being rich in silica phases (also microcrystalline, like opal) and poor in clay minerals, and FA83 dominated by Al-hydroxides (6.09 Å, 3.16 Å, 2.35 Å and 1.86 Å peaks; Fig. 3.6d), showing features better fitting with silicic facies (Fulignati et al., 1998; Balić-Žunić et al., 2016). The intermediate-argillic alteration is usually linked to weakly acid fluids (pH 4-6) and characterized by the presence of smectite and kaolinite group minerals, while the silicic-alteration, marked by the nearly complete hydrothermal alteration of the host rocks to silica phases, due to the interaction with extremely acid fluids (pH <2) (Wohletz and Heiken, 1992). These types of hydrothermal alteration facies are typical of an acid-sulfate condition, associated with acid waters that contain residual magmatic volatiles (Heald et al., 1987). Only the earlier phases (i.e. low-T) were recognized, while the high-T ones, such as the sericitic and propylitic facies, are completely absent.

From a general view of the overall data, it is interesting to note a good correspondence between the mineralogical composition of the samples and the sampling locations with respect to the main vents. Smectite-rich samples mainly accompanied by cristobalite, feldspar and alunogen, are located near or in proximity to the vents (both mains and minors), where pervasive alteration, fluids with pH of ~3.5 at temperatures of 108-119°C and soil temperatures up to ~70°C, are recognized; while the kaolinite-rich samples, accompanied by halloysite and subordinate smectite (FA47-FA65-FA72), lies far from the main thermal features (Fig. 3.2b), where soil temperatures of up to ~45 °C are reached. In the smectite-rich zone, samples FA103a and FA103b, could represent transitional facies between the two subzones (i.e. smectite-rich and kaolinite-rich zones), testified by the richness of smectite, coupled with the less amount of kaolinite and halloysite. Transitional facies can be considered the group 3 samples too (Table 3.3), representing a mineralogical assemblage moderately found near the vents (Fig. 3.2b), as testified by the presence of alunogen, frequently related to evaporation of acid water in low-temperature fumaroles (around 100°C) contexts (Balić-Žunić et al., 2016). Only two samples do not fit with this general interpretation, as the FA49 (silica-rich and smectite-poor; Table 3.3 and Fig. 3.6c) lies right above a diffuse degassing area (Fig. 3.3a) where the highest soil temperatures are reached (i.e. ~83°C), and the FA83 shows a mineralogical assemblage where clay minerals are almost totally absent (Table 3.3; Fig. 3.6d). These latter two samples could represent conditions associated with peculiar local characters. The mineralogical association of the FA49 is indicative of low-crystallinity, possibly associated to an extremely rapid crystallization or to secondary events of decreasing grade of organization

of the silica crystalline structure, like "silica flooding" (Lagat, 2010), maybe related to a past fumarolic activity. In fact, this area is located in the most north-easterly part of the area, where a NE-striking discontinuity is recognized (Fig. 3.8).

If on one side, a moderate agreement is found for mineralogical assemblages and related soil temperatures, on the other side the clay-minerals assemblages do not fit with the pH conditions proposed for the smectite group minerals, that would require higher pH than those found in the fumarole's fluids (e.g. Patrier et al., 2003; Amram and Ganor, 2005). This inconsistency could be associated with the reaction between the fluids of the vents (pH 3.5) and the primary minerals consuming H^+ through a hydrolysis process, generating the pH of the fluids in the porous host rock to a more neutral condition and thus allowing the formation of smectite minerals. In this context, kaolinitic soils can be interpreted as ancient zones with a longer time of fluid circulation and development of leaching processes, with the consequent decrease of the pH, while the smectitic soils would represent the current active hydrothermal discharges, with the presence of neutralization processes. From the mineralogical zones and their extensions, the samples-related soil temperatures and the areal distribution of the main thermal features (i.e. fumaroles, mud pool, minor vents and the degassing area), the presence of two main lineaments NW-striking and NE-striking is pointed out (Fig. 3.8).

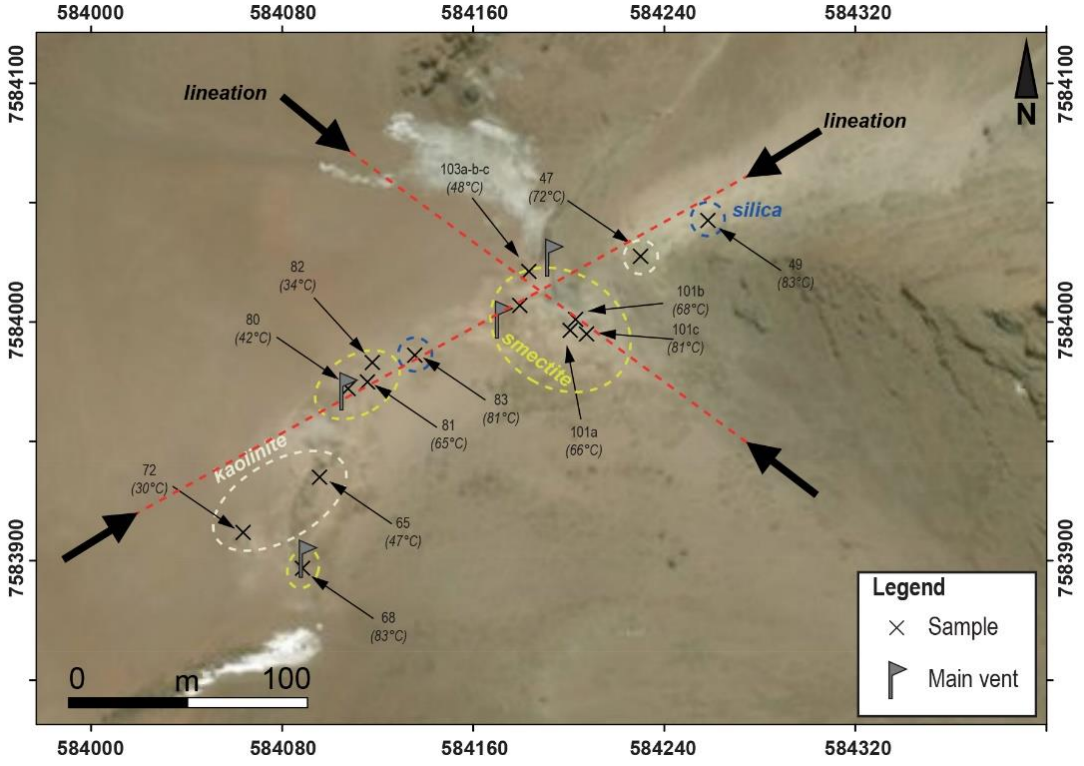

Figure 3.8 *- Schematic model of the mineralogical zonation, based on the main minerals recognized in the fumarolic field. For each sample the relative soil temperature is reported; yellow dotted lines indicate the smectite-rich areas; white dotted lines indicate the kaolinite-rich areas; blue dotted lines indicate the sample where a silicic alteration facies is recognized. Two main lineaments, NW-striking and NE-striking, based on the thermal features position, soil temperatures and on the extensions of the distinct mineralogical zones, are highlighted.*

3.7. Final remarks

Mineralogical studies on the vertical and superficial distribution of the clay minerals forming the hydrothermal system of the Cerro Pabellón active geothermal field, where carried out. From the mineral assemblages recognized in the fumarolic field and in the two boreholes located in the Pampa Apacheta, the system seems to be characterized by both acid-sulfate (fumarolic field) and adularia-sericite (production well) alteration types, which represent the two most typical hydrothermal alteration assemblages linked to geothermal systems in active or recent volcanic areas (Wohletz and Heiken, 1992).

The acid-sulfate alteration characterizes the upper parts of the Apacheta volcano, where the rising magmatic gases are mixed with shallower aquifer, producing acid-sulfate waters (Tassi et al., 2010). Two main subzones are recognized: (i) one characterized by high amounts of smectite, mainly coupled with cristobalite and feldspar, and (ii) one characterized by kaolinite, mainly coupled with halloysite and subordinate smectite. It has been constrained how these subzones show a good correspondence with the thermal features' location, and a moderate accordance with the soil temperatures measured in the sampling locations. Conversely, a not-fitting with the pH conditions of stability for the smectite clay minerals group is observed. Although a unique explanation to this controversy is difficult, our preliminary data indicate the involvement of neutralization processes in the active vents areas to explain the presence of smectite in such acid environment (i.e. pH 3.5), and typical acid-fluids leaching processes in the far-from-vents areas, where kaolinite is the main mineralogical phase.

The adularia-sericite alteration characterizes the geothermal reservoir and, from the mineralogical assemblages recognized, is possibly associated with fluids with neutral pH (Heald et al., 1987). Two main clay minerals transitions were detected in the thick and impermeable clay-cap units: the smectite to illite and the smectite to chlorite. In fact, the illite and chlorite, only prevail in rock samples from the reservoir domain, where mixed-layer I-S and C-S are almost absent. In both reaction series, a continuous and slow reduction of the proportion of smectite layers in mixed layers with depth was observed. The impermeability of the clay cap of the geothermal system, would not favour the advance of I-S and C-S reaction series.

Detailed studies by XRD of clay minerals might help to understand the formation processes of the hydrothermal minerals and how these mineralogical transformations might be controlled not only by temperature (and depth) but also by kinetics related to permeability/porosity that might enhance (or prevent) mineral transformations. Consequently, detailed studies of alteration minerals in continuous drill cores, cuttings and superficial alteration zones, should improve the data available for better understanding of the processes that control the development of alteration zones in active geothermal fields and thus the reliability of conceptual models.

CHAPTER 4

SEALING CAPACITY OF CLAY-CAP UNITS OF THE GEOTHERMAL RESERVOIR

THE MAIN PARTS OF THIS CHAPTER ARE IN PREPARATION FOR THE SUBMISSION AS:

Taussi, M., Nisi, B., Pizarro, M., Morata, D., Veloso, E.A., Tassi, F., Vaselli, O., Renzulli, A. *Sealing capacity of clay-cap units above the blind geothermal system of Cerro Pabellón (northern Chile).*

4.1. Introduction

The Cerro Pabellón geothermal power generation project is a high enthalpy geothermal system (T>200 °C; Aravena et al., 2016) located in the Antofagasta region (Northern Chile; 21,86°S; 68,15°W; 4,520 m) (Fig. 4.1). The commercial operations started in March 2017, involving the production of electrical energy through a binary power plant (Organic Rankine Cycle) with an installed capacity of 48 MWe (ENEL, 2012). The project area is set in the downward block of the Pabelloncito graben, delimited by two NW-SE oriented major lineaments (Fig. 4.1). This tectonic structure hosts the geothermal reservoir, whose thickness is estimated to be between 900 and 1,100 m (Aravena et al., 2016), with an area ranging between ~4 and ~25 km^2 (Urzua et al., 2002; Aravena et al., 2016). The geothermal system is sealed by a thick (~300 m) argillic zone (the clay-cap), which covers the deeper propylitic zone. According to the mineralogical assemblage (Chapter 3), the propylitic facies is likely associated with near-neutral pH fluids (Heald et al., 1987), and linked to shallow heat sources (~4-8 km; Chapter 2). The site was discovered by CODELCO (Chilean national mining company) at the end of '90s during water-related exploring surveys (Urzua et al., 2002). At the surface, the sole evidences of hydrothermalism are represented by relatively large areas of argillic alteration, related to past and present fumarolic activity (Aguilera et al., 2008), mainly distributed on the western, north-eastern and eastern flanks of the Apacheta-Aguilucho Volcanic Complex (AAVC), i.e. to the west of the Cerro Pabellón geothermal area (Fig. 4.1b). The scarceness of hydrothermal manifestations in the studied area has been ascribed to the presence of the thick clay-rich zone that prevents the ascent of geothermal fluids, masking the typical features of active high enthalpy geothermal systems (Chapter 3). The presence of a clay-cap (or cap-rock) is one of the key components of geothermal systems to guarantee adequate fluids pressure and temperature conditions at depth (Corrado et al., 2014). Seal integrity of the impermeable units through surface monitoring of CO_2 flux from the ground may provide useful information of gas leakage from active hydrothermal system (Chiodini et al., 2005; Annunziatellis et al., 2008; Todesco and Giordano, 2010; Carapezza et al., 2015). Flux measurements of CO_2 in blind or hidden geothermal systems, i.e. when hot springs, fumaroles, mud pools, and geysers are absent, are commonly coupled with complementary methodologies (e.g. $\delta^{13}C$-CO_2 isotopes; Hanson et al., 2014). In geothermal areas or in active volcanic systems, diffuse CO_2 soil degassing is frequently associated with heat anomalies of the ground (Giammanco et al., 2016) since CO_2 and high-enthalpy fluids, such as steam, often have similar origin and both follow the same transport mechanisms (Aubert and Baubron, 1988; Chiodini et al., 2001, 2005; Fridriksson et al., 2006). Thus, soil temperature is a useful parameter to evaluate how efficiently the geothermal fluids are transported to the surface in relation to the depth of the gas source, even when CO_2 soil fluxes are low. The blind geothermal system of Cerro Pabellón is a suitable example where the CO_2 flux and temperature pair can be applied to verify (i) the

sealing capacity of the clay-cap units and (ii) the occurrence of active geological structures. Soil temperature and CO_2 measurements (~500 points) were conducted during stable and dry conditions in November 2016 and September and November-December 2017, respectively.

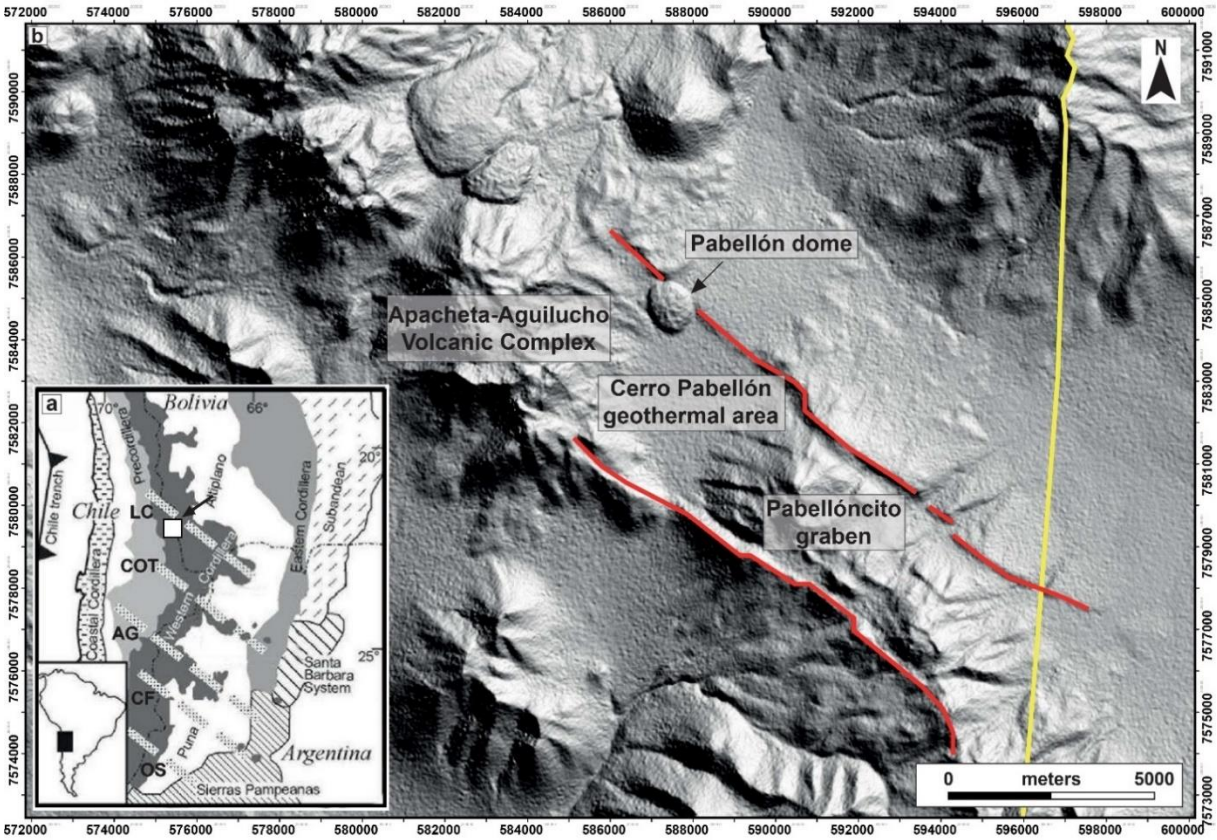

Figure 4.1 *- a) Central Andes NW–SE trending main lineaments associated with magmatic activity (dashed lines); these include the Lipez-Coranzuli (LC), Calama–Olacapato–El Toro (COT), Archibarca-Galan (AG), Culumpaja–Farallon Negro (CF), and Ojos del Salado (OS) (modified from Acocella et al., 2011); b) location map of the Cerro Pabellón geothermal area. The red lines define the Pabellóncito graben main faults. The yellow line is the national border with Bolivia.*

4.2. Geological background

The Cerro Pabellón area is located at the base of the eastern flank of the AAVC, a Pliocene-Pleistocene composite stratovolcano (Aguilera et al., 2008; Mercado et al., 2009), mainly characterized by andesitic, dacitic to rhyolitic products belonging to the high-K calk-alkaline series (Chapter 2). The products of the AAVC were emplaced on a volcanic basement consisting of Miocene andesitic-to-dacitic eroded volcanoes and dacitic-to-rhyolitic pyroclastic flows (Ramírez and Huete, 1981), over which ignimbrites and andesitic lava flows are partially exposed subaerially. On the flanks of the AAVC, large areas of hydrothermal alteration are present, partially associated with past and present fumarolic activity (Urzua et al., 2002; Aguilera et al., 2008). The mineralogical association in the active fumarolic area is related to argillic alteration processes, dominated by clay minerals belonging to the smectite and kaolinite

groups, with subordinate cristobalite and halloysite (Chapter 3). The mineralogical assemblage is referred to an acid-sulfate alteration facies, due to the interaction between the rising magmatic gases of the AAVC with shallow aquifers (Tassi et al., 2010). The Cerro Pabellón project area is characterized by a thick argillic clay-cap (~300 m), set above a sub-propylitic and a propylitic alteration zone (Chapter 3). The superficial alteration zones are weakening structures of the volcanic edifice, as also confirmed by the presence of a debris avalanche deposit, morphologically emphasized by small hummocks, in the eastern flank, and mainly consisting of hydrothermally-altered lava fragments (Godoy et al., 2017b).

As concerning the tectonic setting of the studied area, a series of NW-SE-oriented morphological lineaments are present. Two major lineaments form the ~4 km wide and ~20 km long Pabellóncito graben (Fig. 4.1b). This Late Pliocene-Quaternary structure (Tibaldi et al., 2009; Tibaldi et al., 2017) shares the same direction of a series of NW-SE-trending faults and lineaments that crosscut the Andean Belt at several latitudes, such as the Lípez-Coranzuli, the Calama-Olacapato-El Toro, the Archibarca-Galan, Culumpaja–Farallon Negro, and Ojos del Salado regional lineaments affecting the Paleozoic rocks (Fig. 4.1a; Salfity, 1985; Marrett et al., 1994; Riller et al., 2001; Tibaldi et al., 2009; Acocella et al., 2011). Individual faults along these large NW-SE-trending faults suggest left-lateral displacements over NW-trending faults and left-lateral/normal displacement over subsidiary W-trending faults forming a duplex-like structure (Giordano et al., 2013). Volcanoes, monogenetic cones and hydrothermal systems are commonly located and built atop the trace of NW-trending faults and lineaments (e.g. Davidson and de Silva, 1992; de Silva et al., 1994; Giordano et al., 2013; Godoy et al., 2014; Rivera et al., 2015; Tibaldi and Bonali, 2018), suggesting that these structures act as fluid conduits towards shallower crustal levels (e.g. Chernicoff et al., 2002).

4.3. Fluid geochemistry at AAVC

Presently, the hydrothermal activity at the Cerro Pabellón geothermal system is represented by two super-heated fumaroles with temperatures of 108 and 118 °C (boiling point of water at that elevation is ~84 °C) (Urzua et al., 2002; Tassi et al., 2010), mud pools, a diffuse degassing zone and numerous minor gas vents, located in an area of about 0.03 km^2 on the top of the Apacheta Volcano at about 5,150 m.

Fumarolic gas discharges showed very low gas/H_2O_{vap} ratio (0.01) with 2.5 wt% of non-condensable gases (NCG) dominated by CO_2 and N_2. These values were similar to those of the liquid-dominated geothermal reservoir (i.e. 20% of steam, 80% of liquid; ENEL, personal communication) of sampled from the production wells, as the gas/H_2O_{vap} ratio was of 0.007 (mean between 0.004 and 0.012; ENEL, personal communication). Among the acidic gases discharged from the fumaroles, the concentrations of H_2S were between 5,996 and 7,987 µmol/mol, with those of HCl and SO_2 varying from 563 to 607 and from 110 to 146 µmol/mol,

respectively, i.e. higher with respect to those recorded from other geothermal systems from northern Chile (Tassi et al., 2010). Conversely, in the 187 m-depth PAE-1 exploration well, located in the Pampa Apacheta at about 4.5 km E of the AAVC fumaroles (Fig. 4.2), no HCl and SO_2 were detected, and much lower contents of H_2S were measured (<0.0106 mole fraction of total NGC; Urzua et al., 2002). Low methane abundances (4.0-9.6 μmol/mol) and relatively high ratios of N_2/Ar (388-442), indicating the presence of extra-atmospheric N_2 (Urzua et al., 2002), were measured. The isotopic signatures of CO_2 provided evidence of mantle gas contribution to the hydrothermal system, as a matter of fact the $\delta^{13}C$–CO_2 values (−4.76‰, expressed in V-PDB; Tassi et al., 2010) overlapped the typical range of mantle CO_2 (Rollinson, 1993; Hoefs, 1997; Ohmoto and Goldhaber, 1997).

The helium isotopic vales (expresses as *R*/Ra) ranged between between 1.65, in the PAE-1 well (Urzua et al., 2002) and up to 1.85 in the fumaroles (Urzua et al., 2002; Tassi et al., 2010), i.e. significantly lower than those expected for an active subduction environment (i.e. >5; Mason et al., 2017). These low values were related to a possible dilution of the primary mantle-derived ^{3}He-rich magmatic component by ^{4}He produced in the thick crust of this part of the Andes (>70 km; Beck et al., 1996), or to an aggressive alteration of host rocks in a magmatic–hydrothermal environment that enhanced the release of ^{4}He from the AAVC extrusive and subvolcanic rocks (Christenson et al., 2002).

The thermal waters discharging from the AAVC fumarolic field presented temperatures at about 83-84 °C, low pH (<3.57), and calcic-sulfate composition (Tassi et al., 2010), likely representing steam-heated acidic-sulfate waters, produced by shallow aquifers heated by inputs of deep vapor phases rich in S-bearing compounds. According to Tassi et al. (2010), the water isotopic compositions ($\delta^{18}O$ and δD) was interpreted as the result of a mixture between meteoric and magmatic fluids. The thermal waters showed a Total Dissolved Solids (TDS) content of < 2700 mg/L with low contents of boron, lithium and silica (0.1-1.7, 0.1, and 51-59 mg/L, respectively). This evidence coupled with the high temperatures constrained by gas geothermometers (from 200 up to 350 °C, in a slightly oxidizing environment; Urzua et al., 2002; Tassi et al., 2010), and consistent with those measured from the production wells (i.e. 212-256 °C; Aravena et al., 2016), suggested a significant contribution from a magmatic-related source to the surface manifestations. As a matter of fact, the fluids of AAVC seem to be produced by a non-conventional hydrothermal system still directly linked to the recent volcanic activity, due to the high temperature associated with a significant amount of magmatic gas species (Tassi et al., 2010).

4.4. Material and methods

4.4.1. Soil CO_2 fluxes measurements at the Cerro Pabellón area

In September and November-December 2017 (with dry and stable atmospheric conditions), 498 diffuse CO_2 flux measurements were carried out along some of the principal morphological and/or structural lineaments of the Cerro Pabellón geothermal field and AAVC, as follows: (i) western flank of AAVC, (ii) eastern sector of Pampa Apacheta and (iii) NE-fault and (iv) SW-fault systems of the Pabelloncito graben (Fig. 4.2). Soil CO_2 flux measurements were carried out following the accumulation chamber method (e.g. Nisi et al., 2013; Rodrigo-Naharro et al., 2013; Tassi et al., 2013; Elío et al., 2016), by simultaneously using two instruments. The instruments were calibrated before each survey and have a company reported lower detection limit of 0.044 $g \cdot m^{-2} \cdot day^{-1}$ (https://www.westsystems.eu/it). The equipment, operating in a dynamic mode, consisted of a metal cylindrical vessel (the accumulation chamber), an Infra-Red spectrophotometer, an analog-digital converter, and a palmtop computer. The accumulation chamber had a volume of ~2.8 L and was equipped with a ring-shaped perforated manifold to re-inject the circulating gas through a low-flux pump (20 $mL\ s^{-1}$) thus, ensuring the mixing of the soil gas into the chamber. The Infra-Red spectrometer consisted of a LICOR Li-820 detector equipped with a sensor operating in the range 0-20,000 ppm of CO_2. The soil gas circulated from the chamber to the Infra-Red sensor and vice versa by a pump (~1 $L\ min^{-1}$). The signal was converted by the analog-digital converter and transmitted to a palmtop computer, where a CO_2 concentration vs. time diagram was plotted in real time. Soil temperature was measured at each site, within 0.01 m from the accumulation chamber, using a Hanna HI-935005N K-Thermocouple (accuracy of ± 0.1 °C) in the first 10 cm. The different areas were covered as much as possible with a regular grid, whose nods were located with a portable GPS Garmin Etrex 10, at a 20–30 m grid spacing. Few measurements (< 60) were conducted in the Pampa Apacheta, due to a) work in progress at the geothermal power plant, b) presence of gas-pipelines, and c) absence of geological structures recognized from Landsat images (Fig. 4.2). The spatial distribution of the diffuse CO_2 soil gas spots, as well as their density, was strongly affected by logistics and the lack of a soil cover in several zones where compact hard lavas were cropping out. Ambient air temperature and barometric pressure were recorded for every sample site.

4.4.2 Soil temperatures measurements at the AAVC fumarolic field

Soil temperatures at the fumarolic alteration zone were measured in November 2016. The rectangular-like-shaped field, located on the top of the Apacheta stratovolcano at about 5,150 m a.s.l., is striking NE-SW with a length of ~400 m, and a width of ~80 m (Fig. 4.2). Temperature soil profiles at 10, 20 and 30 cm depths (99 points), located with the same

portable GPS described above (i.e. Garmin Etrex 10), were carried every ~15 meters with a Hanna HI 98509 thermocouple (accuracy of ± 0.3 °C).

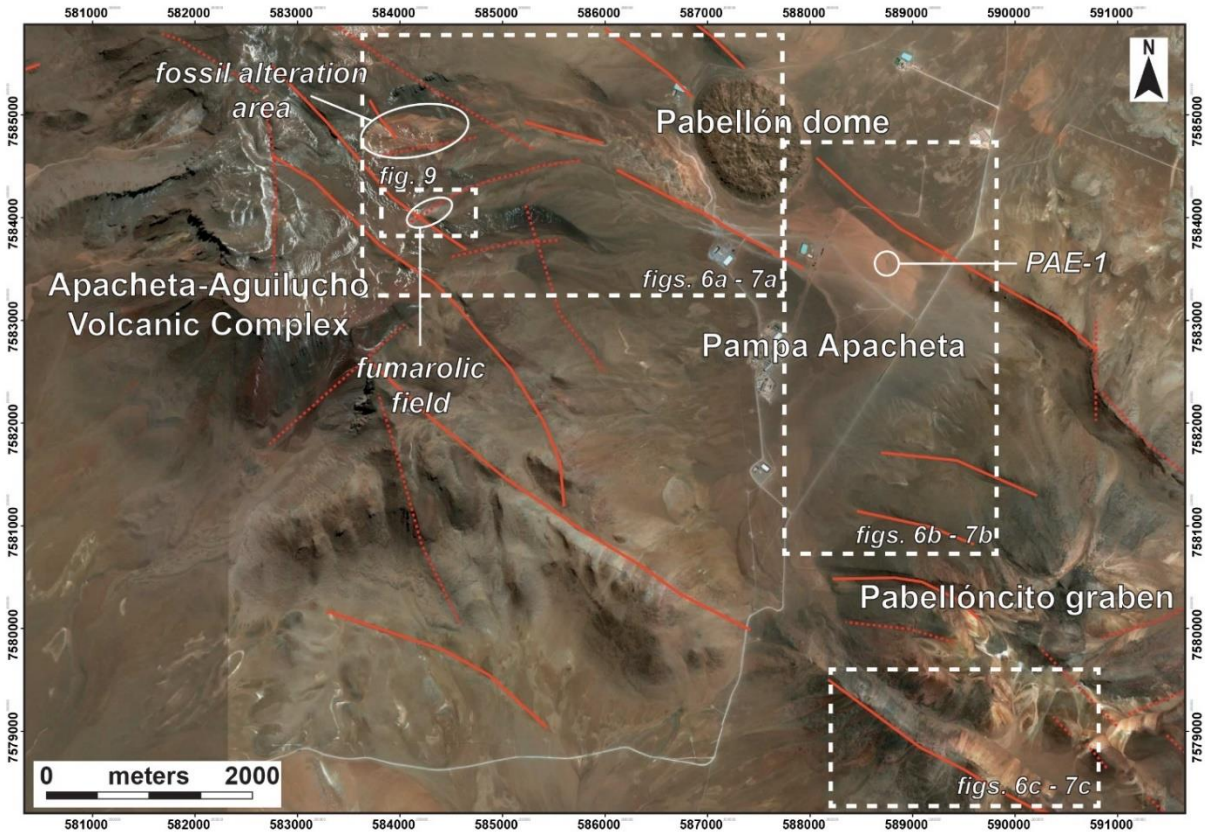

Figure 4.2 *- Map of the Cerro Pabellón geothermal field. Red lines represent the main structural and morphological lineaments available in the literature (Ahumada and Mercado, 2009; Rivera et al., 2015; Sellés and Gardeweg, 2017), photo-interpretation and field survey. Location of the investigated sites described in the text and in the following figures is reported. The dotted boxes are referred to the maps in Figures 4.6, 4.7 and 4.9.*

4.4.3 Soil CO_2 fluxes and temperature data processing

Soil CO_2 flux values in hydrothermal areas are characterized by complex statistical distributions, which generally reflect the coexistence of different CO_2 sources, e.g. biogenic and endogenous (e.g. Cardellini et al., 2003; Nisi et al 2013; Tassi et al; 2013). These complex distributions result on a curve with different inflection points that allow to discriminate different populations. The CO_2 flux values, as well as the superficial soil temperatures, were analyzed using the Graphical Statistical Analysis (GSA) method (Chiodini et al., 1998), performed according to the graphical procedure proposed by Sinclair (1974). Rosner's test (Rosner, 1983) was also applied to estimate the background value of the CO_2 efflux and to discretize the possible outlier values of the dataset with a significance level of 1%. Distribution temperature maps in the fumarolic field were obtained using the ordinary kriging of the values in ArcGIS® software by Esri, using the Geostatistical Analyst tool. Kriging allows to estimate

the variable of interest at unsampled locations through a weighted linear combination of neighboring observations over a regularly spaced grid.

4.5. Results

4.5.1 Soil CO_2 flux and soil temperatures

Soil CO_2 efflux values ranged from < detection limit values (detection limit: d.l. < 0.044 $g \cdot m^{-2} \cdot day^{-1}$) to about 25.00 $g \cdot m^{-2} \cdot day^{-1}$, with an arithmetic mean of 0.83 $g \cdot m^{-2} \cdot day^{-1}$, standard deviation of ± 1.99 $g \cdot m^{-2} \cdot day^{-1}$ and a median of 0.56 $g \cdot m^{-2} \cdot day^{-1}$. A non-parametric distribution with a strongly positive skewness (9.06) and only few anomalous detectable values, is highlighted from the frequency plot (Fig. 4.3a) and the Shapiro-Wilk (Royston 1982a; 1982b), and Lilliefors (1967) statistics tests used to examine the normality (or lognormality) of the data set. The cumulative probability plot of the CO_2 flux data (Fig. 4.3b) indicates two inflection points, at the 91.7 and 98.6 percentiles, respectively, suggesting the presence of at least three different populations. The average soil CO_2 efflux values of the three populations (A, B and C) are 0.56, 1.89, and 15.33 $g \cdot m^{-2} \cdot day^{-1}$, respectively. According to the Rosner's test (Rosner, 1983), only one possible inconsistent value (24.96 $g \cdot m^{-2} \cdot day^{-1}$) was recognized. The background threshold value (BTVs) and the upper tolerance limit (UTL) were calculated by either considering or not considering the 47 values below the instrumental detection limit. The results are similar, with a BTVs ranging between 1.9 and 2.1 $g \cdot m^{-2} \cdot day^{-1}$. The main statistical parameters of the different populations of CO_2 flux are resumed in Table 4.1.

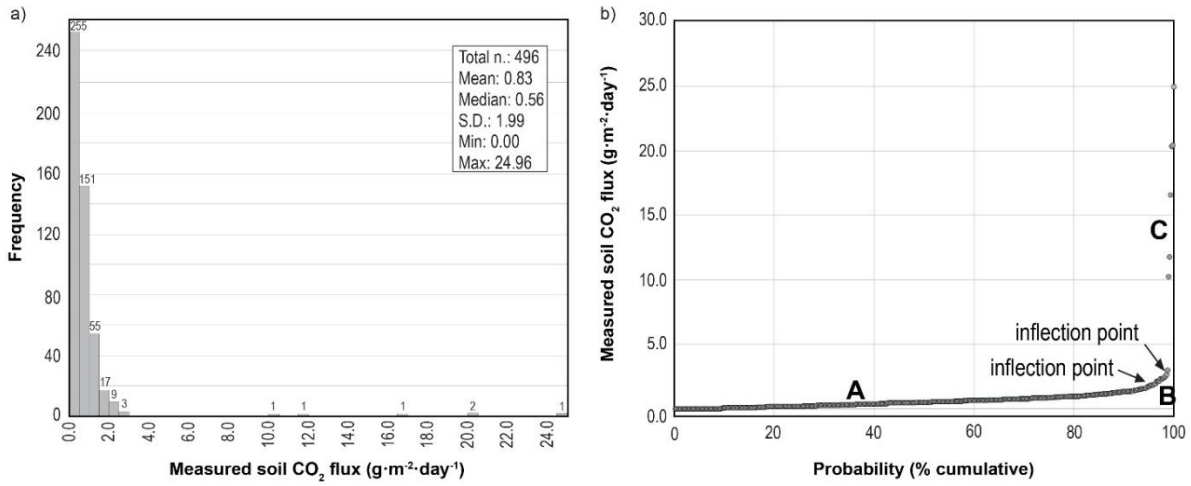

Figure 4.3 *- a) Histogram of distribution frequency of the CO_2 efflux values from Cerro Pabellón area; inset table shows the main statistical parameters of the distribution; b) cumulate probability plot of soil CO_2 flux measurements of Cerro Pabellón area where the main inflection points and the three different populations (A, B and C) are highlighted.*

Table 4.1

Estimated parameters of the partitioned populations of CO_2 (GSA method)

Population	CO_2 flux (g m^{-2} day^{-1})	Measurements (no.)	Frequency	Mean (g m^{-2} day^{-1})	Median (g m^{-2} day^{-1})
B.d.l.	< 0.044	49	9.8%	-	-
A (background)	0.05 - 1.42	411	82.5%	0.56	0.48
B	1.42 - 2.67	31	6.2%	1.89	1.82
C	2.67 - 24.97	7	1.4%	15.33	16.60
Total	0.00 - 24.97	498	100.0%	0.83	0.56

Similar results are obtained from the analysis of soil temperature data, which occasionally were lower than the atmospheric temperature, ranged from -1.1 to 29.8 °C (with the exception of one site where a temperature of 33.2 °C was measured) with an arithmetic mean of 17.6 °C, standard deviation of ± 6.4 °C and a median of 18.6 °C. The non-parametric distribution of these values, calculated with the Shapiro-Wilk (Royston 1982a; 1982b), and Lilliefors (1967) tests, is shown in the histogram of Figure 4.4a. Although the shape of their distribution is apparently more regular than that of the soil CO_2 effluxes, the soil temperature values also have a polymodal distribution, as confirmed by the cumulative probability plot (Fig. 4.4b). Two main inflection points are recognized, at the 12.4 and 97.3 percentiles, respectively, suggesting the presence of at least three distinct populations. The average soil temperature values of the three populations (A, B and C) are 4.5, 19.2 and 28.2 °C, respectively. The main statistical parameters of the different populations of CO2 flux are resumed in Table 4.2.

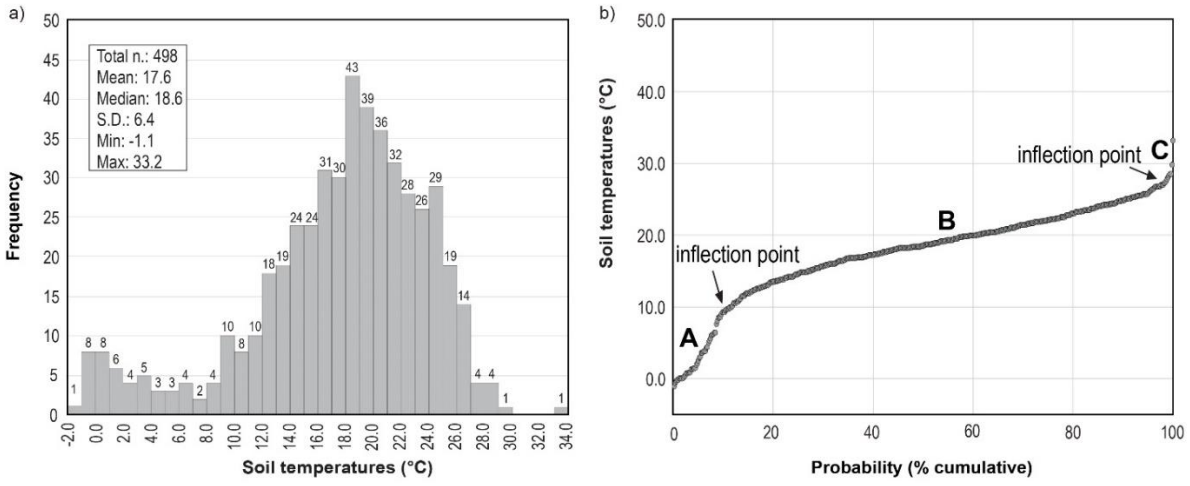

Figure 4.4 *- a) Histogram of distribution frequency of the soil temperature values corresponding to the CO_2 flux measurement points; inset table shows the main statistical parameters of the distribution; b) cumulate probability plot of soil temperature measurements where the main inflection points and the three different populations (A, B and C) are highlighted.*

Table 4.2

Estimated parameters of the partitioned populations of Soil Temperature (GSA method)

Population	Soil T (°C)	Measurements (no.)	Frequency	Mean (°C)	Median (°C)
A	-1.1 - 10.5	62	12.4%	4.6	3.8
B	10.6 - 26.9	423	84.9%	19.2	19.3
C	27.0 - 33.2	13	2.6%	28.2	28.2
Total	0.00 - 24.97	498	100.0%	17.6	18.6

4.5.2 Soil temperatures at the AAVC fumarolic field

On the basis of the statistical tests (Royston 1982a; 1982b; Lilliefors, 1967) and the analysis of soil temperature data at the fumarolic field, only the 10 cm depth measurements seem to show a parametric (log-normal) distribution as evidenced in the histogram of Figure 4.5a, being defined by a positive skewness (0.79). The 20 cm (Fig. 4.5b) and 30 cm depths (Fig. 4.5c) measurements are characterized by a non-parametric distribution, with a negative-trending asymmetry, as demonstrated by the skewness values (0.31 and 0.07, respectively). The soil temperatures seem to have polymodal distribution, as also indicated by the cumulative probability plot for the three temperature datasets (Fig. 4.5d,e,f). Two main inflection points are recognized in each dataset, at the 6.1 and 80.8 percentiles for the 10 cm depth (Fig. 4.5d), at 17.2 and 85.8 percentiles for the 20 cm depth (Fig. 4.5e), and at 27.7 and 81.8 percentiles for the 30 cm depth (Fig. 4.5f), suggesting, once again, the presence of at least three distinct populations. The average soil temperature values of the three populations (A, B and C) for the 10 cm depth are 8.4, 27.1 and 70.7 °C, respectively; for the 20 cm depth are 9.0, 40.0 and 82.3 °C, respectively and finally, for the 30 cm depth are 11.6, 48.6 and 82.4 °C, respectively. The main statistical parameters of the different populations of soil temperatures at each depth (i.e. 10, 20 and 30 cm) are resumed in Table 4.3.

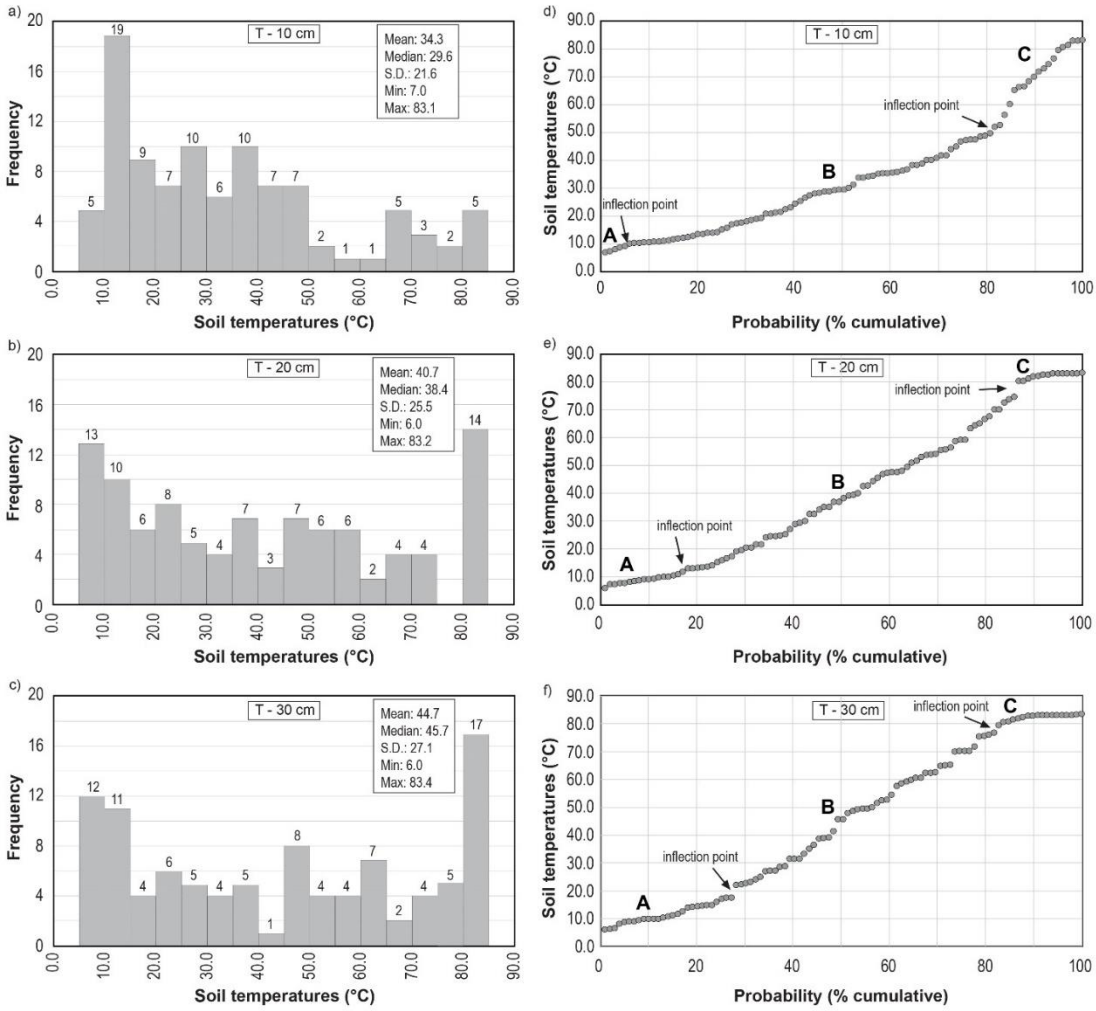

Figure 4.5 - *a), b) and c) Histograms of distribution frequency of soil temperature values at 10, 20 and 30 cm depths, respectively; inset tables report the main statistical parameters of the distributions; d), e) and f) cumulate probability plots of soil temperature measurements where the main inflection points and the three different populations (A, B and C) for each depth are highlighted.*

Table 4.3

Estimated parameters of the partitioned populations of Soil Temperature at the AAVC fumarolic field (GSA method)

Populations	Soil T (°C)	Measurements (no.)	Frequency (%)	Mean (°C)	Median (°C)
10 cm					
A	7.0 - 11.3	14	14.1%	9.8	10.5
B	11.4 - 49.7	66	66.7%	29.3	29.1
C	49.8 - 83.1	19	19.2%	70.7	71.8
Total	7.0 - 83.1	99	100%	34.3	29.6
20 cm					
A	6.0 - 11.0	16	16.2%	8.9	8.9
B	12.0 - 74.6	69	69.7%	39.6	39.1
C	80.4 - 83.2	14	14.1%	82.3	82.9
Total	6.0 - 83.2	99	100%	40.7	38.4
30 cm					
A	6.0 - 17.5	27	27.3%	11.6	10.8
B	22.0 - 76.7	54	54.5%	48.6	49.4
C	79.4 - 83.4	18	18.2%	82.4	83.0
Total	6.0 - 83.4	99	100%	44.7	45.7

4.6. Discussion

Based on the GSA analysis related to the CO_2 flux values, three different populations were recognized and possibly related to different sources or geochemical processes. The low values of the population A (<1.50 $g \cdot m^{-2} \cdot day^{-1}$; Fig. 4.3b), can be referred to CO_2 fluxes associated with soil respiration. In fact, this value is similar to that obtained from Rosner's test used to estimate the background (i.e. ~2.00 $g \cdot m^{-2} \cdot day^{-1}$). Considering the unique features and the scarceness of vegetation of the Atacama Desert, coupled with the low atmospheric pressure at these altitudes (i.e. between 4,500 and 5,150 m a.s.l., corresponding to 543-591 hPa) that should have increased the fluxes (Cannata et al., 2010), a background value of 1.50 $g \cdot m^{-2} \cdot day^{-1}$ can be considered realistic. To the best of our knowledge, no flux data in this sector of the Andes are available in the literature. Consequently, the only comparable values are those reported by Raich and Schlesinger (1992) and referred to desert scrubs from Utah and New Mexico (USA), for which an estimated soil respiration values of about 2.25 $g \cdot m^{-2} \cdot day^{-1}$ was computed and therefore, in agreement with that reported in the present study. According to the maps reported in Figure 4.6, the sites belonging to the population B and C show a scattered distribution, although they appear to be slightly grouped at the base of the volcanic edifice, at the connection with the Pampa Apacheta (Fig. 4.6a). Consequently, tracing a real diffuse degassing structures is not possible.

As a matter of fact, < 10% of the CO_2 flux measurements values from the study area is higher than the background value. Of these exceeding values, the ranges and the mean pertaining to the populations B and C, show a possible correlation with an endogenous, or at least an intermediate (i.e. mixing between endogenous and biogenic) source or geochemical process. In fact, similar ranges and means of values have been recognized in other geothermal and/or active volcanic areas and related to endogenous source/s (e.g. Etna, Vesuvio, Vulcano, Ohaaki hydrothermal field; Giammanco et al., 2016; Cardellini et al., 2003; Chiodini et al., 1998; Rissmann et al., 2012). Nevertheless, no carbon isotopic analyses were carried out, so a clear discrimination of the presence of a deep-seated source of carbon dioxide cannot be defined (Chiodini et al., 2008; Hanson et al., 2014; Venturi et al., 2017).

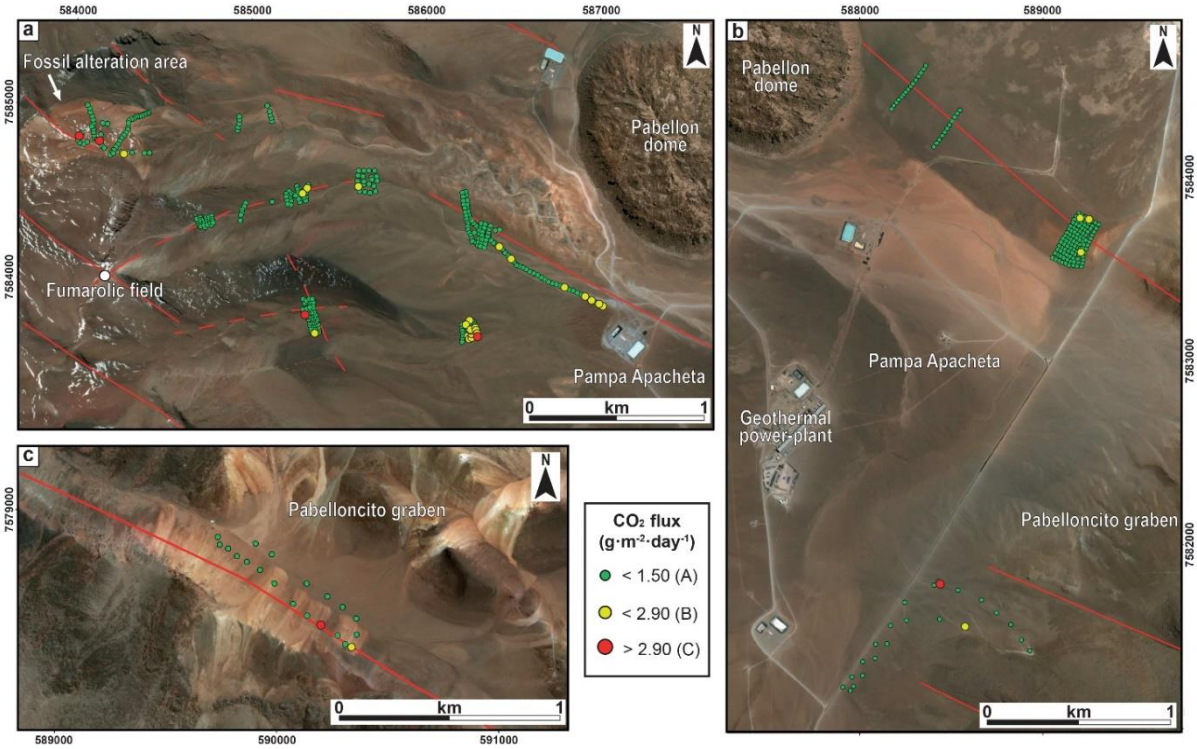

Figure 4.6 *- Dot-map of soil CO2 efflux values in the studied area. The main structural/morphological lineaments (dashed when uncertain), sampling points with the relative range of values and population are reported; a) Western flank of the Apacheta-Aguilucho Volcanic Complex; b) Pabelloncito graben NE-fault and eastern sector of the Pampa Apacheta; c) Pabelloncito graben SW-fault.*

Unlike the CO_2 efflux values, soil temperatures display a different behavior. The lowest values (<10 °C) related to population A are approaching those of ambient temperature and thus, reflecting temperature condition of air-saturated soil. It is worth to mention that population A is represented by 13% of total temperature measurements and the major frequency (~85%) pertaining to population B. Population C is only represented by ~2% of the total values. Although population B and C are not characterized by high CO_2 fluxes, they are possibly recording increasing inputs of heat from high-enthalpy fluids (mostly water vapor; Giammanco et al., 2016), derived from the underneath geothermal system. The spatial distribution of the measured temperatures, distinguished in the three populations, is reported in Figure 4.7. A relatively homogeneous distribution of the intermediate temperatures (population B) is highlighted. The highest temperatures appear to be randomly distributed in the western flank of the Apacheta volcano (Fig. 4.7a), whereas the sites included in the population A are concentrated in the fossil alteration zone (Fig. 4.7a), in the southern part of the Pampa Apacheta (Fig. 4.7b) and Pabellóncito graben SW-fault (Fig. 4.7c).

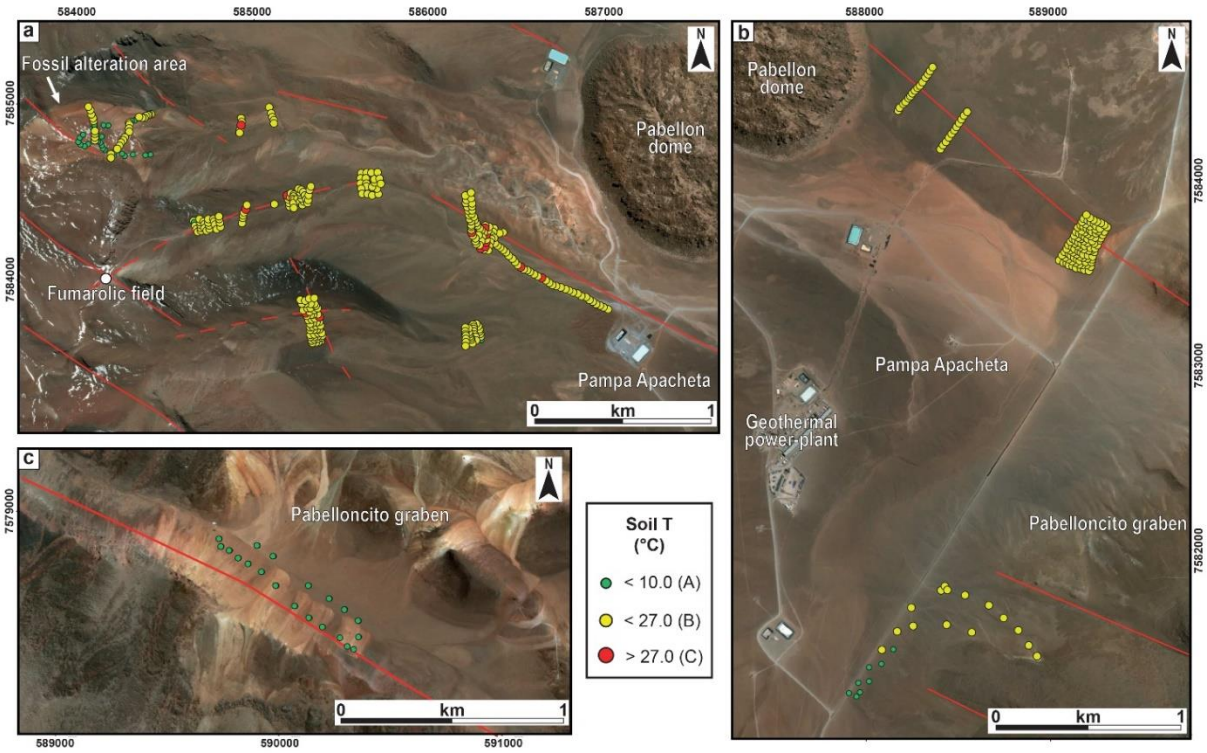

Figure 4.7 *- Soil temperature dot-map in the studied area. Sampling points with the relative range of values are reported; a) Western flank of the Apacheta-Aguilucho Volcanic Complex; b) Pabellóncito graben NE-fault and eastern sector of the Pampa Apacheta; c) Pabellóncito graben SW-fault.*

Even though the presence of three populations was recognized for both soil CO_2 emissions and soil temperatures, no spatial correlation between them was observed (Fig. 4.8). This assumption implies a decoupling between the two parameters, defining that the volcano-tectonic structures do not play a key role in the distribution of the CO_2 flux and temperature (e.g. Chiodini et al., 2015; Giammanco et al., 2016; Rolleau et al., 2017).

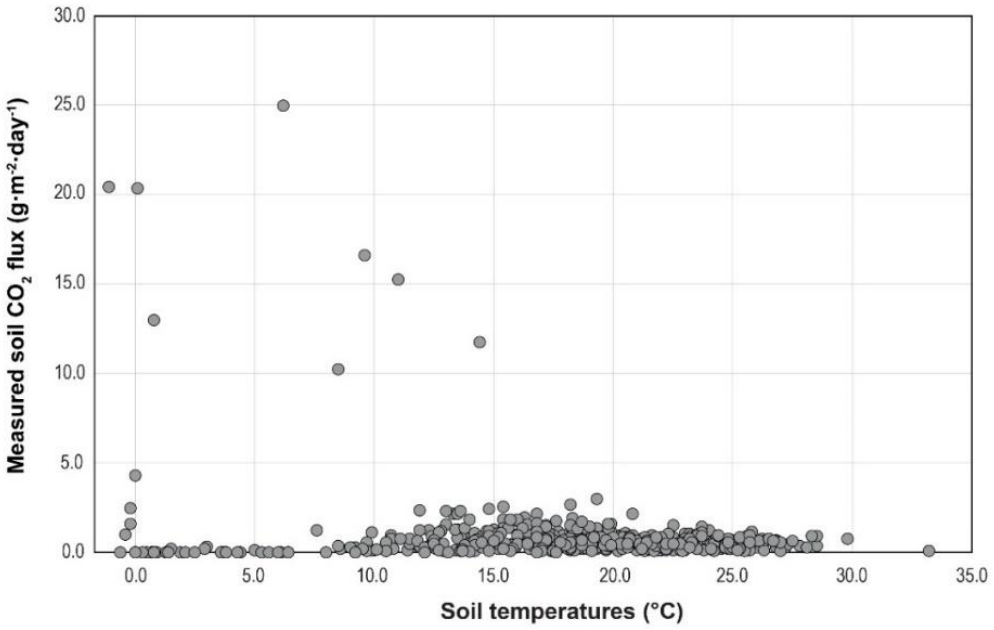

Figure 4.8 *- Soil temperature vs. CO_2 flux binary diagram for all the data measured in the Cerro Pabellón area. No spatial correlation between the two parameters is observed.*

As expected, at the fumarolic field of the AAVC the largest heat and mass transfer occurs, indicating a close association and a direct structural link between the surface and the magmatic gas source. As a matter of fact, this area is located right above the up-flow zone identified by magnetotelluric studies (Urzua et al., 2002). In the fumarolic field, beside the background (A) and intermediate (B) populations, it is worth to note that temperatures approaching that of the boiling water at this altitude are achieved in some sites (population C), indicating therefore heat input from a high-T fluid (Giammanco et al., 2016). The soil temperature maps at 10, 20 and 30 cm depth in correspondence of the AAVC fumarolic field are reported in Figure 4.9, while the main parameters for the modeled maps are summarized in Table 4.4.

Table 4.4.
Relevant parameters of ordinary kriging application

Depth	Variogram model	Transformation	Nugget	Range (m)	N. lags	Lag size (m)
10 cm	Spherical	Log	0.130	56.5	8	18.0
20 cm	Spherical	Box-cox	0.275	53.9	8	18.0
30 cm	Spherical	Box-cox	0.290	59.3	8	18.0

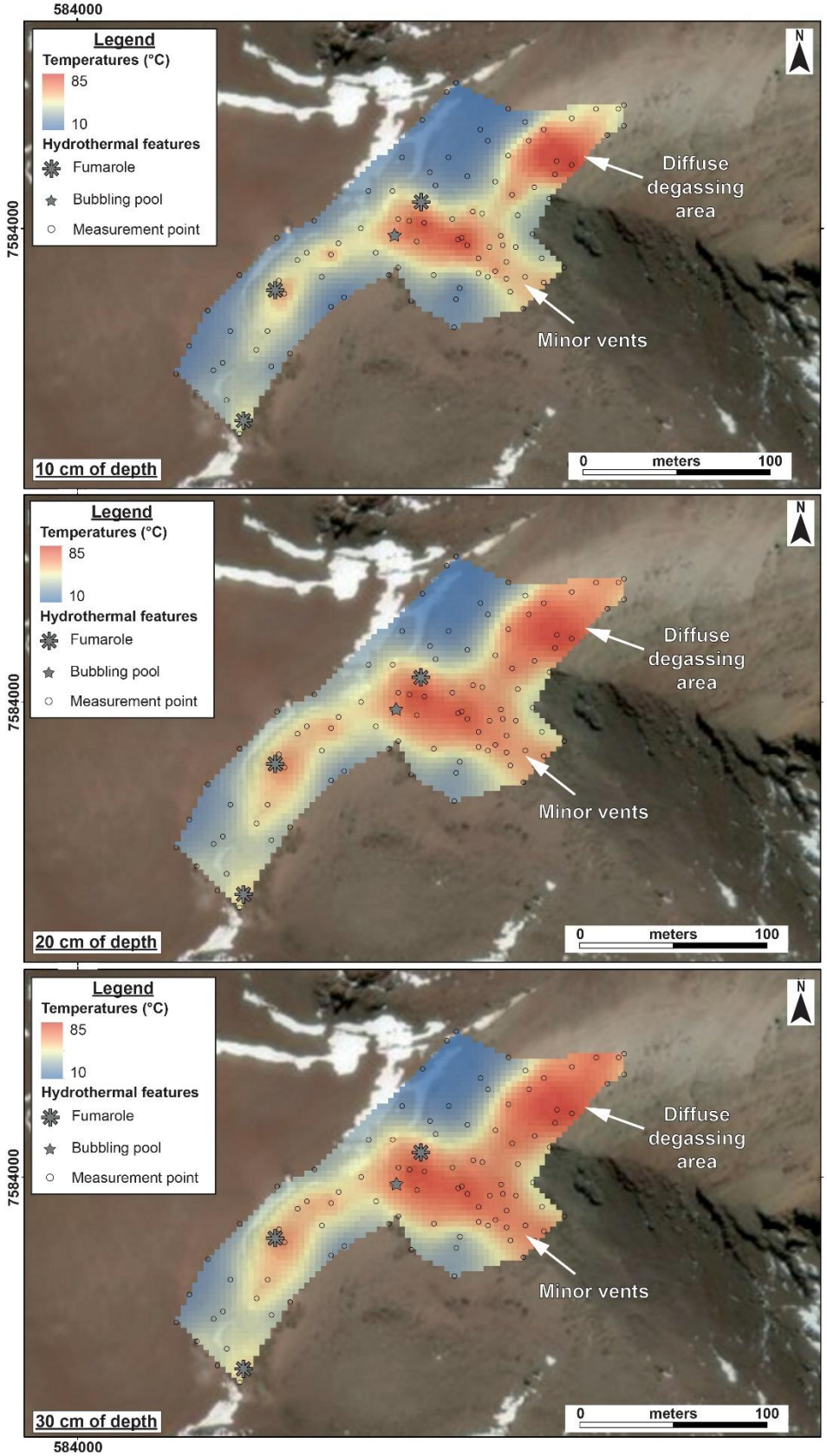

Figure 4.9 *- Iso-soil temperature distribution maps at the fumarolic field of the AAVC at a) 10 cm, b) 20 cm, and c) 30 cm. The main thermal features and the measurement sites (black dots) are also reported. The temperature anomaly becomes wider at increasing depth.*

The thermal anomalies are oriented according to two main trends: NE-SW and NW-SE, which are likely associated with structural discontinuities, along which the main vents and the degassing areas are located (Figs. 4.9 and 4.10). The NE-SW-trending lineament could represent a local transtentional pull-apart area in a major strike-slip faults zone (*sensu* Faulds and Hinz, 2015), that favours the resurgence of the geothermal fluids, acting as the only degassing pathway from the still active magmatic gas source (Tassi et al., 2010). The highest temperatures (up to ~83 °C) are found in the NE portion of the investigated area, where a diffuse degassing zone is present (Figs. 4.9 and 4.10a). Near the fumaroles, the temperatures remain high, although they do not reach those measured in the degassing zone. Nevertheless, the thermal anomaly gradually broadens when passing from 10 to 30 cm depth (Fig. 4.9).

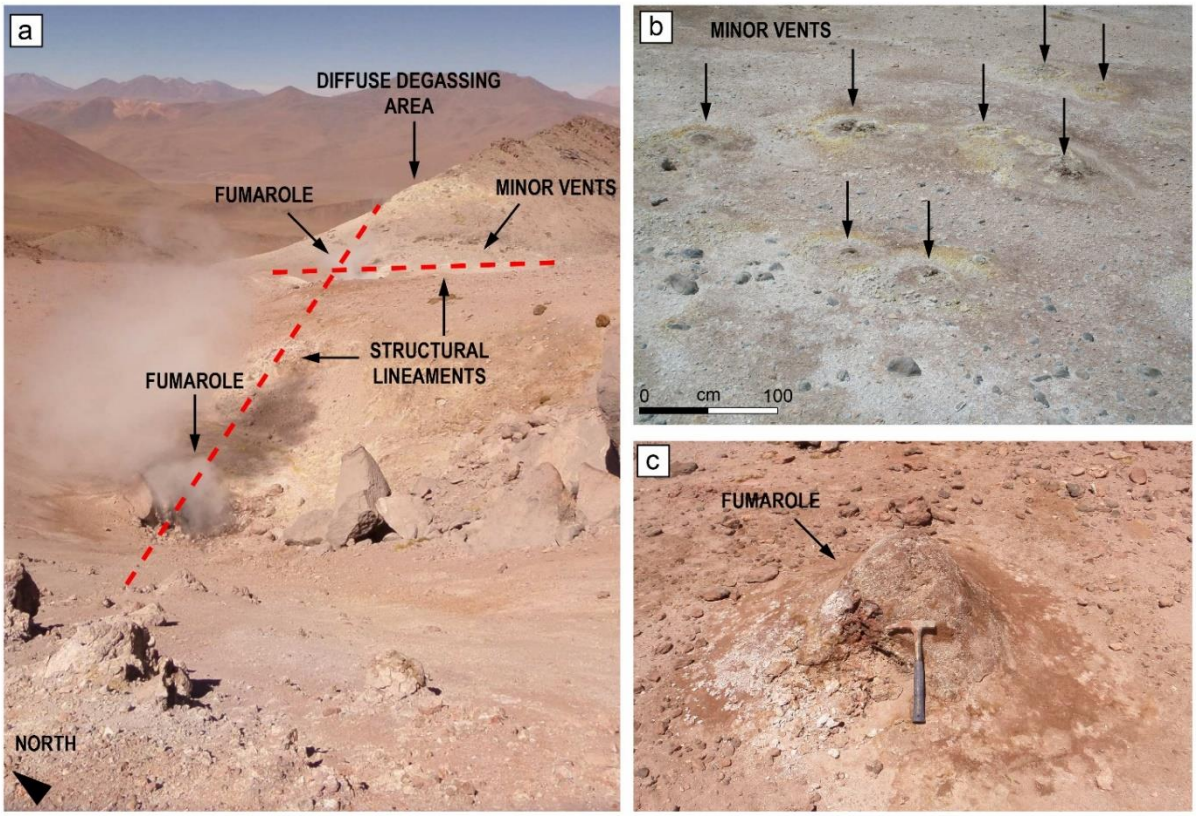

Figure 4.10 *– Main thermal features at the AAVC fumarolic field. a) View toward West; it is possible to note: the two main fumaroles, the diffuse degassing area where the highest temperatures were recorded, and the site characterized by minor steam/gas vents; b) a detailed photo of the minor vents; c) small fumarole located at the SW margin of the studied area.*

Few data about the hydrological setting of the Pampa Apacheta sector are available. From the MT-survey a perched condensate aquifer has been constrained by Urzua et al. (2002) at a depth of ~200-300 m, where the iso-resistivity lines reach the lowest values (i.e. 2 Ω·m). Even though it seems unlikely the presence of a perched aquifer (*strictu sensu*) of this size (i.e. ~100 m), the presence of shallow, even if discontinuous, aquifer/s has been confirmed

during drilling operations in the first ~400 m of the stratigraphic sequence, where different losses of circulation associated to the presence of water, were recorded (ENEL personal communication). Moreover, the presence of illite mixed layer (Chapter 3) at about 270 m and 400 m of depths, could be related to the presence of variable amounts of water. No data related to the thickness of this/these aquifer/s are available. Water boiling temperature at this elevation (~88 °C, at about 4,500 m a.s.l.) is reached at the bottom of the 187 m-depth PAE-1 exploration well, located in the eastern margin of the geothermal system (Urzua et al., 2002; Fig. 4.2) and thus above the clay-cap units identified in Chapter 3. Soil CO_2 degassing in the peripheral volcanic areas is likely related to the input of magmatic CO_2, although the CO_2 flux and the groundwater volume involved are not to be neglected (Inguaggiato et al., 2017). The presence of an impervious clay-cap and the negligible role of the volcano-tectonic structures, coupled with the involvement of "scrubbing" processes (Symonds et al., 1994, 2001) within the liquid-dominated environment (i.e. reservoir) overlying the degassing magma, may explain the lack of strong acidic gas compounds at the surface (Tassi et al., 2010) and the ascent of CO_2-depleted steam in the permeable and unconsolidated deposits characterizing the first 200 m of the Pampa Apacheta stratigraphic sequence (Rivera et al., 2015). As a consequence, those sites belonging population B and C (Figs. 4.4 and 4.5), could be derived from the heating of the shallower aquifer/s, and dispersed laterally over large areas, likely by advective processes. Probably, the aquifer/s maintain such a high temperature due to the scarceness of water recharge characterizing the Atacama Desert (average annual rains < 2mm; Azua-Bustos et al., 2012). A high recharging volume would indeed have produced a relatively low temperatures waters (Minissale, 2018), able to minimize the soil temperature anomaly. Considering the absence of surface hydrothermal features in the geothermal area, the fluids volume involved in the process (i.e. ascending geothermal fluid and shallow aquifer/s) is expected to be small, confirming once more the effectiveness of the clay cover.

4.7. Concluding remarks

Shallow geochemical signals are often able to provide useful information concerning the presence of high-enthalpy geothermal reservoirs or mark changes in the magmatic and/or geothermal systems. Some difficulties may be faced when these signals are hidden or masked by different processes. At Cerro Pabellón, the low CO_2 effluxes measured in the main geothermal areas suggest that contribution by deep-seated CO_2 (magmatic origin) to soil degassing is almost negligible. In fact: (i) the majority (~92%) of the soil CO_2 flux measurements are below background levels (i.e. 1.50 $g \cdot m^{-2} \cdot day^{-1}$); (ii) most shallow (10 cm) soil temperatures are higher than the temperature condition of air-saturated soil (i.e. ~10 °C); (iii) no correlation between soil temperature and CO_2 flux is recorded; and (iv) the only significant thermal anomalies is that registered at the active fumarolic field.

The lack of soil CO_2 anomalies, even above the existing pressurized reservoir, can be due to two main factors: 1) the continuous, ~300 m thick and impervious clay-cap that lies above the propylitic zone, and 2) the magmatic gas scrubbing processes in the liquid-dominated environment, that produce the removal of CO_2, SO_2, and HCl compounds, and the consequent ascent of CO_2-depleted steam, thus permitting the heating of the shallower aquifer/s. The latter resulting at the surface as a diffuse, slight thermal anomaly, recognized by a geostatistical approach, and at 187 m below the surface (i.e. at the bottom of the PAE-1 well) as a wispy flow of steam with measured temperature of 88 °C (Urzua et al., 2002). As a matter of fact, the active fumarolic area, located at the summit of the Apacheta volcano, is the only visible evidence of the hidden geothermal reservoir in the Cerro Pabellón area. This work highlights the significance of the sealing capacity of the thick and impermeable clay-cap able to confine the high enthalpy geothermal fluid of Cerro Pabellón, and confirm the importance of soil temperature and diffuse CO_2 measurements for the detection of possible thermal anomalous areas, thus suggesting that this approach can be extended to other areas of the Andes where the typical thermal manifestations are not present.

CHAPTER 5

OVERALL FINAL REMARKS AND FURTHER WORKS

5.1. Overall final remarks

In order to produce an update conceptual model of the Cerro Pabellón blind (or hidden) geothermal system, where the only evidence of active hydrothermalism is represented by two fumaroles, different methodological approaches were used during the present PhD project. To accomplish the main goals of the research, a multidisciplinary study was involved. The main results achieved, corroborated by previously published data, are resumed as follow.

A polybaric upper crustal magma plumbing system has been working during the ~1 Ma span time of activity of the AAVC area, with two distinct reservoirs (Fig. 5.1). The deeper reservoirs were located at mid-crustal levels (15-20 km) and are akin to the location given for the APMB, involving AFC processes with a dominant role played by amphibole fractionation. Shallower magma chambers were located at depth of 4-8 km allowing further differentiation of the erupted magmas through FC processes, mainly dominated by plagioclase crystallization.
In the evolution of the AAVC area we envisaged a transition of the magmatic regimes from flare-up mode (about 1 Ma; Fig. 5.1a) to steady state (1-0.6 Ma; Fig. 5.1b). This latter magmatic regime characterized by decreasing, but still relatively high rates of mafic magmas recharges for at least 0.4 Ma, kept the upper crustal reservoirs thermally “fertile”, allowing mixing between the new higher temperature magmas with the older, lower-temperature silicic resident magmas to form the abundant andesites and dacites lavas of the composite cones of Apacheta and Aguilucho (Fig. 5.1b). At about 150-100 ka, a change in the magmatism occurred, with inputs of basaltic-andesite magmas into the shallower dacitic chambers, leading to triggering the extrusion of the domes (Fig. 5.1c), which enclaves represent a snapshot of this process at the interface of interactions of the magmas. A revised petrogenetic model, well constrains the textural and geochemical variations in the observed enclaves, which are strongly influenced by the location of crystallization with respect to the andesite-dacite interface.

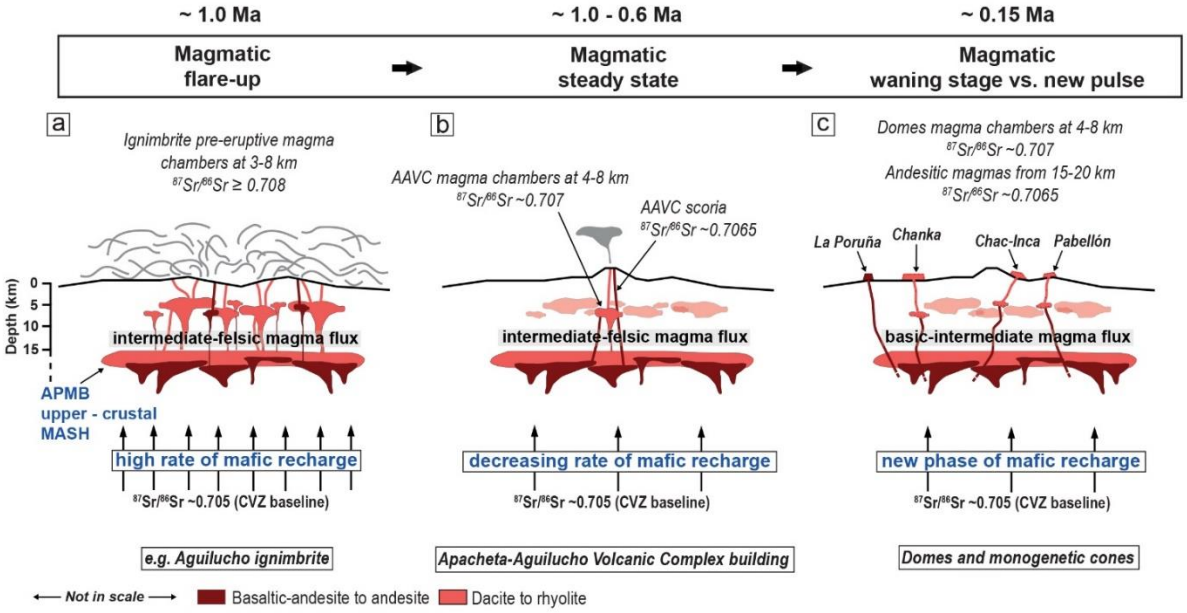

Figure 5.1 *– A schematic model of the magma plumbing system processes in the upper crust at the Altiplano-Puna Volcanic Complex, focussing on the Apacheta-Aguilucho area, through the last ~1.0 Ma. The detailed description of the model is reported in Chapter 2, Paragraph 2.6, Figure 2.14.*

The absence of dated products between 0.6 - 0.1 Ma in the studied area do not allowed to define a univocal, main heat source. Neither the petrological history of the dacitic domes, permitted to constrain their magma chamber as the main thermal engine of the Cerro Pabellón geothermal system. What is undoubted is that the presence of the huge APMB in the upper crust is not negligible and cannot be ruled out as the main heat source of this and other geothermal systems of the APVC.

The magmatic fluids released from the heat source/s during their rise to the surface, started to interact with the host rocks, producing mineralogical, textural and chemical variations of these latter, as a response to the thermal and chemical changes.

Mineralogical studies on the vertical and superficial distribution of the clay minerals forming the active hydrothermal system of the Cerro Pabellón geothermal field, revealed that the system is characterized by both acid-sulfate (fumarolic field) and adularia-sericite (boreholes) alteration types, which represent the two most typical hydrothermal alteration assemblages linked to geothermal systems in active or recent volcanic areas. The acid-sulfate alteration characterizes the upper parts of the Apacheta volcano, where the rising magmatic gases are mixed with shallower aquifer, producing acid-sulfate waters. Here two main subzones were recognized: i) one characterized by high amounts of smectite, mainly coupled with cristobalite and feldspar, and ii) one characterized by kaolinite, mainly coupled with halloysite and subordinate smectite. These subzones show a good correspondence with the thermal manifestations position, and a moderate accordance with the soil temperatures measured in

the sampling locations. Conversely, a not-fitting with the pH conditions of stability for the smectite clay minerals group was observed.

The adularia-sericite alteration characterizes the geothermal reservoir and was possibly linked to fluids with near-neutral pH. Two main clay minerals transitions were detected in the upper parts of the investigated boreholes: the smectite to illite and the smectite to chlorite. The illite and chlorite, only prevail in rock samples from the reservoir domain (i.e. deeper parts of the boreholes), where mixed-layer illite-smectite and chlorite-smectite are almost absent. In both reaction series, a continuous and slow reduction of the proportion of smectite layers in mixed layers with depth, was recognized. The impermeability of the clay cap of the geothermal system, would not favour the advance of illite-smectite and chlorite-smectite reaction series. Thus, the blind nature of the Cerro Pabellón geothermal system might be related to the thickness and very low permeability of the clay cap (~300 m).

The sealing capacity of these clay-cap units was finally investigated through systematic diffuse CO_2 soil flux and temperature measurements, using the accumulation chamber method. The low CO_2 flux and the relatively large areas of thermal anomalies identified, demonstrate the efficiency of the thick clay-cap to prevent the resurgence of fluids up to the surface. Moreover, the efficient magmatic gas scrubbing processes within the liquid-dominated environment of the reservoir produced both the removal of CO_2 and the subsequent heating of the perched shallow aquifer. The thermal behaviour of the aquifer resulted at the surface as a slight and diffused thermal anomaly (recognized by a geostatistical approach) and as a wispy flow of steam with measured temperature of 88 °C at the bottom of the 187 m depth PAE-1 well. The low CO_2 effluxes measured in the main geothermal areas suggest that contribution by deep-seated CO_2 (magmatic origin) to soil degassing is almost negligible. In fact: i) the majority (91.7%) of the soil CO_2 flux measurements are below background levels (i.e. 1.50 $g \cdot m^{-2} \cdot day^{-1}$); ii) most shallow (10 cm) soil temperatures are higher than the temperature condition of air-saturated soil (i.e. ~10 °C); iii) no correlation between soil temperature and CO_2 flux is recorded; and iv) the only significant thermal anomalies is registered at the active fumarolic field. Finally, the decoupling between soil temperature and CO_2 flux, defined that the volcano-tectonic structures did not play a key role in the distribution of the CO_2 flux and temperature at surface, with the active fumarolic area representing the only visible evidence of the blind (or hidden) geothermal reservoir in the Cerro Pabellón area (Fig. 5.2).

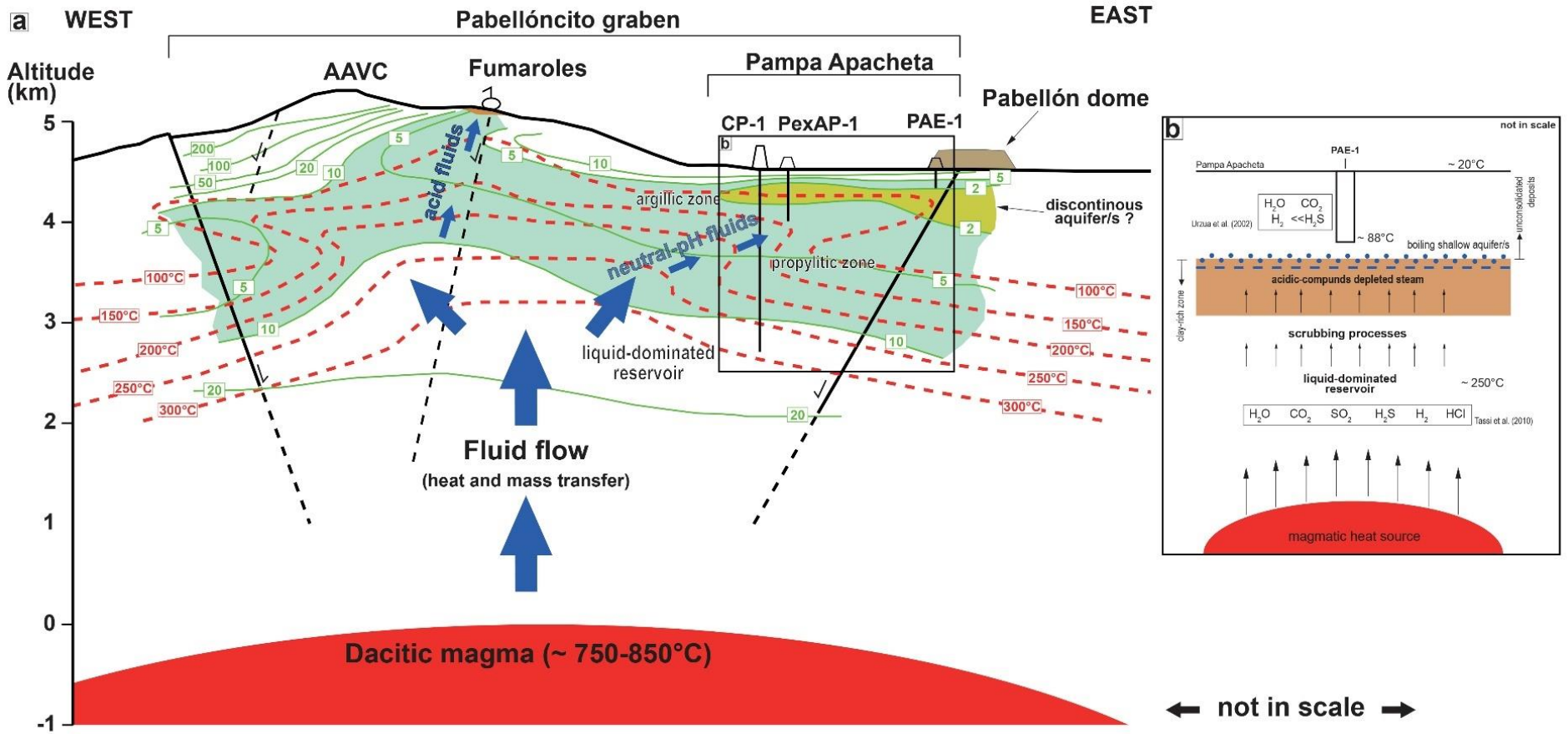
a
WEST
Pabellóncito graben
EAST
Altitude (km)
AAVC
Fumaroles
Pampa Apacheta
Pabellón dome
CP-1
PexAP-1
PAE-1
b
argillic zone
discontinous aquifer/s ?
acid fluids
neutral-pH fluids
propylitic zone
liquid-dominated reservoir
Fluid flow
(heat and mass transfer)
Dacitic magma (~ 750-850°C)
100°C
150°C
200°C
250°C
300°C
not in scale
b
not in scale
PAE-1
Pampa Apacheta
~ 20°C
Urzua et al. (2002)
H2O CO2 H2 <<H2S
~ 88°C
boiling shallow aquifer/s
unconsolidated deposits
acidic-compunds depleted steam
clay-rich zone
scrubbing processes
liquid-dominated reservoir
~ 250°C
H2O CO2 SO2 H2S H2 HCl
Tassi et al. (2010)
magmatic heat source

Figure 5.2 *– Simplified conceptual model for the Cerro Pabellón geothermal field. a) West to east simplified profile of the Cerro Pabellón area showing temperature isotherms, regional water table depth and MT resistivity data (in Ω·m) from Urzua et al. (2002); the 100°C temperature isotherm has been modified taking in account new data of soil temperatures at the fumarolic field. The greenish area represents the clay-rich zone identified in Chapter 3, while the yellowish area represents the possible shallow aquifer identified by Urzua et al. (2002) with MT. The main volcanic and tectonic features are also report. The dacitic magma depth and temperatures are according to Gorini et al. (2018). b) Schematic evolution of rising of the geothermal fluids to the surface. Scrubbing processes characterized the liquid-dominant reservoir, resulting in the lack of acidic compounds at surface; the CO_2-depleted steam can rise in the permeable and unconsolidated deposits heating the perched aquifer. Black rectangles report the main compounds detected by Tassi et al. (2010) and Urzua et al. (2002) in the fumaroles and in the PAE-1 well, respectively.*

5.2. Further works

Many arguments of the Cerro Pabellón geothermal system were deepened during this work, whereas some points still need further investigations.

Some possible starting points for further studies are resumed hereafter.

Chapter 2 focused on the ascent of the different magmas erupted at the AAVC only within the shallower parts of one of the thickest continental crusts of the world (up to 70 km). What is still unknown is the origin of the less differentiated magmas (i.e. basalts-andesites) sporadically found in different sector of this Andean sector (Altiplano-Puna Volcanic Complex). It is not clear if these magmas are directly "produced" by the Altiplano-Puna Magma Body or if they come from the lower crust. A good starting point is to work mainly with petrographic and geochemical composition of primitive mineralogical phases (i.e. pyroxene) from the mafic enclaves and from other similar lavas found near the AAVC area (e.g. La Poruña scoria cone) to determine if they were generated under the same petrological conditions. In fact, they share similar eruption ages (~100 ka), geochemical and isotopic characters. The pyroxene compositions could give the P-T conditions on which these magmas generated and could be more reliable than the olivine. Information given by this latter mineralogical phase would not give useful constraints, because of disequilibrium processes involved during the interaction with a > 70 km thick crust of the mantle-derived magmas. Moreover, deepen the mixing/mingling processes could be useful to clarify the timing of the domes' eruptions, defining how long the two different magmas interacted (without homogenization) before being erupted. Another possible theme that could be developed thanks to the new chronological ages (Sellés and Gardeweg, 2017; Chapter 2), is the calculation of the eruption rates and recharge volumes. In fact, the timing and the evaluation of the volumes erupted can be used to define the rates of eruption in the volcanic complex, giving a summary idea of the heat flux from the magmatic chambers towards the surface, and possibly unravelling the main heat source of the geothermal system.

A critical point emerged in Chapter 3 is that related to the not-fitting conditions of stability of the smectite clay minerals group with the strongly acid conditions characterizing the Apacheta-Aguilucho Volcanic Complex fumarolic field. The involvement of neutralization processes can, at least partially, explain the presence of smectite in such acid environment. Further XRD detailed analyses to distinguish di- and trioctahedral clay minerals, coupled with SEM and FTIR analyses to constrain the morphology of the minerals and the crystallinity index, as well the chemical compositions, could help to understand the physico-chemical processes of the fluid-rocks interaction. Moreover, a detailed study on the fossil alteration zone, located about 600 m North from the fumarolic field, could give insights on the temporal and spatial evolution of the superficial alteration related to the resurgence of hydrothermal fluids. One main objective could be to compare the main characters of the fossil alteration zone with those of the active alteration area (i.e. fumarolic field).
The investigation of the fossil alteration zone is currently under development, in the framework of a collaborative research between the Centro de Excelencia en Geotermia de los Andes (C.E.G.A.) and the University of Urbino.

In Chapter 4, the investigated areas were limited with respect of the whole extension of the geothermal area. The difficulties to cover large portions of the geothermal concession were due: i) to the scarceness of structural lineaments evidences, ii) to the hard-working conditions (i.e. altitude), iii) to the power-plant-related structures and infrastructures work in progress, and iv) to the lack of a soil-cover in several zones, where compact hard lavas cropped out. A critical topic that could be really useful to deepen is that related to the origin of the CO_2 in the interstitial gases. An extensive sampling campaign to determine the $\delta^{13}C$-CO_2 isotopic contents could shed light on the origin of the source/s or geochemical processes affecting the geothermal fluids.

REFERENCES

Acocella, V., Gioncada, A., Omarini, R., Riller, U., Mazzuoli, R., Vezzoli, L., 2011. Tectonomagmatic characteristics of the back-arc portion of the Calama-Olacapato-El Toro Fault Zone, Central Andes. Tectonics, 30, TC3005, pp. 1-19. doi:10.1029/2010TC002854.

AFNOR. 1993. Mesure de la quantité et de l'activité de la fraction argileuse (Norme Française NF P 94-068). Association française de Normalization (ANFOR), La Défense, Paris, France.

Aguilera, F., Ahumada, S., Mercado, J.L., Piscaglia, F., Renzulli, A., Tassi F., 2008. Geological survey, petrology and fluid geochemistry of the Apacheta-Aguilucho Volcanoes (Andean Central Volcanic Zone, Northern Chile) and their geothermal system. XXVII National Conference GNGTS, Trieste, 23 August.

Aguirre, I., Clavero, J., Simmons, S., Giavelli, A., Mayorga, C., Soffia, J., 2011. Colpitas a new geothermal project in Chile. Geothermal Resources Council Transactions, 35, 1141-1145, California.

Ahumada, S., Mercado, J.L., 2009. Evolución geológica y estructural del complejo volcánico Apacheta-Aguilucho (CVAA), Segunda Región, Chile. Dissertation, Bachelor's Degree Thesis, Universidad Católica del Norte. Chile, Antofagasta.

Aitcheson, S.J., Harmon, R.S., Moorbath, S., Schneider, A., Soler, P., Soria-Escalante, E., Steele, G., Swainbank, I., Wörner, G., 1995. Pb isotopes define basement domains of the Altiplano, central Andes. Geology, 23 (6), pp. 555-558. https://doi.org/10.1130/0091-7613(1995)023<0555:PIDBDO>2.3.CO;2.

Amram, K., Ganor, J., 2005. The combined effect of pH and temperature on smectite dissolution rate under acidic conditions. Geochimica et Cosmochimica Acta, vol. 69 (10), pp. 2535-2546. doi:10.1016/j.gca.2004.10.001.

Annen, C., Blundy, J.D., Leuthold, J., Sparks, R.S.J., 2015. Construction and evolution of igneous bodies: Towards an integrated perspective of crustal magmatism. Lithos, 230, pp. 206-221. https://doi.org/10.1016/j.lithos.2015.05.008.

Annunziatellis, A., Beaubien, S.E., Bigi, S., Ciotoli, G., Coltella, M., Lombardi, S., 2008. Gas migration along fault systems and through the vadose zone in the Latera caldera (central Italy): Implications for CO_2 geological storage. International Journal of Greenhouse Gas Control, 2, pp. 353-372. doi:10.1016/j.ijggc.2008.02.003.

Aravena, D., Muñoz, M., Morata, D., Lahsen, A., Parada, M.A., Dobson, P., 2016. Assessment of high enthalpy geothermal resources and promising areas of Chile. Geothermics 59, 1–13. http://dx.doi.org/10.1016/j.geothermics.2015.09.001.

Aubert, M., Baubron, J.C., 1988. Identification of a hidden thermal fissure in a volcanic terrain using a combination of hydrothermal convection indicators and soil-atmosphere analysis. Journal of Volcanology and Geothermal Resources, 35, pp. 217-225. https://doi.org/10.1016/0377-0273(88)90018-2.

Azua-Bustos, A., Urrejola, C., Vicuña, R., 2012. Life at the dry edge: Microorganisms of the Atacama Desert. Federation of European Biochemical Societies Letters, 586, pp. 2939-2945. http://dx.doi.org/10.1016/j.febslet.2012.07.025.

Bacon, C.R., 1986. Magmatic inclusions in silicic and intermediate volcanic rocks. Journal of Geophysical Research, 91, pp. 6091-6112. https://doi.org/10.1029/JB091iB06p06091.

Balić-Žunić, T., Garavelli, A., Jakobsson, S.P., Jonasson, K., Katerinopoulos, A., Kyriakopoulos, K., Acquafredda, P., 2016. Fumarolic Minerals: An Overview of Active

European Volcanoes. Chapter 11 from “Updates in Volcanology - From Volcano Modelling to Volcano Geology”, Dr. Karoly Nemeth (Ed.), InTech, DOI: 10.5772/64129.

Barazangi, M., Isacks, B.L., 1976. Spatial distribution of earthquakes and subduction of the Nazca plate beneath South America. Geology, 4, 41-47.

Bauluz, B., Peacor, D.R., Ylagan, R.F., 2002. Transmission electron microscopy study of smectite illitization during hydrothermal alteration of a rhyolitic hyaloclastite from Ponza, Italy. Clays and Clay Minerals, 50 (2), pp. 157-173.

Beaufort, D., Baronnet, A., Lanson, B., Meunier, A., 1997. Corrensite: A single phase or a mixed-layer phyllosilicate in the saponite-to-chlorite conversion series? A case study of Sancerre-Couy deep drill hole (France). American Mineralogist, 82, pp. 109-124.

Beck, S.L., Zandt, G., Myers, S.C., Wallace, T.C., Silver, P.G., Drake, L., 1996. Crustal-thickness variations in the central Andes. Geology, 24 (5), pp. 407-410. https://doi.org/10.1130/0091-7613(1996)024<0407:CTVITC>2.3.CO;2.

Bertani, R., 2015. Geothermal Power Generation in the World, 2010-2014 Update Report. Proceedings World Geothermal Congress 2015. Melbourne, Australia, 19-25 April 2015.

Bertin, D., Amigo, A., 2015. Geología y peligros del Volcán San Pedro, II Region. In: Actas XIV Congreso Geológico Chileno, La Serena, Chile, vol. 3. pp. 128–131.

Biscaye, P.E., 1965. Mineralogy and sedimentation of Recent Deep-Sea Clay in the Atlantic Ocean and Adjacent Sea and Oceans. Geological Society of America Bulletin, 76, pp. 803-832.

Blum-Oeste, M., Wörner, G., 2016. Central Andean magmatism can be constrained by three ubiquitous end-members. Terra Nova 28 (6), pp. 434-440. http://dx.doi.org/10.1111/ter.12237.

Bona, P., Coviello, M., 2016. Valoración y gobernanza de los proyectos geotérmicos en América del Sur: una propuesta metodológica. Comisión Económica para América Latina y el Caribe (CEPAL), Copyright © United Nations; pp. 178.

Brandmeier, M., Wörner, G., 2016. Compositional variations of ignimbrite magmatism in the Central Andes over the past 26 Ma - a multivariate statistical perspective. Lithos 262, pp. 713-728. http://dx.doi.org/10.1016/j.lithos.2016.07.011.

Brasse, H., Lezaeta, P., Rath, V., Schwalenberg, K., Soyer, W., Haak, V., 2002. The Bolivian Altiplano conductivity anomaly. Journal of Geophysical Research, 107, 2096. DOI: 10.1029/2001JB000391.

Burgisser, A., Bergantz, G.W., 2011. A rapid mechanism to remobilize and homogenize highly crystalline magma bodies. Nature 471, pp. 212-215. https://doi.org/10.1038/nature09799.

Burns, D.H., de Silva, S.L., Tepley III, F., Schmitt, A.K., Loewen, M.W., 2015. Recording the transition from flare-up to steady-state arc magmatism at the Purico–Chascon volcanic complex, northern Chile. Earth and Planetary Science Letters 422, pp. 75–86. doi:10.1016/j.epsl.2015.04.002.

Cannata, A., Giudice, G., Gurrieri, S., Montalto, P., Alparone, S., Di Grazia, G., Favara, R., Gresta, S., Liuzzo, M., 2010. Relationship between soil CO_2 flux and volcanic tremor at Mt. Etna: Implications for magma dynamics. Environmental Earth Sciences, 61, 3, pp. 477-489. DOI 10.1007/s12665-009-0359-z.

Carapezza, M.L., Ranaldi, M., Gattuso, A., Pagliuca, N.M., Tarchini, L., 2015. The sealing capacity of the cap rock above the Torre Alfina geothermal reservoir (Central Italy) revealed by soil CO_2 flux investigations. Journal of Volcanology and Geothermal Resources, 291, pp. 25-34. http://dx.doi.org/10.1016/j.jvolgeores.2014.12.011.

Cardellini, C., Chiodini, G., Frondini, F., 2003. Application of stochastic simulation to CO_2 flux from soil: Mapping and quantification of gas release. Journal of Geophysical Research, 108, B9, pp. 2425. http://dx.doi.org/10.1029/2002JB002165.

Chamorro, C. R., Mondéjar, M. E., Ramos, R., Segovia, J. J., Martín, M. C. Villamañán, M. A., 2012. World geothermal power production status: Energy, environmental and economic study of high enthalpy technologies. Energy, 42, 1, pp. 10-18.

Charrier, R., Pinto, L., Rodríguez, M.P., 2007. Tectonostratigraphic evolution of the Andean Orogen in Chile. Pp. 21-114 in: The Geology of Chile (T. Moreno and W. Gibbons, editors). 'Geology of Series', Geological Society London.

Chernicoff, C.J., Richards, J.P., Zappettini, E.O., 2002. Crustal lineament control on magmatism and mineralization in northwestern Argentina: geological, geophysical, and remote sensing evidence. Ore Geology Reviews, 21, pp. 127-155.

Chiodini, G., Cioni, R., Guidi, M., Raco, B., Marini, L., 1998. Soil CO_2 flux measurements in volcanic and geothermal areas. Applied Geochemistry, 13, 5, pp. 543-552. https://doi.org/10.1016/S0883-2927(97)00076-0.

Chiodini, G., Frondini, F., Cardellini, C., Granieri, D., Marini, L., Ventura, G., 2001. CO_2 degassing and energy release at Solfatara volcano, Campi Flegrei, Italy. Journal of Geophysical Research, 105, B8, pp. 16213-16221. https://doi.org/10.1029/2001JB000246.

Chiodini, G., Granieri, D., Avino, R., Caliro, S., Costa, A., Werner, C., 2005. Carbon dioxide diffuse degassing and estimation of heat release from volcanic and hydrothermal systems. Journal of Geophysical Research, 110, B08204. http://dx.doi.org/10.1029/2004JB003542.

Chiodini, G., Caliro, S., Cardellini, C., Avino, R., Granieri, D., Schmidt, A., 2008. Carbon isotopic composition of soil CO_2 efflux, a powerful method to discriminate different sources feeding soil CO_2 degassing in volcanic-hydrothermal areas. Earth and Planetary Science Letters, 274, pp. 372-379. doi:10.1016/j.epsl.2008.07.051.

Chiodini, G., Cardellini, C., Lamberti, M.C., Agusto, M., Caselli, A., Liccioli, C., Tamburello, G., Tassi, F., Vaselli, O., Caliro, S., 2015. Carbon dioxide diffuse emission and thermal energy release from hydrothermal systems at Copahue-Caviahue Volcanic Complex (Argentina). Journal of Volcanology and Geothermal Research 304, pp. 294-303. http://dx.doi.org/10.1016/j.jvolgeores.2015.09.007.

Chmielowski, J., Zandt, G., Haberland, C., 1999. The Central Andean Altiplano-Puna magma body. Geophysical Research Letters 26, pp. 783-786. https://doi.org/10.1029/1999GL900078.

Christenson, B.W., Mroczek, E.K., Kennedy, B.M., van Soest, M.C., Stewart, M.K., Lyon, G., 2002. Ohaaki reservoir chemistry: characteristics of an arc-type hydrothermal system in the Taupo Volcanic Zone, New Zealand. Journal of Volcanology and Geothermal Resources, 115, pp. 53-82. https://doi.org/10.1016/S0377-0273(01)00309-2.

Clavero, J., Pineda, G., Mayorga, C., Giavelli, A., Aguirre, I., Simmons, S., Martini, S., Soffia, J., Arriaza, R., Polanco, E., Achurra, L., 2011. Geological, geochemical, geophysical and first drilling data from Tinguiririca geothermal area, central Chile. Geothermal Resources Council Transactions, 35, pp. 731-734.

Comeau, M.J., Unsworth, M.J., Cordell, D., 2016. New constraints on the magma distribution and composition beneath Volcán Uturuncu and the southern Bolivian Altiplano from magnetotelluric data. Geosphere 12, pp. 1391-1421. https://doi.org/10.1130/GES01277.1.

Comeau, M.J., Unsworth, M.J., Ticona, F., Sunagua, M., 2015. Magnetotelluric images of magma distribution beneath Volcán Uturuncu, Bolivia: Implications for magma dynamics. Geology 43, pp. 243-246. https://doi.org/10.1130/G36258.1.

Coombs, M.L., Eichelberger, J.C., Rutherford, M.J., 2002. Experimental and textural constraints on mafic enclave formation in volcanic rocks. Journal of Volcanology and Geothermal Research 119, pp. 125-144. https://doi.org/10.1016/S0377-0273(02)00309-8.

Corrado, S., Aldega, L., Celano, A.S., de Benedetti, A.A., Giordano, G., 2014. Cap rock efficiency and fluid circulation of natural hydrothermal systems by means of XRD on clay minerals (Sutri, northern Latium, Italy). Geothermics, 50, pp. 180-188. http://dx.doi.org/10.1016/j.geothermics.2013.09.011.

Cusicanqui, H., 1978a. Geochemical monitoring of wells 12 and 13 at El Tatio. Unpublished Report, Committee for geothermal energy resources (CORFO), 8 pp. (in Spanish).

Cusicanqui, H., 1978b. Control geoquimico de los pozos 7, 10 y 11 de El Tatio y estudio geoquimico de los pozos 2, 3, 4, y 5 del campo geotermal de Puchuldiza. Unpublished Report, Committee for geothermal energy resources (CORFO), 8 pp. (in Spanish).

Cusicanqui, H., 1979. Geochemical Study of the Suriri Thermal Area, Arica Province, 1st Region - Estudio Geoquímico del área Termal de Suriri, Provincia de Arica, I Región. Unpublished Report; Committee for Geothermal Energy Resources (CORFO): Santiago, Chile, 1979; p. 29. (In Spanish).

Davidson, J., Harmon, R.S.H., Wörner, G., 1991. The source of Central Andean magmas; some considerations. In: Harmon, Rapela (Eds.), Andean Magmatism and its Tectonic Setting, Geological Society of America Special Publication 265, pp. 233-243. https://doi.org/10.1130/SPE265-p233.

Davidson, J.P., de Silva, S.L., 1992. Volcanic rocks from the Bolivian Altiplano: insights into crustal structure, contamination, and magma genesis in the central Andes. Geology 20 (12), pp. 1127-1130. https://doi.org/10.1130/0091-7613(1992)020<1127:VRFTBA>2.3.CO;2.

Davidson, J.P., Turner, S., Handley, H., Macpherson, C., Dosseto, A., 2007. Amphibole “sponge” in arc crust?. Geology 35 (9), pp. 787-790. https://doi.org/10.1130/G23637A.1.

Day-Stirrat, R.J., Dutton, S.P., Milliken, K.L., Loucks, R.G., Aplin, A.C., Hillier, S., Van der Pluijm, B.A., 2010. Fabric anisotropy induced by primary depositional variations in the silt: clay ratio in two fine-grained slope fan complexes: Texas Gulf Coast and northern North Sea. Sedimentary Geology, 226, pp. 42-53.

de Silva, S.L., 1989. Altiplano-Puna volcanic complex of the central Andes. Geology 17 (12), pp. 1102-1106.

de Silva, S.L., Francis, P.W., 1991. Volcanoes of the Central Andes. Springer-Verlag, Berlin Heidelberg, pp. 216. https://doi.org/10.1017/S0016756800008372.

de Silva, S.L., Gosnold, W.D., 2007. Episodic construction of batholiths: Insights from the spatiotemporal development of an ignimbrite flare-up. Journal of Volcanology and Geothermal Research 167, pp. 320-335. doi:10.1016/j.jvolgeores.2007.07.015

de Silva, S.L., Gregg, P.M., 2014. Thermomechanical feedbacks in magmatic systems: Implications for growth, longevity, and evolution of large caldera-forming magma reservoirs

and their supereruptions. Journal of Volcanology and Geothermal Research 282, pp. 77–91. http://dx.doi.org/10.1016/j.jvolgeores.2014.06.001.

de Silva, S.L., Key, S.M., 2018. Turning up the Heat: High-Flux Magmatism in the Central Andes. Elements 14, pp. 245-250. doi:10.2138/gselements.14.4.245.

de Silva, S.L., Riggs, N.R., Barth A.P., 2015. Quickening the Pulse: Fractal Tempos in Continental Arc Magmatism. Elements 11, pp. 113-118. doi:10.2113/gselements.11.2.113

de Silva, S.L., Self, S., Francis, P.W., Drake, R.E., Ramírez, C., 1994. Effusive silicic volcanism in the Central Andes: the Chao dacite and other young lavas of the Altiplano-Puna volcanic complex. Journal of Geophysical Research 99 (B9), pp. 17805-17825. https://doi.org/10.1029/94JB00652.

de Silva, S.L., Zandt, G., Trumbull, R., Viramonte, J., Salas, G., Jimenez, N., 2006. Large ignimbrite eruptions and volcano-tectonic depressions in the Central Andes: a termomechanical perspective. Geological Society, London, Special Publications, 269, pp. 47-63. https://doi.org/10.1144/GSL.SP.2006.269.01.04.

del Potro, R., Díez, M., Blundy, J., Camacho, A.G., Gottsmann, J., 2013. Diapiric ascent of silicic magma beneath the Bolivian Altiplano. Geophysical Research Letters 40, pp. 2044-2048. https://doi.org/10.1002/grl.50493.

DePaolo, D.J., 1981. Trace element and isotopic effects of combined wallrock assimilation and fractional crystallization. Earth and Planetary Science Letters 53 (2), pp. 189-202. http://dx.doi.org/10.1016/0012-821X(81)90153-9.

Eichelberger, J.C., 1980. Vesiculation of mafic magma during replenishment of silicic magma reservoirs. Nature, 288, pp. 446-450. https://doi.org/10.1038/288446a0.

ELC-Electroconsult, 1980. Geothermal field of El Tatio: evaluation of the geothermal potential. Unpublished Report, Committee for geothermal energy resources (CORFO), 13 pp. (in Spanish).

Elío, J., Ortega, M.F., Nisi, B., Mazadiego, L.F., Vaselli, O., Caballero, J., Chacón, E., 2016. A multi-statistical approach for estimating the total output of CO_2 from diffuse soil degassing by the accumulation chamber method. International Journal of Greenhouse Gas Control, 47, pp. 351-363. http://dx.doi.org/10.1016/j.ijggc.2016.02.012.

ENEL, 2012. Cerro Pabellón Geothermal Project (Apacheta), Technical Report Enel, Latinoamérica (Chile) Ltda.

Farías, M., Charrier, R., Comte, D., Martinod, J., Hérail, G., 2005. Late Cenozoic deformation and uplift of the western flank of the Altiplano: Evidence from the depositional, tectonic, and geomorphologic evolution and shallow seismic activity (northern Chile at 19 30′S). Tectonics, 24, pp. 1-27.

Faulds, J.E., Hinz, N.H., 2015. Favorable Tectonic and Structural Settings of Geothermal Systems in the Great Basin Region, Western USA: Proxies for Discovering Blind Geothermal Systems. In: Proceedings of World Geothermal Congress 2015, Melbourne, Australia, 19-25 April.

Feeley, T.C., Davidson, J.P., 1994. Petrology of calc-alkaline lavas at Volcán Ollagüe and the origin of compositional diversity at Central Andean stratovolcanoes. Journal of Petrology 35 (5), pp. 1295-1340. http://dx.doi.org/10.1093/petrology/35.5.1295.

Francis, P.W., Rundle, C.C., 1976. Rates of production of the main magma types in the central Andes. Geological Society of America Bulletin 3, pp. 474-480. doi:10.1130/0016-7606(1976)87<474:ROPOTM>2.0.CO;2.

Freymuth, H., Brandmeier, M., Wörner, G., 2015. The origin and crust/mantle mass balance of Central Andean ignimbrite magmatism constrained by oxygen and strontium isotopes and erupted volumes. Contributions to Mineralogy and Petrology 169 (6), pp. 1-24. http://dx.doi.org/10.1007/s00410-015-1152-5.

Fridriksson, T., Bjarni Reyr, K., Halldór, A., Eygerður, M., Snjólaug, Ó., Chiodini, G., 2006. CO_2 emissions and heat flow through soil, fumaroles, and steam heated mud pools at the Reykjanes geothermal area, SW Iceland. Applied Geochemistry, 21, 9, pp. 1551-1569. https://doi.org/10.1016/j.apgeochem.2006.04.006.

Fulignati, P., Gioncada, A., Sbrana, A., 1998. Geological model of magmatic-hydrothermal system of Vulcano (Aeolian Islands, Italy). Mineralogy and Petrology, 62 (3-4), pp. 195-222. https://doi.org/10.1007/BF01178029.

Garcia-Estrada, G.H., López-Hernández, A., Prol, L.R.M., 2002. Conductive thermal modeling to estimate the age of the heat source at the Los Azufres field, Mexico. Geothermal Resources Council Transactions 26, 22–25.

Giammanco, S., Melián, G., Neri, M., Hernández, P.A., Sortino, F., Barrancos, J., López, M., Pecoraino, G., Perez, N.M., 2016. Active tectonic features and structural dynamics of the summit area of Mt. Etna (Italy) revealed by soil CO_2 and soil temperature surveying. Journal of Volcanology and Geothermal Research, 311, pp. 79-98. https://doi.org/10.1016/j.jvolgeores.2016.01.004.

Giordano, G. Pinton, A., Cianfarra, P., Baez, W., Chiodi, A., Viramonte, J., Norini, G., Groppelli, G., 2013. Structural control on geothermal circulation in the Cerro Tuzgle–Tocomar geothermal volcanic area (Puna plateau, Argentina). Journal of Volcanology and Geothermal Research, 249, pp. 77-94. http://dx.doi.org/10.1016/j.jvolgeores.2012.09.009.

Godoy, B., Wörner, G., Kojima, S., Aguilera, F., Simon, K., Hartmann, G., 2014. Low-pressure evolution of arc magmas in thickened crust: the San Pedro-Linzor volcanic chain, Central Andes, Northern Chile. Journal of South American Earth Sciences 52, pp. 24-42. http://dx.doi.org/10.1016/j.jsames.2014.02.004.

Godoy, B., Wörner, G., Le Roux, P., de Silva, S., Parada, 838 M.A., Kojima, S., González-Maurel, O., Morata, D., Polanco, E., Martínez, P., 2017a. Sr- and Nd isotope variations along the Pleistocene San Pedro-Linzor volcanic chain, N. Chile: Tracking the influence of the upper crustal Altiplano-Puna Magma Body. Journal of Volcanology and Geothermal Research 341, pp. 172-186. doi:843 10.1016/j.jvolgeores.2017.05.030

Godoy, B., Rodríguez, I., Pizarro, M., Rivera, G., 2017b. Geomorphology, lithofacies, and block characteristics to determine the origin, and mobility, of a debris avalanche deposit at Apacheta-Aguilucho Volcanic Complex (AAVC), northern Chile. Journal of Volcanology and Geothermal Research, 347, pp. 136-148. doi:10.1016/j.jvolgeores.2017.09.008.

González, G., Cembrano, J., Carrizo, D., Macci, A., Schneider, H., 2003. The link between forearc tectonics and Pliocene-Quaternary deformation of the Coastal cordillera, northern Chile. Journal of South American Earth Sciences, 16, pp. 321-342.

Gorini, A., 2017. Heat source and reservoir of geothermal areas in Latin America as inferred from thermobarometry of amphibole-bearing extrusives and fluid geochemistry: examples from Chile and Ecuador. PhD thesis, University of Urbino, pp. 106.

Gorini, A., Ridolfi, F., Piscaglia, F., Taussi, M., Renzulli, A., 2018. Application and reliability of calcic amphibole thermobarometry as inferred from calc-alkaline products of active geothermal areas in the Andes. Journal of Volcanology and Geothermal Research 358, pp. 58-76. https://doi.org/10.1016/j.jvolgeores.2018.03.018.

Gottsmann, J., Blundy, J., Henderson, S., Pritchard, M., Sparks, S., 2017. Thermomechanical modeling of the Altiplano-Puna deformation anomaly: Multiparameter insights into magma mush reorganization. Geosphere 13 (4), pp. 1042-1065. DOI: 10.1130/GES01420.1.

Götze, H.J., Krause, S., 2002. The Central Andean gravity high, a relic of an old subduction complex? Journal of South American Earth Sciences, 14, pp. 799-811. https://doi.org/10.1016/S0895-9811(01)00077-3.

Götze, H.J., Lahmeyer, B., Schmidt, S., Strunk, S., 1994. The lithospheric structure of the Central Andes (20°–26°S) as inferred from quantitative interpretation of regional gravity. In: Reutter, Scheuber, Wigger (eds) Tectonics of the Southern Central Andes. Springer, Heidelberg, pp. 7-21. https://doi.org/10.1007/978-3-642-77353-2_1.

Grocke, S.B., de Silva, S.L., Iriarte, R., Lindsay, J.M., Cottrell, E., 2017. Catastrophic caldera-forming (CCF) monotonous silicic magma reservoirs: geochemical and petrological constraints on heterogeneity, magma dynamics, and eruption dynamics of the 3.49 Ma Tara Supereruption, Guacha II Caldera, SW Bolivia. Journal of Petrology, 58, pp. 227-260. https://doi.org/10.1093/petrology/egx012.

Guisseau, D., Patrier-Mas, P., Beaufort, D., Girard, J.P., Inoue, A., Sanjuan, B., Petit, S., Lens, A., Genter, A., 2007. Significance of the depth-related transition montmorillonite-beidellite in the Bouillante geothermal field (Guadeloupe, Lesser Antilles). American Mineralogist, 92, pp. 1800-1813.

Hanson, M.C., Oze, C., Horton, T.W., 2014. Identifying blind geothermal systems with soil CO_2 surveys. Applied Geochemistry, 50, pp. 106-114. http://dx.doi.org/10.1016/j.apgeochem.2014.08.009.

Hauser, A., 1997. Register and characterization of mineral and thermal springs of Chile, 50. Servicio Nacional de Geología y Minería, Santiago, Chile, p. 90 (in Spanish).

Hawkesworth, C.J., Hammill, M., Gledhill, A.R., van Calsteren, P., Rogers, G., 1982. Isotope and trace element evidence for late-stage intra-crustal melting in the High Andes. Earth and Planetary Science Letters, 58, pp. 240-254. https://doi.org/10.1016/0012-821X(82)90197-2.

Heald, P., Foley, N.K., Hayba, D.O., 1987. Comparative anatomy of volcanic-hosted epithermal deposits: acid-sulfate and adularia-sericite types. Economic geology, 82 (1), pp. 1-26. https://doi.org/10.2113/gsecongeo.82.1.1.

Henley, R.W., Ellis, A.J., 1983. Geothermal systems ancient and modern: a geochemical review. Earth Science Reviews, 19 (1), pp. 1-50. DOI: 10.1016/0012-8252(83)90075-2.

Herrera, S., Pinto, L., Deckart, K., Cortés, J., Valenzuela, I., 2017. Cenozoic tectonostratigraphic evolution and architecture of the Central Andes in northern Chile based on the Aquine region, Western Cordillera (19-19°30' S). Andean Geology, 44, pp. 87-122.

Hickson, C.J., Ferraris, F., Rodriguez, C., Sielfeld, G., Henriquez, R., Gislason, T., Selters, J., Benoit, D., White, P., Southon, J., Ussher, G., Charroy, J., Smith, A., Lovelock, B., Lawless, J., Quinlivan, P., Smith, L., Yehia, R., 2011. The Mariposa geothermal system, Chile. Geothermal Resources Council Transactions, v. 35, pp. 817-825.

Hildreth, W., Moorbath, S., 1988. Crustal contributions to arc magmatism in the Andes of Central Chile. Contributions to Mineralogy and Petrology 98 (4), pp. 455-489. doi:10.1007/BF00372365.

Hochstein, M.P., 1971. Geophysical survey of the Puchuldiza geothermal area results up to December 1970, Survey for geothermal development in northern Chile. Unpublished Report UN, 22 pp.

Hoefs, J., 1997. Stable Isotope Geochemistry. 3rd Edition. Springer-Verlag, Berlin. https://doi.org/10.1007/978-3-662-03377-7.

IGA Geothermal Energy Database, 2015. Website: https://www.geothermal-energy.org/explore/our-databases/geothermal-power-database-old/#electricity_generation.

Inguaggiato, C., Vita, F., Diliberto, I.S., Calderone, L., 2017. The role of the aquifer in soil CO_2 degassing in volcanic peripheral areas: A case study of Stromboli Island (Italy). Chemical Geology, 469, pp. 110-116. http://dx.doi.org/10.1016/j.chemgeo.2016.12.017.

Inoue, A., 1995. Formation of clay minerals in hydrothermal environments. Pp. 268-329 in: Origin and Mineralogy of Clays (B. Velde, editor). Springer, Berlin, Heidelberg.

Inoue, A., Meunier, A., Beaufort, D., 2004. Illite-smectite mixed-layer minerals in felsic voclaniclastic rocks from drill cores, Kakkonda, Japan. Clays and Clay Minerals, 52, pp. 66-84.

Inoué, S., Kogure, T., 2016. High-angle annular dark field scanning transmission electron microscopic (HAADF- STEM) study of Fe-rich 7 Å–14 Å interstratified minerals from a hydrothermal deposit. Clay Minerals, 51, pp. 603-613.

Irvine, T.N., Baragar, W.R.A., 1971. A guide to the chemical classification of the common volcanic rocks. Canadian Journal of Earth Sciences 8 (5), pp. 523-548. http://dx.doi.org/10.1139/e71-055.

Japan International Cooperation Agency (JICA), 1979. Geothermal power development project in Puchuldiza area. Unpublished Report, 109 pp.

Japan International Cooperation Agency (JICA), 1981. Report on geothermal power development project in Puchuldiza area. Unpublished Report, 48 pp.

Kay, S.M., Coira, B.L., Caffe, P.J., Chen, C.-H., 2010. Regional chemical diversity, crustal and mantle sources and evolution of central Andean Puna plateau ignimbrites. Journal of Volcanology and Geothermal Research 198 (1–2), pp. 81-111. http://dx.doi.org/10.1016/j.jvolgeores.2010.08.013.

Kay, S.M., Mpodozis, C., Coira, B., 1999. Neogene magmatism, tectonism, and mineral deposits of the Central Andes (22° to 33°S Latitude). In: Skinner, B.J. (Ed.), Geology and Ore Deposits of the Central Andes, Society of Economic Geology, Special Publication, vol. 7, pp. 27-59.

Kern, J.M., de Silva, S.L., Schmitt, A.K., Kaiser, J.F., Iriarte, A.R., Economos, R., 2016. Geochronological imaging of an episodically constructed subvolcanic batholith: U-Pb in zircon chronochemistry of the Altiplano-Puna Volcanic Complex of the Central Andes. Geosphere 12 (4), pp. 1-24. http://dx.doi.org/10.1130/GES01258.1.

Lagat, J., 2010. Hydrothermal alteration mineralogy in geothermal fields with case examples from Olkaria domes geothermal field, Kenya. Presented at Short Course V on Exploration for Geothermal Resources. Organized by UNU-GTP, GDC and KenGen, at Lake Naivasha, Kenya, pp. 1-24.

Lahsen, A., 1969 Geology of the area between El Tatio and Cerros de Ayquina. Unpublished Report, Committee for geothermal energy resources (CORFO), 75 pp. (in Spanish).

Lahsen, A., 1976. Geothermal exploration in northern Chile – Summary. In: Circum-Pacific Energy and Mineral Resources, M.T. Halbouty, J.C. Maher, and H.M. Lian, eds., American Association of Petroleum Geologists Memoir 25, pp. 169-175.

Lahsen, A., 1988. Chilean geothermal resources and their possible utilization. Geothermics, 17, pp. 401-410.

Lahsen, A., Muñoz, N., and Parada, M.A., 2010. Geothermal development in Chile. Proceedings, World Geothermal Congress 2010, Bali, Indonesia, 25-29 April, 2010, 7 pp.

Lahsen, A., Rojas, J., Morata, D., Aravena, D. 2015. Geothermal exploration in Chile: Country Update. In Proceedings of the world geothermal congress, Melbourne, Australia (19-25 April 2015).

Lahsen, A., Sepúlveda, F., Rojas, J., and Palacios, C., 2005. Present status of geothermal exploration in Chile. Proceedings, World Geothermal Congress 2005, Antalya, Turkey, 24-25 April 2005, 9 pp.

Lahsen, A., Trujillo, P., 1975. El Tatio geothermal field. Proceedings of the Second United Nations Symposium on the Development and Use of Geothermal Resources, pp. 157-178.

Le Bas, M.J., Le Maitre, R.W., Streckeisen, A., Zanettin, B., 1986. A Chemical Classification of Volcanic Rocks Based on the Total Alkali-Silica Diagram. Journal of Petrology 27 (3), pp. 745-750. https://doi.org/10.1093/petrology/27.3.745.

Lesher, C.E., 1990. Decoupling of chemical and isotopic exchange during magma mixing. Nature 344, pp. 235-237. https://doi.org/10.1038/344235a0.

Lilliefors, H.W., 1967. On the Kolmogorov-Smirnov Test for Normality with Mean and Variance Unknown. Journal of the American Statistical Association, 62, pp. 399-404. DOI: 10.1080/01621459.1967.10482916.

Lindsay, J.M. Schmitt, A.K., Trumbull, R.B., de Silva, S.L., Siebel, W., Emmermann, R., 2001. Magmatic evolution of the La Pacana Caldera system. Central Andes, Chile: compositional variation of two cogenetic, large-volume felsic ignimbrites. Journal of Petrology, 42 (3), pp. 459-486. doi:10.1093/petrology/42.3.459.

Lowell, R.P., Kolandaivelu, K., Rona, P.A., 2014. Hydrothermal activity. Reference Module in Earth Systems and Environmental Sciences, Elsevier, 2014. 18-July-14 doi: 10.1016/B978-0-12-409548-9.09132-6.

Lucassen, F., Becchio, R., Harmon, R., Kasemann, S., Franz, G., Trumbull, R., Wilke, H.-G., Romer, R.L., Dulski, P., 2001. Composition and density model of the continental crust at an active continental margin – the Central Andes between 21° and 27°S. Tectonophysics 341 (1–4), pp. 195-223. http://dx.doi.org/10.1016/S0040-1951(01)00188-3.

Macpherson, C.G., Dreher, S.T., Thirlwall, M.F., 2006. Adakites without slab melting: High pressure differentiation of island arc magma, Mindanao, the Philippines. Earth and Planetary Science Letters 243, pp. 581-593. doi:10.1016/j.epsl.2005.12.034.

Maffucci, R., Corrado, S., Aldega, L., Bigi, S., Chiodi, A., Di Paolo, L., Invernizzi, C., 2016. Cap rock efficiency of geothermal systems in fold-and-thrust belts: Evidence from paleo-thermal and structural analyses in Rosario de La Frontera geothermal area (NW Argentina). Journal of Volcanology and Geothermal Research, 328, pp. 84-95.

Mahon, W., 1974. The geochemistry of the El Tatio geothermal System, survey for geothermal development in northern Chile. Unpublished Report, UN, 109 pp.

Mamani, M., Tassara, A., Wörner, G., 2008. Composition and structural control of crustal domains in the Central Andes. Geochemistry, Geophysics, Geosystems 9 (3), pp. 13 https://doi.org/10.1029/2007GC001925.

Mamani, M., Wörner, G., Sempere, T., 2010. Geochemical variations in igneous rocks of the Central Andean orocline (13°S to 18°S): tracking crustal thickening and magma generation through time and space. Geological Society of America Bulletin 122 (1-2), pp. 162-182. https://doi.org/10.1130/B26538.1.

Marinoviç, N., Lahsen, A., 1984. Carta geológica de Chile No. 58: Hoja Calama, Región de Antofagasta.

Maro, G., Caffe, P.J., Romer, R.L., Trumbull, R.B., 2017. Neogene mafic magmatism in the northern Puna Plateau, Argentina: generation and evolution of a back-arc volcanic suite. Journal of Petrology 58 (8), pp. 1591-1618. doi:10.1093/petrology/egx066..

Marrett, R.A., Allmendinger, R.W., Alonso, R.N., Drake, R.E., 1994. Late Cenozoic tectonic evolution of the Puna Plateau and adjacent foreland, northwestern Argentine Andes. Journal of South American Earth Sciences, 7 (2), pp. 179-207. https://doi.org/10.1016/0895-9811(94)90007-8.

Mason, E., Edmonds, M., Turchyn, A.V., 2017. Remobilization of crustal carbon may dominate volcanic arc emissions. Science, 357 (6348), pp. 290-294. DOI: 10.1126/science.aan5049.

Matthews, S.J., Jones, A.P., Gardeweg, M.C., 1994. Lascar volcano, northern Chile: evidence for steady-state disequilibrium. Journal of Petrology 35 (2), pp. 401-432. https://doi.org/10.1093/petrology/35.2.401.

Mattioli, M., Renzulli, A., Menna, M., Holm, P.M., 2006. Rapid ascent and contamination of magmas through the thick crust of the CVZ (Andes, Ollagüe region): Evidence from a nearly aphyric high-K andesite with skeletal olivines. Journal of Volcanology and Geothermal Research 158 (1-2), pp. 87-105. doi:10.1016/j.jvolgeores.2006.04.019.

Maza, S.N., Collo, G., Morata, D., Lizana, C., Camus, E., Taussi, M., Renzulli, A., Mattioli, M., Godoy, B., Alvear, B., Pizarro, M., Ramírez, C., Rivera, G., 2018. Clay mineral associations in the clay cap from the Cerro Pabellón blind geothermal system, Andean Cordillera, Northern Chile. Clay Minerals Journal of Fine Particle Science, 54 (2), pp. 117-141. https://doi.org/10.1180/clm.2018.9.

McDonald, W.J., 1969. Preliminary geophysical report on El Tatio geothermal field. Unpublished Report, Committee for geothermal energy resources (CORFO), 18 pp.

McDonald, W.J., 1974. Geophysical survey of El Tatio geothermal field, Survey for Geothermal Development in Northern Chile. Unpubl. report, Committee for geothermal energy resources (CORFO), 26 pp.

McMillan, N., Davidson, J., Wörner, G., Harmon, R.S., López-Escober, L., Moorbath, S., 1993, Mechanism of trace element enrichment related to crustal thickening: The Nevados de Payachata region, Northern Chile. Geology 21, pp. 467-470. doi:10.1130/0091-7613(1993)021<0467:IOCTOA>2.3.CO;2.

Melosh, G., Cumming, W., Benoit, D., Wilmarth, M., Colvin, A., Winick, J., Soto-Neira, E., Sussman, D., Urzua-Monsalve, L., Powell, T., Peretz, A., 2010. Exploration results and resource conceptual model of the Tolhuaca geothermal field, Chile. Proceedings, World Geothermal Congress 2010, Bali, Indonesia, 25-29 April 2010, 7 pp.

Melosh, G., Moore, J., Stacey, R., 2012. Natural reservoir evolution in the Tolhuaca geothermal field, Southern Chile. Proceedings, 36th Workshop on Geothermal Reservoir Engineering, Stanford University, Stanford, CA. SGP-TR-194.

Mercado, J.L., Ahumada, S., Aguilera, F., Medina, E., Renzulli, A., Piscaglia, F., 2009. Geological and Structural Evolution of Apacheta-Aguilucho Volcanic Complex (AAVC), Northern Chile. XII Congreso Geológico Chileno, Santiago, 22-26 November.

Meunier, A., 2005. Hydrothermal process – thermal metamorphism. Pp. 379-415 in: Clays (A. Meunier, editor). Springer Science and Business Media, Berlin.

Meunier, A., Mas, A., Beaufort, D., Patrier, P., Dudoignon, P., 2008a. Clay minerals in basalt-hawaiite rocks from Mururoa atoll (French Polynesia). I. Mineralogy. Clays and Clay Minerals, 56, pp. 711-729.

Meunier, A., Mas, A., Beaufort, D., Patrier, P., Dudoignon, P., 2008b. Clay minerals in basalt-hawaiite rocks from Mururoa atoll (French Polynesia). II. Petrography and geochemistry. Clays and Clay Minerals, 56, pp. 730-750.

Michelfelder, G.S., Feeley, T.C., Wilder, A.D., Klemetti, E.W., 2013. Modification of the Continental Crust by Subduction Zone Magmatism and Vice-Versa: Across-Strike Geochemical Variations of Silicic Lavas from Individual Eruptive Centers in the Andean Central Volcanic Zone. Geosciences 2013, 3, 633-667; doi:10.3390/geosciences3040633.

Michelfelder, G.S., Feeley, T.C., Wilder, A.D., 2014. The Volcanic Evolution of Cerro Uturuncu: A High-K, Composite Volcano in the Back-Arc of the Central Andes of SW Bolivia. International Journal of Geosciences 5, pp. 1263-1281. doi:10.4236/ijg.2014.511105.

Minissale, A.A., 2018. A simple geochemical prospecting method for geothermal resources in flat areas. Geothermics, 72, pp. 258-267. https://doi.org/10.1016/j.geothermics.2017.12.001.

Moore, D.M., Reynolds Jr, R.C., editors, 1997. X-ray Diffraction and the Identification and Analysis of Clay Minerals. 2nd edition. Oxford University Press, New York, 378 pp.

Muir, D.D., Barfod, D.N., Blundy, J.D., Rust, A.C., Sparks, R.S.J., Clarke, K.M., 2015. The temporal record of magmatism at Cerro Uturuncu, Bolivian Altiplano. In: Caricchi, L., Blundy, J.D. (Eds.), Chemical, Physical, and Temporal Evolution of Magmatic Systems 422 (1). Geological Society of London Special Publications, pp. 57-82. http://dx.doi.org/10.1144/SP422.1.

Muir, D.D., Blundy, J.D., Hutchinson, M.C., Rust, A.C., 2014. Petrological imaging of an active pluton beneath Cerro Uturuncu, Bolivia. Contributions to Mineralogy and Petrology 167: 980. http://dx.doi.org/10.1007/s00410-014-0980-z.

Murphy, M.D., Sparks, R.S.J., Barclay, J., Carroll, M.R., Lejeune, A-M., Brewer, T.S., Macdonald, R., Black, S., Young, S., 1998. The role of magma mixing in triggering the current eruption at the Soufriere Hills volcano, Montserrat, West Indies. Geophysical Research Letters, 25 (18), pp. 3433-3436.

Nisi, B., Vaselli, O., Marchev, P., Tassi, F., 2013. Diffuse CO_2 soil flux measurements at the youngest volcanic system in Bulgaria: the 12.2 Ma old Kozhuh cryptodome. Acta Vulcanologica, 25, 1-2, pp. 169-178.

Ohmoto, H., Goldhaber, M.B., 1997. Sulfur and carbon isotopes. In: Barnes, H.L. (Ed.), Geochemistry of Hydrothermal Ore Deposits. John Wiley and Sons, pp. 517-611.

Pan, S.-Y., Gao, M., Shah, K.-J., Zheng, J., Pei, S.-L., Chiang, P.-C., 2019. Establishment of enhanced geothermal energy utilization plans: Barriers and strategies. Renewable Energy 132, pp. 19-32.

Patrier, P., Beaufort, D., Mas, A., Traineau, H., 2003. Surficial clay assemblage associated with the hydrothermal activity of Bouillante (Guadeloupe, French West Indies). Journal of Volcanology and Geothermal Research, 126, pp. 143-156.

Peccerillo, A., Taylor, S.R., 1976. Geochemistry of eocene calc-alkaline volcanic rocks from the Kastamonu area, Northern Turkey. Contributions to Mineralogy and Petrology, 58 (1), pp. 63-81. https://doi.org/10.1007/BF00384745.

Peréz, Y., 1999. Fuente de aguas termales de la Cordillera Andina del centro-sur de Chile (39–42◦S, 54. Servicio Nacional de Geología y Minería, Santiago, 1 map 1:500,000.

Piscaglia, F., 2011. Il campo geotermico ad alta temperatura del Complesso Vulcanico Apacheta-Aguilucho (Cile settentrionale): esplorazione geo-petrografica di superficie, sorgenti di calore crostali e rocce sigillo. PhD thesis (unpublished, in italian), University of Urbino, pp. 188.

Piscaglia, F., 2012. The high temperature geothermal field of the Apacheta-Aguilucho Volcanic Complex (northern Chile): geopetrographic surface exploration, crustal heat sources and cap rocks. Plinius 38, pp. 4.

Pritchard, C.J., Larson, P.B., Spell, T.L., Tarbert, K.D., 2013. Eruption-triggered mixing of extra-caldera basalt and rhyolite complexes along the East Gallatin-Washburn fault zone, Yellowstone National Park, WY, USA. Lithos 175, pp.163-177. DOI: 10.1016/j.lithos.2013.04.022.

Pritchard, M.E., Gregg, P.M., 2016. Geophysical Evidence for Silicic Crustal Melt in the Continents: Where, What Kind, and How Much? Elements 12 (2), pp. 121-127. https://doi.org/10.2113/gselements.12.2.121.

Procesi, M., 2014. Geothermal potential evaluation for northern Chile and suggestions for new energy plans. Energies 7, pp. 5444-5459.

Raich, J.W., Schlesinger, W.H., 1992. The global carbon dioxide flux in soil respiration and its relationship to vegetation and climate. Tellus, 44B, pp. 81-99. https://doi.org/10.1034/j.1600-0889.1992.t01-1-00001.x.

Ramírez, C., Huete, C., 1981. Carta geológica de Chile, Hoja Ollagüe. Escala 1:250.000. Carta n. 40. Instituto de Investigaciones Geológicas, Santiago, Chile.

Renzulli A., Menna M., Tibaldi A., Flude S., 2006. New data of surface geology, petrology and Ar-Ar geochronology of the Altiplano-Puna Volcanic Complex (northern Chile) in the framework of future geothermal exploration. XI Congreso Geòlogico Chileno, Antofagasta, 7-11 August.

Ridolfi, F., Renzulli, A., 2012. Calcic amphiboles in calc-alkaline and alkaline magmas: thermobarometric and chemometric empirical equations valid up to 1,130 °C and 2.2 GPa. Contributions to Mineralogy and Petrology 163, pp. 877-895. https://doi.org/10.1007/s00410-011-0704-6.

Ridolfi, F., Renzulli, A., Puerini, M., 2010. Stability and chemical equilibrium of amphibole in calc-alkaline magmas: an overview, new thermobarometric formulations and application to subduction- related volcanoes. Contributions to Mineralogy and Petrology 160, pp. 45-66. https://doi.org/10.1007/s00410-009-0465-7.

Riller, U., Petrinovic, I., Ramelow, J., Strecker, M., Oncken, O., 2001. Late Cenozoic tectonism, collapse caldera and plateau formation in the central Andes. Earth and Planetary Science Letters, 188, pp. 299-311. DOI: 10.1016/S0012-821X(01)00333-8.

Rissmann, C., Christenson, B., Werner, C., Leybourne, M., Cole, J., Gravley, D., 2012. Surface heat flow and CO_2 emissions within the Ohaaki hydrothermal field, Taupo Volcanic Zone, New Zealand. Applied Geochemistry, 27, pp. 223-239. doi:10.1016/j.apgeochem.2011.10.006.

Rivera, G., Morata, D., Ramírez, C., 2015. Evolución vulcanologíca y tectónica del área del Cordón Volcánico Cerro del Azufre – Cerro Inacaliri y su relación con el sistema geotérmico de Pampa Apacheta, II Región de Antofagasta, Chile. In Actas XIV Congreso Geológico Chileno, La Serena, Chile, pp. 556-559.

Rodrigo-Naharro, J., Nisi, B., Vaselli, O., Lelli, M., Saldaña, R., Clemente-Jul, C., Pérez del Villar, L., 2013. Diffuse soil CO_2 flux to assess the reliability of CO_2 storage in the Mazarrón-Gañuelas Tertiary basin (Spain). Fuel, 114, pp. 162-171.

Rolleau, E., Bravo, F., Pinti, D.L., Barde-Cabusson, S., Pizarro, M., Tardani, D., Muñoz, C., Sanchez, J., Sano, Y., Takahata, N., de la Cal, F., Esteban, C., Morata, D., 2017. Structural controls on fluid circulation at the Caviahue-Copahue Volcanic Complex (CCVC) geothermal area (Chile-Argentina), revealed by soil CO_2 and temperature, self-potential, and helium isotopes. Journal of Volcanology and Geothermal Research, 341, pp. 104-118. http://dx.doi.org/10.1016/j.jvolgeores.2017.05.010.

Rollinson, H.R., 1993. Using Geochemical Data: Evaluation, Presentation, Interpretation. Longman Scientific and Technical, pp. 352.

Rosner, B., 1983. Percentage Points for a Generalized ESD Many-Outlier Procedure. Technometrics, 25, pp. 165-172.

Royston, P. 1982a. An extension of Shapiro and Wilk's W test for normality to large samples. Applied Statistics, 31, pp. 115-124.

Royston, P. 1982b. Algorithm AS 181: The W test for Normality. Applied Statistics, 31, pp. 176-180.

Salfity, J.A., 1985. Lineamientos transversales al rumbo andino en el noroeste argentino. Congreso Geológico Chileno, Volume 1, pp. 2-119-2-138, Antofagasta, Chile. (Spanish).

Salisbury, M.J., Jicha, B.R., de Silva, S.L., Singer, B.S., Jiménez, N.C., Ort, M.H., 2011. $^{40}Ar/^{39}Ar$ chronostratigraphy of Altiplano-Puna volcanic complex ignimbrites reveals the development of a major magmatic province. Geological Society of America Bulletin 123, pp. 821-840. https://doi.org/10.1130/B30280.1.

Sánchez-Alfaro, P., Reich, M., Arancibia, G., Pérez-Flores, P., Cembrano, J., Driesner, T., Lizama, M., Rowland, J., Morata, D., Heinrich, C.A., Tardani, D., Campos, D., 2016. Physical, chemical and mineralogical evolution of the Tolhuaca geothermal system, southern Andes, Chile: Insights into the interplay between hydrothermal alteration and brittle deformation. Journal of Volcanology and Geothermal Research, 324, pp. 88-104.

Sánchez-Alfaro, P., Sielfeld, G., van Campen, B., Dobson, P., Fuentes, V., Reed, A., Palma-Behnke, R., Morata, D., 2015. Geothermal barriers, policies and economics in Chile – Lessons for the Andes. Renewable and Sustainable Energy Reviews, 51, pp. 1390-1401.

Schilling, F.R., Trumbull, R.B., Brasse, H., Haberland, C., Asch, G., Bruhn, D., Mai, K., Haak, V., Giese, P., Muñoz, M., Ramelow, J., Rietbrock, A., Ricaldi, E., Vietor, T., 2006. Partial

Melting in the Central Andean Crust: a Review of Geophysical, Petrophysical, and Petrologic Evidence. In: Oncken, O., Chong, G., Franz, G., Giese, P., Götze, H.J., Ramos, V.A., Strecker, M.R., Wigger, P. (eds): The Andes. Frontiers in Earth Sciences. Springer, Berlin, Heidelberg, pp. 459-474. https://doi.org/10.1007/978-3-540-48684-8_22.

Sellés, D., Gardeweg, M., 2017. Geología del área Ascotán-Cerro Inacaliri, Región de Antofagasta. Servicio Nacional de Geología y Minería, Carta Geológica de Chile, Serie Geología Básica No. 190, pp. 73, 1 mapa escala 1:100.000, 1 CD con anexos. Santiago (Chile). doi:10.13140/RG.2.2.30946.84165.

Sinclair, A.J., 1974. Selection of threshold values in geochemical data using probability graphs. Journal of Geochemical Exploration, 3, pp. 129-149. https://doi.org/10.1016/0375-6742(74)90030-2.

Soffia, J., Clavero, J., 2010. Doing geothermal exploration business in Chile, Energia Andina experience. Geothermal Resources Council Transactions, v. 34, pp. 637-641.

Sparks, R.S.J., Marshall, L.A., 1986. Thermal and mechanical constraints on mixing between mafic and silicic magmas. Journal of Volcanology and Geothermal Research, 29 (1-4), pp. 99-124. https://doi.org/10.1016/0377-0273(86)90041-7.

Sparks, R.S.J., Sigurdsson, H., Wilson, L., 1977. Magma mixing: a mechanism for triggering acid explosive eruptions. Nature, 267, pp. 315-318. https://doi.org/10.1038/267315a0.

Sparks, R.S.J., Folkes, C.B., Humphreys, M.C.S., Barfod, D.N., Clavero, J., Sunagua, M.C., McNutt, S.R., Pritchard, M.E., 2008. Uturuncu volcano, Bolivia: Volcanic unrest due to mid-crustal magma intrusion. American Journal of Science 308, pp. 727-769. doi:10.2475/06.2008.01.

Springer, M., Förster, A., 1998. Heat-flow density across the Central Andean subduction zone. Tectonophysics, 29, pp. 123-139.

Stimac, J., Goff, F., Goff, C., 2015. Intrusion-related geothermal systems. Pp. 799-822; in: The Encyclopedia of Volcanoes. Elsevier, Amsterdam.

Sun, S.-S., McDonough, W.F., 1989. Chemical and isotopic systematics of oceanic basalts: implications for mantle composition and processes. In: Saunders, A.D., Norry, M.J. (Eds.), Magmatism in the Ocean Basins, Geological Society, London, Special Publications, vol. 42, pp. 313-345. https://doi.org/10.1144/GSL.SP.1989.042.01.19.

Symonds, R.B., Gerlach, T.M., Reed, M.H., 2001. Magmatic gas scrubbing: implications for volcano monitoring. Journal of Volcanology and Geothermal Research, 108, pp. 303-341. https://doi.org/10.1016/S0377-0273(00)00292-4.

Symonds, R.B., Rose, W.I., Bluth, W.I., Gerlach, T.M., 1994. Volcanic-gas studies: methods, results, and applications. In: Carrol, M.R., Holloway, J.R. (Eds.), Volatiles in Magmas. Washington, D.C. Reviews in Mineralogy, 30, pp. 1-66.

Tassi, F., Aguilera, F., Darrah, T., Vaselli, O., Capaccioni, B., Poreda, R.J., Delgado Huertas, A., 2010. Fluid geochemistry of hydrothermal systems in the Arica-Parinacota, Tarapacá and Antofagasta regions (northern Chile). Journal of Volcanology and Geothermal Research, 192, pp. 1-15.

Tassi, F., Nisi, B., Cardellini, C., Capecchiacci, F., Donnini, M., Vaselli, O., Avino, R., Chiodini, G., 2013. Diffuse soil emission of hydrothermal gases (CO_2, CH_4, and C_6H_6) at Solfatara crater (Campi Flegrei, southern Italy). Applied Geochemistry, 35, pp. 142-153.

Taussi, M., Godoy, B., Piscaglia, F., Morata, D., Agostini, S., Le Roux, P., Gonzalez-Maurel, O., Gallmeyer, G., Menzies, A., Renzulli, A., 2019. The upper crustal magma plumbing system of the Pleistocene Apacheta-Aguilucho Volcanic Complex area (Altiplano-Puna, northern Chile) as inferred from the erupted lavas and their enclaves. Journal Volcanology and Geothermal Research. Accepted 25 January 2019. https://doi.org/10.1016/j.jvolgeores.2019.01.021.

Tibaldi, A., Bonali, F.L., 2018. Contemporary recent extension and compression in the central Andes. Journal of Structural Geology 107, pp. 73-92. doi:10.1016/j.jsg.2017.12.004.

Tibaldi, A., Bonali, F.L., Corazzato, C., 2017. Structural control on volcanoes and magma paths from local- to orogen-scale: The central Andes case. Tectonophysics, 699, pp. 16-41. http://dx.doi.org/10.1016/j.tecto.2017.01.005.

Tibaldi, A., Corazzato, C., Rovida, A., 2009. Miocene-Quaternary structural evolution of the Uyuni-Atacama region, Andes of Chile and Bolivia. Tectonophysics 471 (1-2), pp. 114-135. doi:10.1016/j.tecto.2008.09.011.

Tiepolo, M., Oberti, R., Vannucci, R., 2002. Trace-element incorporation in titanite: Constraints from experimentally determined solid/liquid partition coefficients. Chemical Geology, 191 (1), pp. 103-117. doi:10.1016/S0009-2541(02)00151-1.

Tierney, C.R., Schmitt, A.K., Lovera, O.M., de Silva, S.L., 2016. Voluminous plutonism during volcanic quiescence revealed by thermochemical modeling of zircon. Geology 44, pp. 683-686. doi:10.1130/G37968.1.

Tocchi, E., 1923. Il Tatio, ufficio geologico Larderello SpA (Unpublished report).

Todesco, M., Giordano, G., 2012. Modelling of CO_2 circulation in the Colli Albani area. In: The Colli Albani Volcano (Funiciello R. and Giordano G., editors). Special Publications of IAVCEI, 3, pp. 311-329. Geological Society, London.

Trujillo, P., 1971. Sub-surficial geology at El Tatio, Antofagasta Province. Unpublished Report, Committee for geothermal energy resources (CORFO), 14 pp. (in Spanish).

Urzua, L., Powell, T., Cumming, W.B., Dobson, P., 2002. Apacheta, a new geothermal prospect in northern Chile. Geothermal Resources Council 26, pp. 65-69.

Vázquez, M., Nieto, F., Morata, D., Droguett, B., Carrillo-Rosúa, F.J., Morales, S., 2014. Evolution of clay mineral assemblages in the Tinguiririca geothermal field, Andean Cordillera of central Chile: an XRD and HRTEM-AEM study. Journal of Volcanology and Geothermal Research, 282, pp. 43-59.

Venturi, S., Tassi, F., Bicocchi, G., Cabassi, J., Capecchiacci, F., Capasso, G., Vaselli, O., Ricci, A., Grassa, F., 2017. Fractionation processes affecting the stable carbon isotope signature of thermal waters from hydrothermal/volcanic systems: The examples of Campi Flegrei and Vulcano Island (southern Italy). Journal of Volcanology and Geothermal Research, 345, pp. 46-57. http://dx.doi.org/10.1016/j.jvolgeores.2017.08.001.

Ward, K.M., Zandt, G., Beck, S.L., Christensen, D.H., McFarlin, H., 2014. Seismic imaging of the magmatic underpinnings beneath the Altiplano-Puna volcanic complex from the joint inversion of surface wave dispersion and receiver functions. Earth and Planetary Science Letters 404, pp. 43-53. https://doi.org/10.1016/j.epsl.2014.07.022.

Watts, R.B., de Silva, S.L., Jimenez de los Ríos, G., Croudace, I., 1999. Effusive eruption of viscous silicic magma triggered and driven by recharge: a case study of the Cerro Chascon-Runtu Jarita Dome Complex in Southwest Bolivia. Bulletin of Volcanology 61 (4), pp. 241-264. https://doi.org/10.1007/s004450050274.

Wohletz, K., Heiken, G., 1992. Volcanology and Geothermal Energy. University of California Press, Berkeley, California, USA, 432 pp.

Wörner, G., Hammerschmidt, K., Henjes-Kunst, F., Lezaun, J., Wilke, H., 2000. Geochronology ($^{40}Ar/^{39}Ar$, K-Ar and He-exposure ages) of Cenozoic magmatic rocks from northern Chile (18-22°S): Implications for magmatism and tectonic evolution of the central Andes. Revista Geológica de Chile 27 (2), pp. 205-240. http://dx.doi.org/10.4067/S0716-02082000000200004.

Wörner, G., Mamani, M., Blum-Oeste, M., 2018. Magmatism in the Central Andes. Elements 14, pp. 237-244. doi:10.2138/gselements.14.4.237.

Wörner, G., Mercier, R., Kilian, R., Mamani, M., 2004. Geochemistry, radiogenic and U-series isotopes in Andean magmas: crustal assimilation and adakite-like magmatism in the Central and Southern Andes. IAVCEI General Assembly 2004, Pucón, Chile, Volume Abstracts, Oral Session 7a, p. 9.

Wörner, G., Moorbath, S., Harmon, R.S., 1992. Andean Cenozoic volcanic centers reflect basement isotopic domains. Geology 20 (12), pp. 1103-1106. doi:10.1130/0091-7613(1992)020<1103:ACVCRB>2.3.CO;2.

Zandt, G., Leidig, M., Chmielowski, J., Baumont, D., Yuan, X., 2003. Seismic Detection and characterization of the Altiplano-Puna Magma Body, Central Andes. Pure and applied geophysics 160 (3-4), pp. 789-807. https://doi.org/10.1007/PL00012557.

Websites

http://cdm.unfccc.int/Projects

www.enelchile.cl

www.thinkgeoenergy.com/el-tatio-project-in-chile-indefinitely-suspended/

www.westsystems.eu/it

APPENDIXES

CHAPTER 2

Appendix - C2-1

Ar-Ar geochronology

A new $^{40}Ar/^{39}Ar$ age was obtained from unaltered groundmass from one sample (**CP 01 05**) of the Apacheta-Aguilucho Volcanic Complex. This age was measured at Servicio Nacional de Geología y Minería (Chile). Crushing and mineral separation, and sample preparation were carried out following the procedures and parameters established by Salazar et al., 2018. Analysis were done using an ARGUS VI mass spectrometer, with characteristics as indicated at www.sernageomin.cl/laboratorio-geocronología, and parameters indicated in Klug et al., 2018.

Geochemical and isotopic analysis methodology

- Geochemical analyses on samples **AA-010, AA-011, AA-023, AA-024, AA-047, AA-050, AA-054, AA-055, AA-056, AA-058, AA-064, AA-067, AA-077, AA-081, AA-083, AA-094** were carried out at Acme Analytical Laboratories Ltd. (*ACMElab*; Canada). The concentrations of major and trace elements were determined by inductively coupled plasma mass spectrometry (ICP-MS) after fusion by metaborate and aqua regia digestion at the Acme Analytical Laboratories Ltda (Vancouver, Canada). The analytical errors are less than 4% for oxides and of ~5% for trace elements.

- Samples **AA-001, AA-003, AA-006, AA-007, CKA1, C-INKA1, CPB1, ICP16, ICP22, ICP24, CKA1a_ch, CKA1a_sc, C-INKA1f** were analysed at Activation Laboratories Ltda. (*Actlabs*; Canada). Whole-rock major and trace element analyses were determined by Inductively Coupled Plasma-Optical Emission Spectrometry (ICP-OES) and Inductively Coupled Plasma-Mass Spectrometry (ICP-MS), after lithium metaborate and lithium tetraborate fusion. The resulting molten bead is digested in a weak nitric acid solution. The analytical errors are less than 1% for oxides and of ~5% for trace elements.

Sr, Nd and Pb isotope analysis on samples **CKA1, C-INKA1, AA003, CKA1a_ch, CKA1a_sc, C-INKA1f, ICP16, ICP22, ICP24, AA-023, AA-047, AA-055, AA-056, AA-083** were performed at the Istituto di Geoscienze e Georisorse - National Research Council (IGG-CNR) of Pisa (Italy). Rock powders were dissolved in HF + HNO_3 and, after complete drying, Sr and rare earth elements (REE) were purified in an HCl solution through ion-exchange chromatography columns. Nd was then separated from the other REE using a diluted HCl solution passing through Eichrom Ln resin. Lead was extracted from the matrix with conventional chromatographic ion exchange in Dowex 1 anion resin, using standard HBr and HCl elution procedures. Once separated chromatographically, Sr, Nd and Pb were loaded onto Re filaments and successively analysed using a Finnigan Mat 262 thermal ionization mass spectrometer.

The geochemical analysis on the sample **CPAB-ENC-1** was carried out using an X-ray fluorescence (XRF) and a Quadrupole Inductively Coupled Plasma – Mass Spectrometry (ICP-MS) for major and trace elements, respectively, following the procedures, standards and parameters detailed in Frimmel et al. (2001). $^{87}Sr/^{86}Sr$ and $^{143}Nd/^{144}Nd$ compositions were measured using a NuPlasma HR multicollector-ICP-MS (MC-ICP-MS). Full details for these analyses were published by Harris et al. (2015). Both analyses were undertaken at the Department of Geological Sciences, University of Cape Town (South Africa). Two-sigma analytical errors were <2% for XRF, <3% for ICP-MS, and <0.003% for $^{87}Sr/^{86}Sr$ and $^{143}Nd/^{144}Nd$ ratios.

References

Frimmel, H.E., Zartman, R.E., Späth, A., 2001. Dating Neoproterozoic continental break-up in the Richtersveld Igneous Complex, South Africa. Journal of Geology, 109 (4), 493-508. doi:10.1086/320795

Harris, C., Le Roux, P., Cochrane, R., Martin, L., Duncan, A. R., Marsh, J. S., le Roex, A.P., Class, C., 2015. The oxygen isotope composition of Karoo and Etendeka picrites: High δ18. Contributions to Mineralogy and Petrology, 170 (1), 1-24.

Klug, J., Singer, B., Jicha, B., Ramírez, A., 2018. Intercalibrating the SERNAGEOMIN and WiscAr 40Ar/39Ar Geochronology Laboratories for Quaternary dating. In Libro de Actas, XV Congreso Geológico Chileno "Geociencias hacia la comunidad", Concepción, 18-23 November, 2018, p. 892.

Salazar, J.S., Madriaza, E., Fonseca, E., 2018. Mejoras en la preparación de rocas volcánicas cálcicas jóvenes (<1 Ma) para datación Ar/Ar en masa fundamental, en el laboratorio del SERNAGEOMIN. In Libro de Actas, XV Congreso Geológico Chileno "Geociencias hacia la comunidad", Concepción, 18-23 November, 2018, p. 906.

Appendix - C2-2

From Taussi et al., 2019 - supplementary material

Geochronological results

Table S2.1
Summary of the **CP 01 05** $^{40}Ar/^{39}Ar$ step-heating data, and plateau ages obtained from Servicio Nacional de Geología y Minería (Chile).

Sample location
Eastern flank of the Apacheta Volcano

	Watts	$^{40}Ar/^{39}Ar$	$^{36}Ar/^{39}Ar$	^{40}Ar (%)	Ca/K	Cl/K	^{39}Ar (%)	Age (ka)	± Age
A	3.00	0.34849	0.012452	8.6	0.458783	0.011824	4.7	969.40363	77.17753
B	6.00	0.35045	0.002971	28.9	0.748494	0.010947	30.8	974.85515	30.76360
C	9.00	0.34426	0.003058	28.4	1.254484	0.011328	37.4	957.65040	47.76509
D	12.00	0.35717	0.003382	28.0	2.480980	0.010629	13.8	993.53770	94.10200
E	15.00	0.32860	0.003229	27.2	2.335226	0.013119	6.7	914.08786	92.60572
F	18.00	0.34019	0.004099	23.2	2.732973	0.012959	4.2	946.32389	111.97611
G	22.00	0.35140	0.004071	25.0	4.495062	0.016342	1.7	977.48973	197.96048
H	30.00	0.34777	0.003720	26.8	4.493088	0.016326	0.6	967.41359	306.35516

Integrated age

Age (ka)	Error (2σ)
970.00	110.00

Age spectrum (Plateau)

Age (ka)	Error (2σ)	Number of data used	MSWD
967.0277	44.6402	8	0.08

MSWD
mean square of weighted deviates